UNIVERSITY OF CINCINNATI

Date: November 18, 2004

I, Tambe, Samir B.,

hereby submit this work as part of the requirements for the degree of:

Master of Science

in:

Aerospace Engineering

It is entitled:

Liquid Jets In Subsonic Crossflow

This work and its defense approved by:

Chair: Dr. San-Mou Jeng

Dr. Milind Jog

Dr. Prem Khosla

LIQUID JETS IN SUBSONIC CROSSFLOW

A thesis submitted to the

Division of Research and Advanced Studies

of the University of Cincinnati

in partial fulfillment of the

requirements for the degree of

MASTER OF SCIENCE

in the Department of Aerospace Engineering and Engineering Mechanics

of the College of Engineering

2004

by

Samir B. Tambe

B. Tech., Indian Institute of Technology, Bombay, 2002

Committee Chair: Dr. San-Mou Jeng

Abstract

An experimental study has been conducted to study the behavior of liquid jets injected transversely into a subsonic crossflow of air. Liquid jet operating conditions are represented by the aerodynamic Weber number (We) and the liquid-air momentum ratio (q). Three injection liquids, water, Jet-A and N-Heptane, and two injection diameters (D) 0.381 and 0.762 mm, have been used to increase the range of operating conditions for the current experiments. q was restricted to 0.7-10.2 to ensure applicability to premix ducts of LPP combustors. Pulsed shadowgraphy and Phase Doppler Particle Analyzer (PDPA) techniques were used to take measurements for these experiments. Jet breakups and penetrations, and the structures of the sprays produced after breakup have been studied. Two breakup modes have been observed, column and surface breakup. The streamwise location of breakup is constant while the transverse location increases with q. Jet penetrations have been correlated with q, D and the streamwise distance (z). The volume flux of the spray exhibits a maximum in the spray core. Droplet axial velocities (U_d) exhibit a minimum below the spray core and increase with increasing transverse distance. The transverse location of the maximum in the droplet sizes occurs in the spray core for low q. Its location increases with an increase in q. Droplet sizes decrease with an increase in the crossflow velocity (U_∞) while penetration increases with an increase in D or q. This property has been found to be very significant.

Acknowledgements

I express my sincere gratitude to my advisor, Dr. San-Mou Jeng, manager of the Combustion Diagnostic Laboratory (CDL) for his guidance and constant encouragement throughout the course of this thesis and also for providing financial aid.

I would also like to thank Jun Cai for his help in the implementation of my setup and for helping me with my experiments. I also wish to thank Nick Flohre for guiding me through the initial stages of my work and for providing many helpful insights on the way. Thanks are also due to Mr. Curtis Fox, associate researcher at the CDL, for providing invaluable technical insights and help with the design and manufacture of the setup. Thanks to Omar Elshamy for the several technical discussions we had which really helped me gain an insight into the subject.

And finally, I thank my family and friends for their constant support and encouragement without which I could not have persevered.

Table of Contents

List of Figures

List of Tables

List of Abbreviations

Symbols

c, d, e	parameters used in nonlinear regression for constant multipliers
D	Nozzle diameter
M	Mach number
Oh	Ohnesorge number = $\mu_l / \rho_l d \sigma_l$
p, r	parameters used in nonlinear regression as exponents of q and z/D
Re_∞	Crossflow Reynolds number = $\rho_\infty U_\infty D / \mu_\infty$
Re_l	Liquid Reynolds number = $\rho_l U_l D / \mu_l$
U_∞	Crossflow Velocity
U_l	Liquid injection velocity
U_d	Droplet axial velocity
We	Aerodynamic Weber number = $\rho_\infty U_\infty^2 D / \sigma_l$
q	Liquid-air momentum ratio
x	Lateral coordinate
y	Transverse coordinate
z	Streamwise coordinate
μ	Viscosity
ϱ	Density
σ	Surface tension

Subscripts

l	liquid property
d	droplet property
∞	freestream property

Chapter 1: Introduction

1.1 Applications of Liquid Jets in Crossflow

Liquid jets injected into a crossflowing airstream have found many applications in the Aerospace industry. Some of these are film cooling[13,30], lubrication of the bearing chamber[3], thrust vectoring and fuel injection in the afterburner of a gas[29]. Fuel injection in gas turbine[2,4,19], as well as ramjet[16,17,29] and scramjet[17] engines also utilize liquid jets injected into subsonic and supersonic crossflows.

The focus on the study of liquid jets varies depending upon the application. For example, for impingement cooling, the jet needs to impinge on the farther wall, necessitating large values of q. On the other hand, for engine fuel injection applications impingement is to be avoided since it might lead to coking on the walls. Film cooling applications[13] represent the other extreme where the jet is needed to stick to the wall surface to maximize its effect, hence imposing very low values of q. Cooling applications tend to suppress the liquid atomization while engine applications try to maximize it to get a uniform mixture.

The application of interest for the current study is the injection of fuel in the combustion chamber of a gas turbine engine. In keeping up with the high performance needed from modern aeroengines, the formation of effluents like NO_x gases has also increased in recent years[2,22]. Lefebvre[22] has described the mechanisms of NO_x formation and shows the combustion temperature to be the most important factor affecting the formation of NO_x.

One of the ways to reduce NO_x formation is to provide a good mixing of the fuel and air prior to combustion to avoid pockets of high temperature. The presence of low temperatures inhibits the thermal mechanism of NO_x formation. The lean premix, prevaporize (LPP) concept provides an attractive way to achieve this by supplying a completely homogeneous fuel-air mixture to the combustion chamber. The combustion chamber is operated very close to the lean blowout conditions, where the low temperatures ensure a significantly low production of NO_x emissions.

A number of stringent limitations apply on the configuration of the premix duct for LPP combustion. Low fuel residence time is required to prevent the possibility of auto-ignition. This requires rapid atomization within this short time period and high evaporation rates. Atomization and fuel placement have to be coupled carefully to achieve a satisfying fuel-air mixture. Also there is a need to avoid uncontrolled fuel impingement on the walls[4] as it might lead to coking.

The liquid (fuel) jet into crossflow emerges as an interesting candidate for the LPP model of combustion due to its features of rapid mixing of the fuel with air coupled with quick atomization and controllable fuel placement.

1.2 Literature Review

Previous studies of liquid jets injected in crossflows have included analyses in subsonic[1-8,10-15,16-21,24-27] as well as supersonic airstreams[23,24,28,31,34,38]. Some studies have been conducted at atmospheric pressures[1,3,10-12,17,18], while others have tried to simulate gas turbine-like

conditions by testing at elevated pressures[2,4,19,20]. Existing literature covers several experimental[1-8,10-13] as well as computational[1,8,13,25,26] studies.

The behavior of liquid jets injected into a supersonic crossflow exhibits marked difference from their behavior when injected into a subsonic crossflow[23]. In the case of a supersonic crossflow, the presence of shock waves dominates the flowfield and the jet is violently sheared off due to the high crossflow velocities. Jets injected into a subsonic crossflow exhibit a smother expansion and breakup characteristics[23]. However some of the trends are common for both flows, and we will consider these while focusing mainly on subsonic crossflows.

The liquid jet bends soon after injection due to the airstream dynamic pressure, which exerts a drag force on the jet[15]. The drag also induces a flattening of the jet[1], which causes a further increase in the drag, thus accelerating the bending process[17,27,36]. The flattening of the jet produces a kidney shaped cross-section of the jet[4,16,17]. The bending of the liquid column is followed by its breakup into ligaments, which undergo further breakup to produce a region of droplets[36].

Waves have been observed on the windward as well as the leeward surface of the jet column[2,36]. Schetz et al[31] related the windward waves to the liquid acceleration. These waves seem to be two dimensional at low air velocities; however, some three-dimensional effects are seen at higher air velocities[16]. The location of the column breakup is seen to coincide with the one of the troughs of the windward waves[2,23]. Ingebo[18] classified these waves as acceleration and capillary waves, and atomization was described as the process of forming

ligaments from the crests of these waves. Thus waves were seen to be responsible for jet breakup.

More recent studies have indicated that the liquid flow in the jet column is not smooth, due to the presence of several vortex systems in the jet flowfield[8,13,20,30,33]. Horseshoe and wake vortices have been observed in the flow around the jet, while the jet flow itself contains periodically shed ring vortices and a counter-rotating vortex pair. These cause the irregularities on the jet surface[8], and could be responsible for the jet breakup, but no studies have linked them to the breakup as yet.

Many studies have focused on the jet trajectory[2,17,24,32,36] and the transverse penetration[3,5] and lateral spread[2,17] of the jet. Schetz and Padhye[32] found that the maximum penetration height is the distance required to redirect the liquid momentum in the crossflow direction. Wu et al[36] modeled the jet trajectory by balancing liquid acceleration with aerodynamic drag forces in the airstream direction. Investigation of jet penetrations involve visualization techniques like pulsed shadowgraphy[27], Mie scattering of laser lightsheets[4,11] and Phase Doppler Particle Analyzer (PDPA) measurements[24]. The jet penetration has been studied in the form of the breakup location[3,7] as well as in terms of the jet trajectory[2,36]. Several correlations have been determined for the jet penetrations, with the expressions ranging from power laws[32,36] to logarithmic[2,38] and exponential[6] relations. Correlations also exist for jet widths[2,17].

Correlations for jet penetration generally formulate the penetration as depending upon the momentum ratio (q), the nozzle diameter (D) and the streamwise distance (z)[2,6,12,36]. However, considerable quantitative differences have been observed in these predictions.

These differences could be attributed to the different measurement techniques, non-uniformity in defining the trajectories, and the effect of presence of boundary layers, which has not been quantified in any study present in the literature. Studies have used the transverse jet extremities[5,14], mean streamline locations[39], locations of maximum velocities[39] and the locations of maximum flux concentration[11,33] to correlate jet trajectories. Differences in measurement methods also affect the penetration predictions. Lin et al[24] observed that for the same test facility and injectors, the penetrations predicted by shadowgraphy were consistently lower than those predicted by PDPA. This happens because shadowgraph images are highly dictated by the number density of droplets and as such tend to overlook regions containing a few droplets[24]. Similar observations were made by Inamura et al[17], Thomas Schetz[34] and Yates[38]. Furthermore, the penetration correlations proposed by some of the studies were based on near-field investigations[2,36], while others were based on far downstream locations[38]. Chen et al[6] recognized that the jet flowfield can be subdivided into three regions and that these different regions could have differing effects on the jet penetration. They proposed a three parameter correlation for the jet penetration to account for these effects. The effect of the boundary layer was observed by Chelko[5], who found that the penetrations from a nozzle mounted flush with the chamber walls differs from that of a jet injected from a tube protruding into the flow. Cortelezzi and Karagozian[8] found that penetration increases with increasing boundary layer thickness. This indicates that boundary layer does affect the jet penetration; however no quantifiable relationships are available in literature.

There have been some exceptions where the penetration has been found to depend on parameters other than q, D and z. Birouk et al[3] correlated jet penetrations in the form of the

transverse coordinate of the breakup location and found a dependence of the penetrations on the Oh for large values of the liquid viscosity. Liu et al[25] observed that for large enough changes in the crossflow velocity (U_∞), the jet penetration decreased with an increase of U_∞, keeping q constant.

The jet penetrations have also been observed to depend on the shape of the injection hole, with higher penetration for low-aspect-ratio holes (elongated in the streamwise direction) and lower penetration for high-aspect-ratio holes (elongated in the direction normal to the streamwise direction) as compared to circular holes[13]. The shape of the hole changes the distance between the counter-rotating vortex pair, which affects the penetration[13].

In addition to transverse injection, a few studies have also considered angled jet injection into crossflows[10,11]. The angle of jet injection is considered positive when the injection velocity has a component in the direction of the crossflow velocity; and negative when it has a component in the opposite direction. Fuller et al[10] observed that the jet penetrations decrease with a decrease in the injection angle. Also at low angles, the jet undergoes non-aerodynamic breakup similar to a jet in a coaxial flow[10].

The entrainment of the crossflow fluid by the jet has also been a parameter of interest. The drag exerted by the airstream and the crossflow entrainment are the two chief causes of jet bending[39]. The entrainment of the high velocity crossflow particles cause the jet to gain streamwise momentum, causing it to bend in the direction of the crossflow[39]. The entrainment behavior has been observed to depend upon the angle of jet injection. Jets injected at negative angles are found to entrain more crossflow fluid as compared to

transverse or positive angled jets[11]. The jet vorticity has been found to be responsible for a part of the crossflow entrainment[8].

Breakup modes and locations have also been investigated in the existing literature. Vich and Ledoux[35] have classified the modes of breakup as simple column fracture, arcade-type breakup, and bag-like breakup. Wu et al[36] found two modes of breakup, column breakup and surface breakup. They also proposed a "breakup map" in the plane of aerodynamic Weber number (We) and momentum ratio (q). Becker and Hassa[2] studied the process at elevated pressures and found breakup processes similar to those found by Wu et al[36]. They also found a high correspondence with the breakup map of Wu et al[36].

Inamura et al[17] found that the breakup always occurs at a constant streamwise location. This has been later corroborated by other studies[2,36]. The transverse breakup location has been correlated with the momentum ratio. However, a few exceptions do exist. One exception was found in the study by Schetz and Padhye[32], who found the value of the streamwise breakup location to increase with q. Birouk et al[3] found the correlations for the breakup locations to for highly viscous liquids needed to be modified by adding a dependence on the Ohnesorge number (Oh). Also even though studies agree on a constant streamwise breakup location, some variance is found in the numeric value of this location[17,36].

A number of studies have also investigated the droplet characteristics of the sprays formed after breakup[2,12,14,16,18,19,21,23]. Older studies were based on photographic techniques[19,32]; more recent studies include methods like spray sampling using an isokinetic sampling probe[16], Fraunhofer diffraction technique[23], Malvern Droplet size analyzer[12] and PDPA[16,37].

Variations of the droplet diameters, liquid velocities and volume flux have been studied. Correlations have been proposed for mean diameters and the spray cross-sectional areas[37].

The volume flux exhibits a maximum in the region of the spray core and decreases on all sides. Droplet velocities exhibit a minimum just below the spray core due to the presence of a wake region. Also the velocities near the top of the plume are less due to momentum exchange. With increasing transverse distance, the droplet velocities decrease to a minimum below the spray core, increase and then decrease near the top of the spray plume[16]. For low U_∞ the droplet sizes exhibit a maximum in the spray periphery, however for high U_∞ the maximum is observed in the spray core[16].

Effects of various parameters on the spray properties have been studied. Inamura and Nagai[16] observed that the volume flux distribution evens out with an increase in the streamwise distance. Zhu et al[40] report that the atomization of the jets resembles pressure atomization at low freestream velocities, and airblast atomization at high freestream velocities. The droplet size decreases with an increase in the air velocity[12,14,16,37,40], but is not affected by the liquid injection velocity[14]. Ingebo and Foster[19] found that the droplet sizes are not affected by air and liquid temperatures. However, Nejad and Schetz[28] found the droplet diameters to decrease with an increase in q. Droplet sizes are also found to decrease with an increase in the crossflow density[12], a decrease in the surface tension of the liquid[12,28] and with a decrease in the liquid viscosity[28].

Chapter 2: Experimental Objectives and Scope

2.1 Objectives

We have observed that liquid jets injected into subsonic crossflows have found significant applications in gas turbine combustors. The current study aims to further study the characteristics of liquid jet injection in realistic gas turbine-like conditions. As a first step, the properties of liquid jets were studied at atmospheric pressures, which is the basis of this report. The studies can then be extended to elevated pressures and elevated temperatures, and together can form a basis for the conclusion of the properties in realistic conditions. Jet injection angles were restricted to 90°; that is, the jets were injected in a direction normal to the crossflow. Studies are restricted to the near field regions, due to the length constraints and rapid mixing requirements on premix ducts.

The objectives of the current work are to conduct a parametric study of the behavior of the jet. This study will be focused on the behavior of the jet column as well as the distributions of droplet sizes and velocities in the spray produced after breakup. The aerodynamic Weber number, We, and the liquid-air momentum ratio, q, are chosen to be the parameters of significance. Also the breakup behavior and the breakup locations will be studied. Moreover the jet trajectory and penetrations are to be studied and an empirical correlation for the jet penetrations will be developed based on the experimental data.

2.2 Experimental Test Range

As mentioned in the previous section, the aerodynamic Weber number (We) and the liquid-air momentum ratio (q) have been selected as the governing parameters that influence the jet properties. In concert with the applicability to LPP premix ducts, the momentum ratios are to be restricted to $q < 15$. This is required to prevent excessive impingement of the farther wall, which could lead to coking. For the present experiments, a range of $0.7 < q < 10.2$ was employed. Liquid injection velocities (U_l), however, depend upon the air velocities, which were determined from We. The liquid velocities were adjusted to achieve the corresponding q values.

It was sought to maximize the range of We tested to include all possible engine operating conditions. We is directly proportional to the dynamic pressure of the crossflow (crossflow velocity) and the jet injection diameter, and inversely proportional to the liquid surface tension. Thus the We can be increased by increasing the air velocity and injection diameter and by decreasing the liquid surface tension.

Air velocities were varied from a low subsonic value of $M = 0.22$ to a high subsonic value of $M = 0.63$. Physically, airspeeds varied from 90 m/s to 215 m/s. Two nozzle sizes were used, with diameters of 0.381 mm (0.015") and 0.762 mm (0.030"). Also three injection liquids were used, water, Jet-A and N-Heptane, to provide a surface tension range of 21.4-72 N/m.

A combination of these properties produced a We range of 50-1725. Liquid injection velocities (U_l) were adjusted to maintain appropriate q values and were found to range from

3-21 m/s for water, 2-24 m/s for Jet-A and 4-26 m/s for N-Heptane. Air and liquid Reynolds numbers (Re_∞, Re_l) varied from $1.79 \times 10^3 - 1.06 \times 10^4$ and $600 - 4 \times 10^7$ respectively, and Ohnesorge numbers (Oh) varied from $1.4 \times 10^{-2} - 8 \times 10^{-2}$. A summary of test conditions has been listed in Table 2.1. The details of the test conditions used for Pulsed Shadowgraphy are given in Appendix A. The test conditions used for PDPA have been included in Chapter 6 (Table 6.1).

Table 2.1 Range of Experimental Parameters

	Water	Jet-A	N-Heptane
ρ_l, kg/m^3	996	800	683.7
$\mu_l \times 10^4$, kg/m/s	8.65	13	6
$\sigma_l \times 10^3$, N/m	72	28	21.4
D, mm	0.381	0.381, 0.762	0.381, 0.762
U_l, m/s	3-21.7	2.7-24.0	4.1-26.4
U_∞, m/s	89.2-197.4	173.1-197.5	118.8-214.8
M_∞	0.26-0.57	0.23-0.63	0.35-0.62
q	0.9-10.2	0.8-9.9	0.7-9.8
We	50.5-247.6	99.0-1274.0	301.6-1725.1
$Re_\infty \times 10^{-3}$	2.36-5.22	2.06-10.43	3.14-10.62
$Re_l \times 10^{-4}$	0.13-0.95	0.06-2195	0.18-4206
$Oh \times 10^3$	5.2	14.07, 9.95	8.04, 5.68

Chapter 3: Experimental Setup

3.1 Overall Setup

An overall representation of the experimental setup is given in Fig. 3.1. The experiments are conducted in a test chamber of internal size 2.54 cm × 2.54 cm (1" × 1"). The test chamber was made out of clear acrylic material to ensure maximum optical accessibility. The length of the test chamber is 25.4 cm (10"). A flange is provided on one end to attach the chamber to the setup in a cantilever fashion. A provision for the liquid nozzle is made in the form of a simple hole. The hole is sized to fit a 6.35 mm diameter tube (1/4" standard SS tubing) with minimum clearance. It is located 12.7 cm (5") from the end of the chamber. The transverse location is at the center of the width dimension. A schematic of the test chamber, along with the coordinate axes used in the experiments, is provided in Fig. 3.2 a.

The test chamber was connected to a rig of inner diameter 15.24 cm (6") through a 22.86 cm (9") long, in-house designed, 15.24 cm – 2.54 cm (6" – 1") flow reducer. The rig is simply a long pipe, which acts as the plenum for the experimental setup. Static pressure and temperature measurements are assumed to be the stagnation values. Fig. 3.2 b. shows a picture of the test chamber along with the 15.24 cm rig.

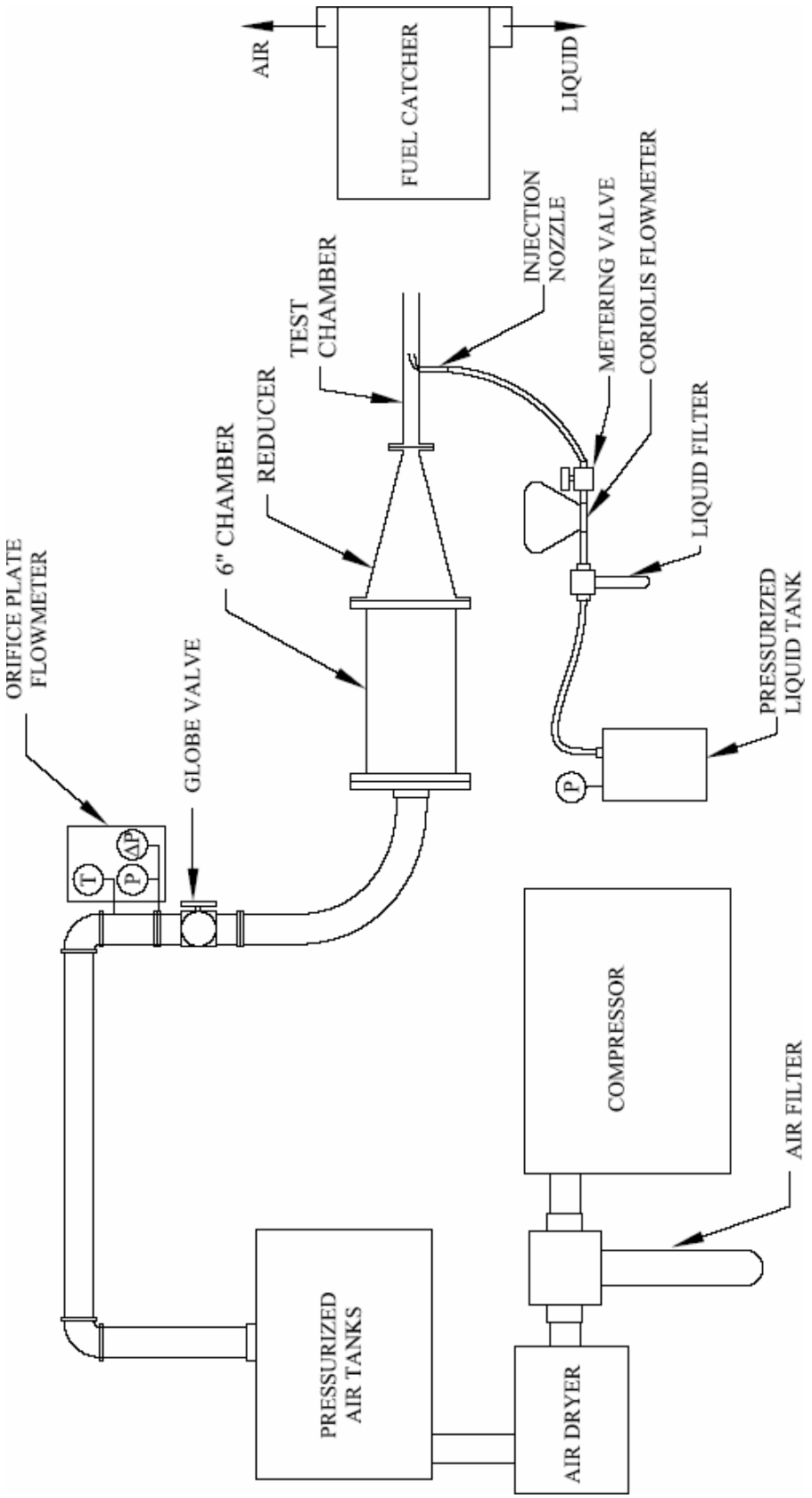

Fig. 3.1 Schematic of Overall Setup

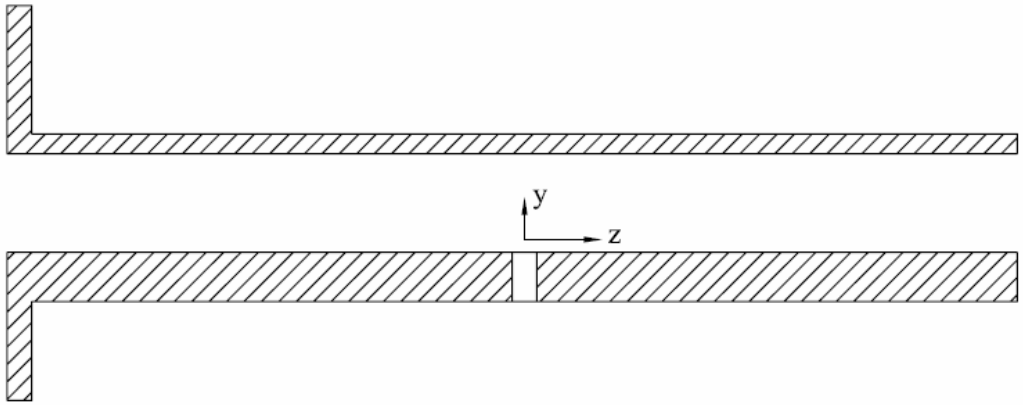

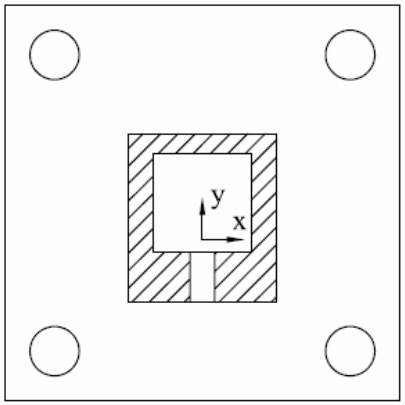

Fig. 3.2 a. Schematic of Test Chamber

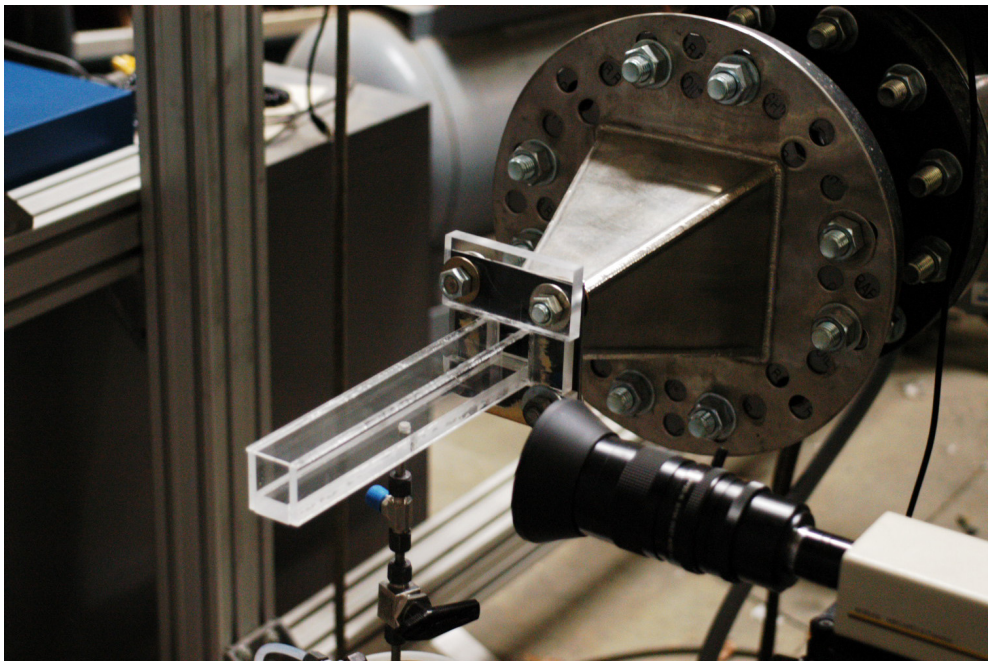

Fig. 3.2 b. Test Chamber in Setup

3.2 Air supply

The compressed airflow setup consists of a compressor, dryer, pressurized tanks and compressed air tubing. Air is compressed by a Kaeser Variable Speed 335 hp, rotary screw compressor rated at 1483 SCFM at 100 psig, which can provide airflow rates up to 0.907 kg/s (2 lb/s) at pressures of up to 13 bars (175 psig). A Domnick-Hunter Series DBP 1680, 200 psi heat reactivated blower purge desiccant air dryer and two 620 gallon vertical receiver tanks complete the compressed airflow setup. The compressed air stream is fed to the rig through a series of 10.16 cm (4") and 5.08 cm (2") compressed air piping, and finally by a 5.08 cm (2") flexible hose. An orifice flow meter is located on the compressed air piping and was used to measure the air mass flow. A standard globe valve is used to control the airflow. All of these components can be seen in the schematic diagram of Fig. 3.1.

3.3 Liquid supply

The liquid injection system consists of a tank to house the liquid, a pressurizing device to maintain uniform flow, flowmeter, valve and the injection nozzle, connected through suitable piping. Two tank - pressurizing device combinations were used, depending upon the liquid used. Jet-A was housed in a large tank and a submersible pump provided the fuel flow at 13.79 bar (200 psi). For water and N-Heptane, another smaller tank was used. A small compressor was used to pressurize this tank at 9.65 bar (140 psi). A Micro Motion CMF010 coriolis flowmeter was used to measure the liquid mass flow rates. A Parker metering valve was used for control of the liquid flow rates. The schematic diagram of Fig. 3.1 shows these components, where the tank-pressurizing device combination has been represented by a single unit.

The liquid injection nozzle essentially is a 5.08 cm (2") long piece of ¼" stainless steel tubing (6.35 mm outer diameter) with a flat end. The nozzle is a hole drilled in the center of this end-wall. The tubing walls are about 1.01 mm (0.04") thick. A taper is provided in the flow area just prior to injection to smoothen out the flow. The depth of the nozzle hole was 0.508 mm (0.020"). Two injection diameters were used for the experiments, 0.381 mm (0.015") and 0.762 mm (0.030"). The L/D values for these nozzles are 1.33 and 0.67 respectively. A schematic representation of the liquid injection nozzle is shown in Fig. 3.3.

For the experiments involving Jet-A and N-Heptane liquids, an in-house developed fuel catcher system was used to separate the liquid from the flow and recycle it.

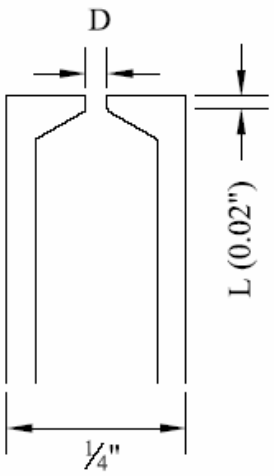

Fig. 3.3 Schematic of Injection Nozzle

Optical systems used for taking measurements of the flow were pulsed shadowgraphy and Phase Doppler and Particle Analyzer (PDPA) systems. Both of these setups are described in the following subsections.

3.4 Shadowgraphy Setup

The pulsed shadowgraphy setup consists of a pulsed light source, collimating lenses and a CCD camera. The light source used is the Xenon Nanopulse system. The Nanopulse system consists of a Xenon Nanolamp 737B controlled by a Xenon Nanopulser 437B. The Nanopulser is the power source for the Xenon Nanolamp. It allows a variation of the power output to the Nanolamp and provides different modes of triggering it. The Nanolamp is essentially a coaxial capacitor with a charge voltage applied at one end and a spark gap at the other. The charge is provided by the Nanopulser. The Nanolamp is capable of emitting 5 mJ pulses of 10 ns duration. A pinhole aperture was used with the nanolamp to obtain a point source of light.

15.24 cm (6") diameter spherical lenses with a focal distance of 450 mm were used to collimate the light beam emitted from the Nanolamp. The choice of the large lens size arises from the fact that optical defects are known to occur near the periphery of any mirror or lens. The choice of a large enough diameter for the lenses allows us to position them so that the area of interest of the chamber is located approximately in the center of the beam, thus avoiding any optical defects.

Lenses have been chosen to obtain a straight optical path to avoid the complicated optical path involved in using mirrors. However, the use of a lens has the disadvantage of making the path too long, thus occupying a large area. This happens because in order to obtain a collimated beam of light, the light source needs to be placed at the focus of a lens. One way to work around this difficulty is to use a series of lenses in tandem, which brings down the focal length of the combination, thus bringing down the size of the optical setup. For the current experiments, three lenses of the same size and focal length were used in tandem. The focal length of the combination was found to be approximately 100 mm.

A RedLake Megaplus ES 1.0 CCD camera was used to take pictures of the jet. A Canon V 6 × 16-1.9 Macro lens (manual zoom) was used with the camera. The camera has a CCD array of 1018 × 1008 pixels. The magnification was adjusted using spacers between the lens and the camera to obtain a field of view of approximately 2.54 cm × 2.54 cm (1" × 1").

The camera is attached to a PIXCI data acquisition board, which is controlled by the EPIX image acquisition and processing software. The EPIX software provides a user-friendly

interface to manipulate the image acquisition characteristics of the camera. It also provides many image processing features.

The nanolamp – lens combination and the camera were mounted on either sides of the test chamber on a bosch rail frame. A schematic of the shadowgraph setup is shown in Fig. 3.4a and a picture of the same is shown in Fig. 3.4b

3.5 PDPA setup

For the PDPA experiments the test chamber and the reducer were attached to another 15.24 cm (6") chamber, which acted as the plenum. The 6" chamber was mounted on a Lintek three-axes traverse. The transmitter and receiver for the PDPA measurements were mounted on a stationary bosch rail framework, and the chamber itself was traversed for the experiments.

A detailed description of the PDPA setup can be found in Flohre[9]. A Coherent Innova 90 argon ion laser forms the core of the PDPA system. It produces a light beam within the green-blue-violet energy spectrum at a maximum power of 5 watts. An Aerometrics FBD 240-R FiberDrive beam separator separates the beam into its constituent green (514.5 nm), blue (488.0 nm) and violet (476.5 nm) components. Only the green and the blue beams were used in the course of the experiments. The FiberDrive further splits each of these components into two and shifts the frequency of one set by 40 MHz using a Bragg cell. All beams, shifted and unshifted, are focused onto fiber-optic cables connected to an Aerometrics XRV204-4.2 two component transmitter outfitted with a 500 mm focal lens. An

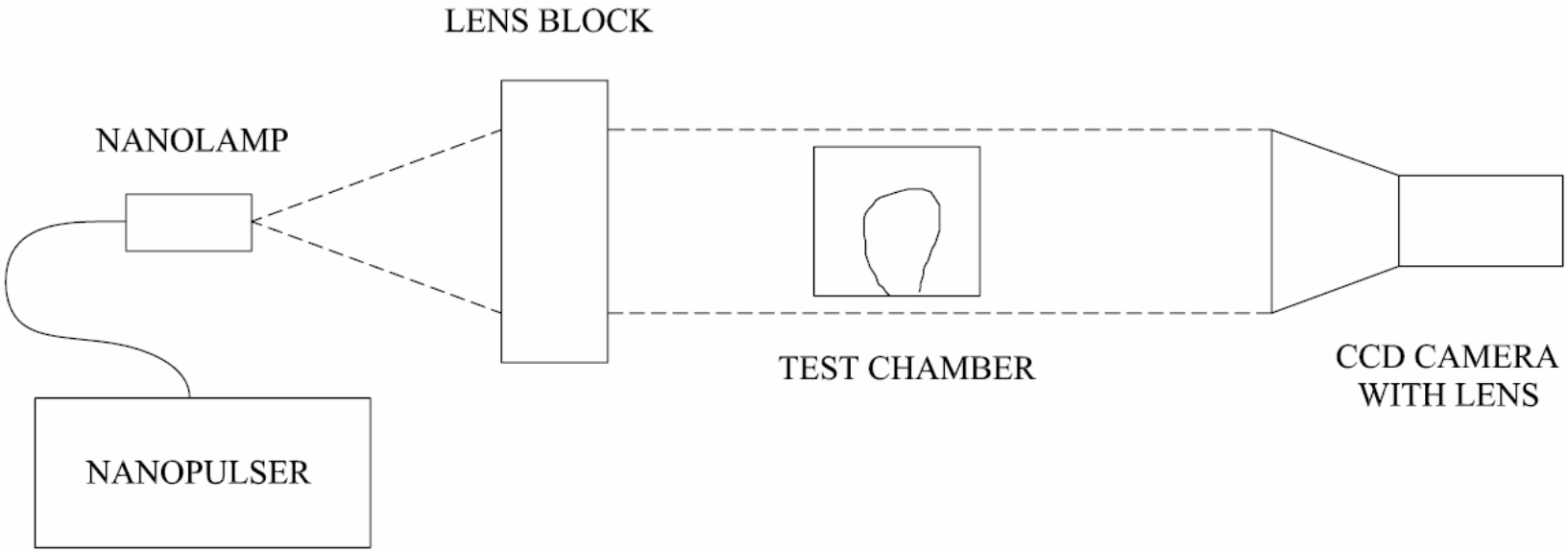

Fig. 3.4 a. Schematic of Shadowgraphy Setup

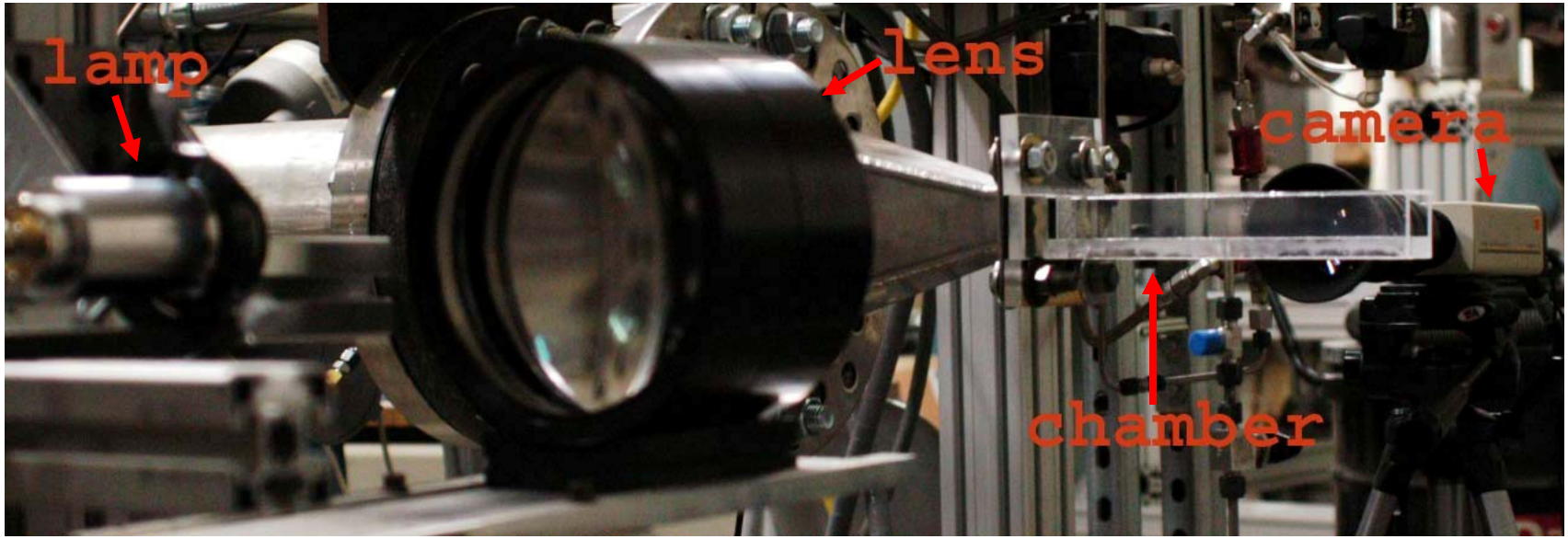

Fig. 3.4 b. Shadowgraphy Setup

Aerometrics RCV208 receiver is mounted across from the transmitter at a 30° azimuthal angle. Both transmitter and receiver are mounted on stationary frames as mentioned above. The receiver sends signals to an Aerometrics RCM200LP6 Photodetector, which directs the blue and green signals to different Real Time Signal Analyzers (RSA 2000-P2 for green and RSA 2000-L for blue). The analyzer sends the processed data to a computer with DataView software installed. The computer also manages the traverse through a Velmex VP9000 controller. Fig. 3.5 shows a schematic representation of the PDPA setup.

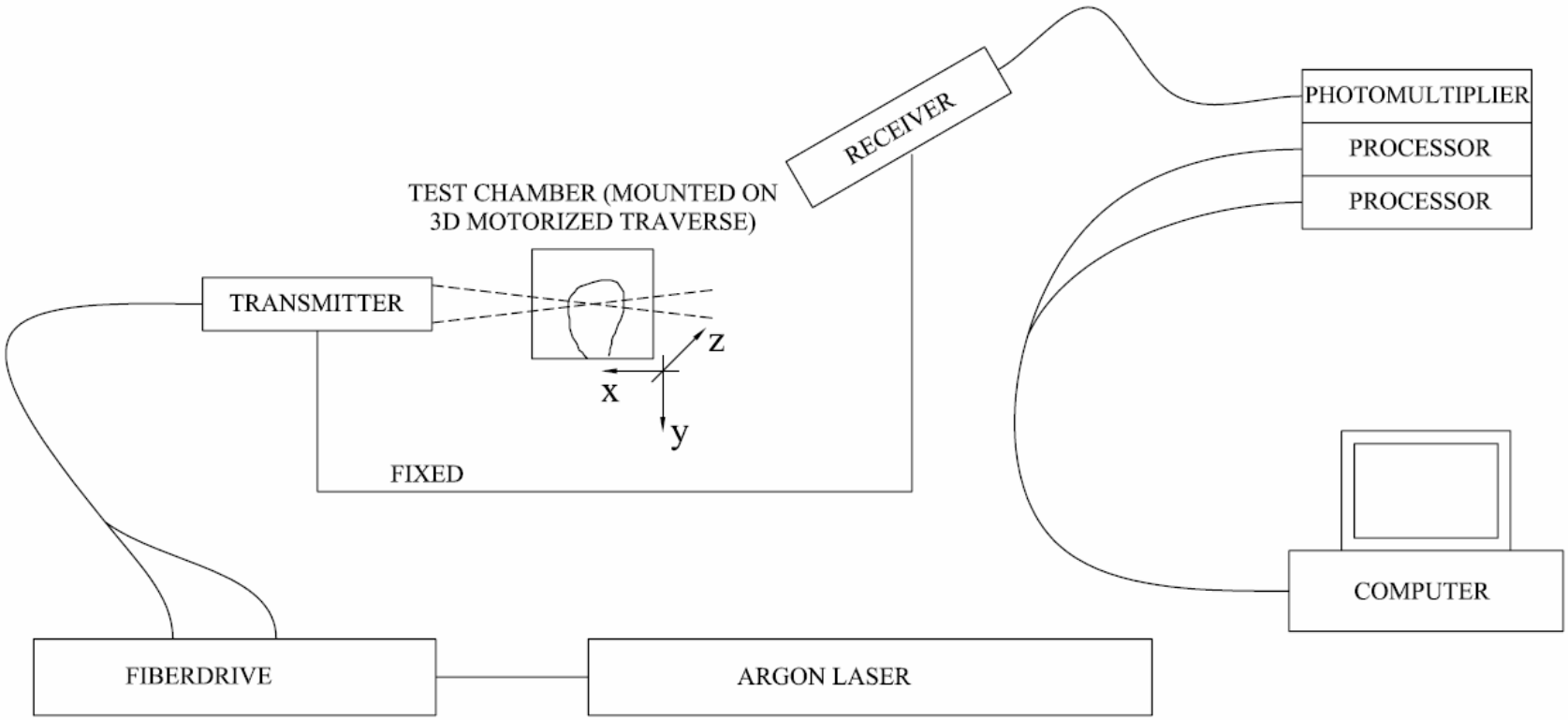

Fig. 3.5 Schematic of PDPA Setup

Chapter 4: Results and Discussion - Jet Column Behavior

4.1 Outline of Results

Flow visualization was carried out on the liquid jets using pulsed shadowgraphy to study the behavior of the liquid jet. Also PDPA analysis was carried out to study the behavior of the post-breakup spray produced by the jet. PDPA analysis was carried out at two cross-sectional planes and the center-plane. The variation of the jet and spray behavior was also studied with changes in We and q.

We will first discuss the behavior of the jet column and the effect of changes in We and q on the same. That will be the subject of the remainder of this chapter. In chapter 5, we will discuss the distribution of the spray properties in the cross section of the jet, while Chapter 6 will focus on the spray distributions in the center-plane. Both of these chapters will also elaborate on the effects of various parameters on the baseline distributions.

In chapter 7, we will discuss the characteristics of the overall jet, which includes the penetration and breakup behavior of the jets. We will study the different breakup modes and their regions of occurrence. Also the location of breakup and its dependence on various parameters will also be studied. Additionally, we will develop an empirical correlation to fit the penetration profiles of the jets produced in the current study, and this correlation will be compared to the ones existing in literature.

4.2 Flow Visualization using Pulsed shadowgraphy

Pulsed shadowgraphy was used to carry out floe visualization of the liquid jets. Instantaneous shadowgraphs of the flow were captured which were then used to extract information about the jet column behavior, breakup modes and locations and the jet penetration behavior.

The phenomenon of jet injection into crossflows has been observed to be a highly unsteady behavior. The unsteadiness is usually attributed to presence of crossflow boundary layers near the channel walls and turbulence in the crossflow. Recent studies focusing on the vortex structures present in the jet flowfield have observed periodic shedding of ring-like vortices along the length of the jet column[8,13,20,30,33]. This indicates that turbulence in the jet flow could also be a primary reason for unsteadiness in the jet flow.

The effects of this unsteadiness are countered by taking multiple images and averaging them out to observe the steady state characteristics. For the current study, 20 shadowgraphs were taken for each test condition, where a test condition is defined as a particular combination of values of the We and q parameters. These images were then averaged using the image processing toolbox in MATLAB. Both the instantaneous and the averaged shadowgraphs have been used to derive relevant conclusions. The instantaneous shadowgraphs reveal information on the jet column and breakup behavior. On the other hand, the averaged shadowgraphs are used to determine the jet penetrations.

We now discuss the behavior of a typical jet column, which will be denoted by the Baseline case. Next we will discuss the change in the column behavior due to a change in different parameters. The effect of a change of q is observed by changing the liquid velocity, U_l; while the effect of a change of We is collectively concluded through the effects of changes in U_∞, D and σ.

4.3 Baseline Case

Fig. 4.1, taken from Wu et al[36], shows a schematic representation of the typical jet behavior and breakup processes. The dynamic pressure of the airstream creates a region of high pressure on the windward surface of the jet and a region of low pressure on the leeward surface. The pressure distribution creates an aerodynamic force on the jet very much similar to the drag experienced by a body in a fluid flow, and causes the jet to bend in the direction of the airstream[15]. The acceleration of the ambient fluid over the jet column creates a pressure distribution on the jet, which draws out the liquid in the cross-stream direction, causing the jet to flatten until the counteracting surface tension forces limit this flattening[1]. This flattening ultimately leads to the formation of the kidney-shaped jet[4,16,17]. As the jet flattens, the increase in its width induces an increase in the drag experienced by the jet, which accelerates the turning of the jet in the airstream direction[17,27,36]. As a result the jet rapidly bends and soon aligns itself with the crossflow.

Within a few jet diameters distance of injection into the crossflow, waves are seen to appear on the surface of the jet column[2,36]. These waves are observed on the windward as well as the leeward side of the jet. The jet bending has been observed to accelerate with the appearance

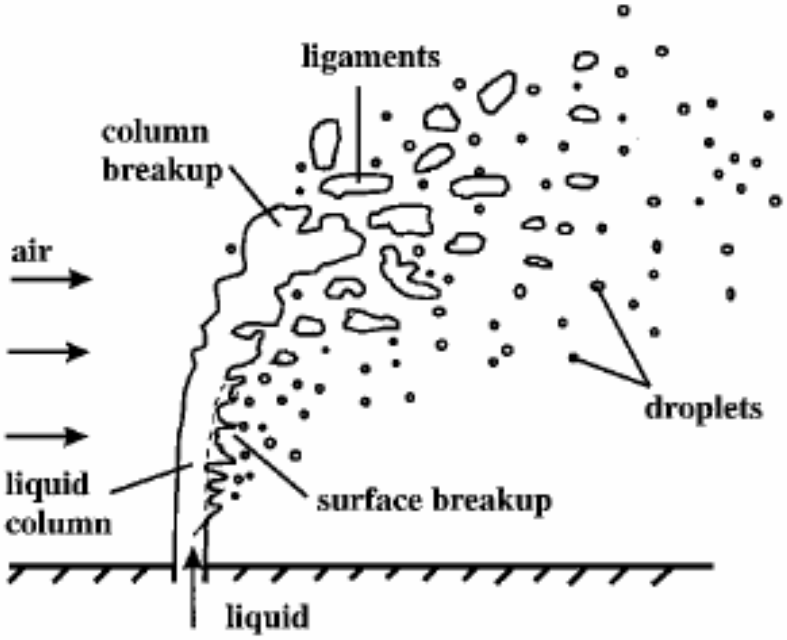

Fig. 4.1 Behavior of a typical jet column[36]

of these surface waves. Also the wavelengths of these waves increase along the length of the jet column. This is observed till the jet ruptures at one of the wave troughs[2,23]. Thus surface waves play an important role in the jet breakups.

The fracture of the jet column occurs at one of the wave troughs, but not at each trough. This produces short segments of jets, which are called as ligaments. These ligaments undergo further breakup to form droplets[36] by a mechanism which is very similar to the breakup of droplets subjected to shock wave disturbances. The droplets produced by this mechanism have diameters of the order of the jet column diameter. These droplets also further breakup with distance forming smaller droplets.

In addition to this, another mechanism of formation of droplets is seen by way of stripping off of droplets from the leeward side of the jet. In reality, this shearing mechanism occurs on

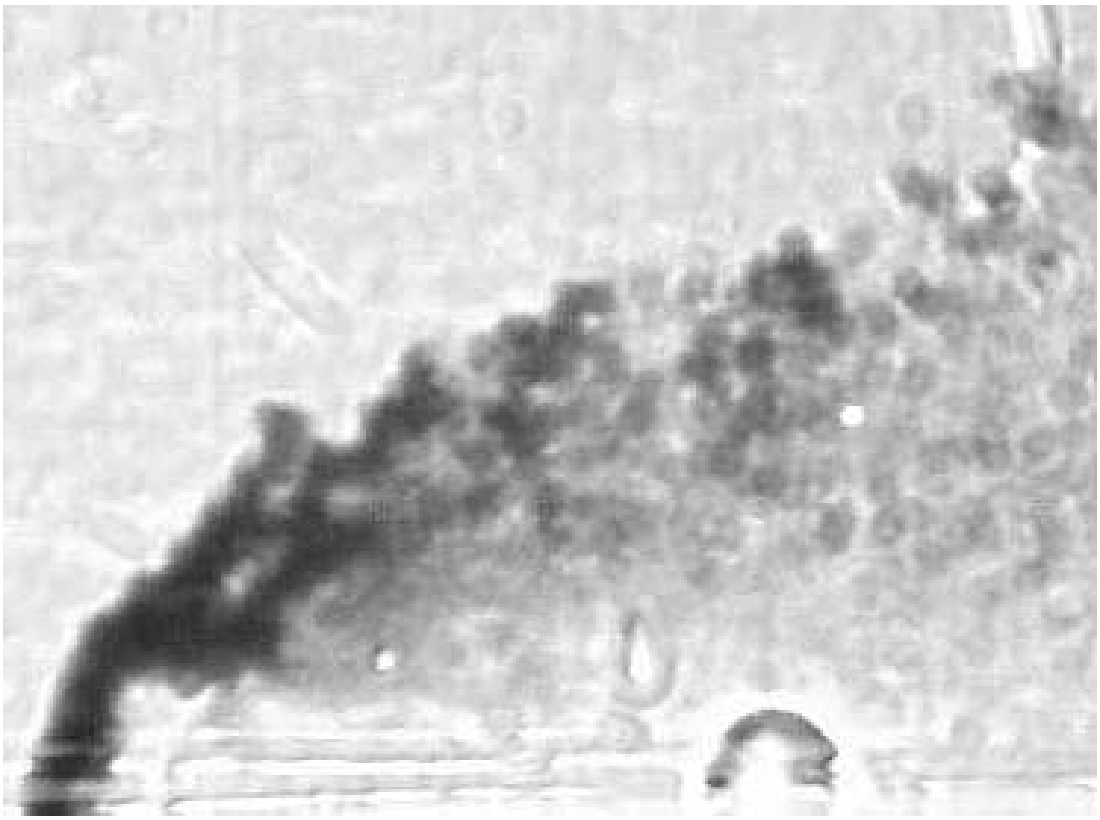

Fig. 4.2 Shadowgraph of a typical jet

the sides of the jets as well; however, this aspect is not observable due to the orientation of the shadowgraphs. The stripping mechanism occurs due to the shearing action of the dynamic pressure of the airflow over the jet. The droplets produced by this mechanism are generally much smaller than those produced from the breakup of the ligaments. This mechanism plays an important role in the determination of the breakup mode as will be seen in Chapter 5. This shearing-off of droplets has been called as surface breakup[36].

A shadowgraph of a sample jet case of a 0.381 mm jet of Water at conditions of We = 50.5 and q = 5.9 is shown in Fig. 4.2. Most of the features discussed above can be easily observed in this picture. We now proceed to investigate the effects of various parameters on the jet column behavior.

4.4 Effect of q on Column Behavior

Fig. 4.3 shows the effect of q on the behavior of the jet column. Shadowgraphs of 0.381 mm jets of Jet-A at We = 483.4 are shown at q = 2.4 in Fig. 4.3 a. and at q = 8 in Fig. 4.3 b. The change in q from 2.4 to 8 is brought about by increasing the U_l from 10.3 m/s to 18.9 m/s, keeping U_∞ constant at 89.2 m/s.

Here the most significant difference is the increase in the jet penetration for the jet with a higher q. This chiefly occurs due to an increase in the momentum of the jet, which delays its bending. Becker and Hassa[2], Hautman and Rosfjord[12] and Wu et al[36] reported similar observations. Our observation in Chapter 5 that the penetration of the jet increases with q is also in support of this finding. In addition to an increase in the penetration, there is also an increase in the extent of the shearing-off mechanism. The shearing-off mechanism will again be discussed in Chapter 7.

4.5 Effect of U_∞ on Column Behavior

The effect of a change in We by an increase in U_∞ is seen in Fig. 4.4. The Figs. 4.4 a, b show shadowgraphs of 0.381 mm jets of Jet-A at conditions of We = 99, q = 7.8 and We = 670.8, q = 8.1 respectively. U_∞ was increased from 77.9 m/s to 202.7 m/s in order to increase the aerodynamic We from 99 to 671. At the same time U_l was increased from 8.4 m/s to 22.3 m/s to maintain the value of q.

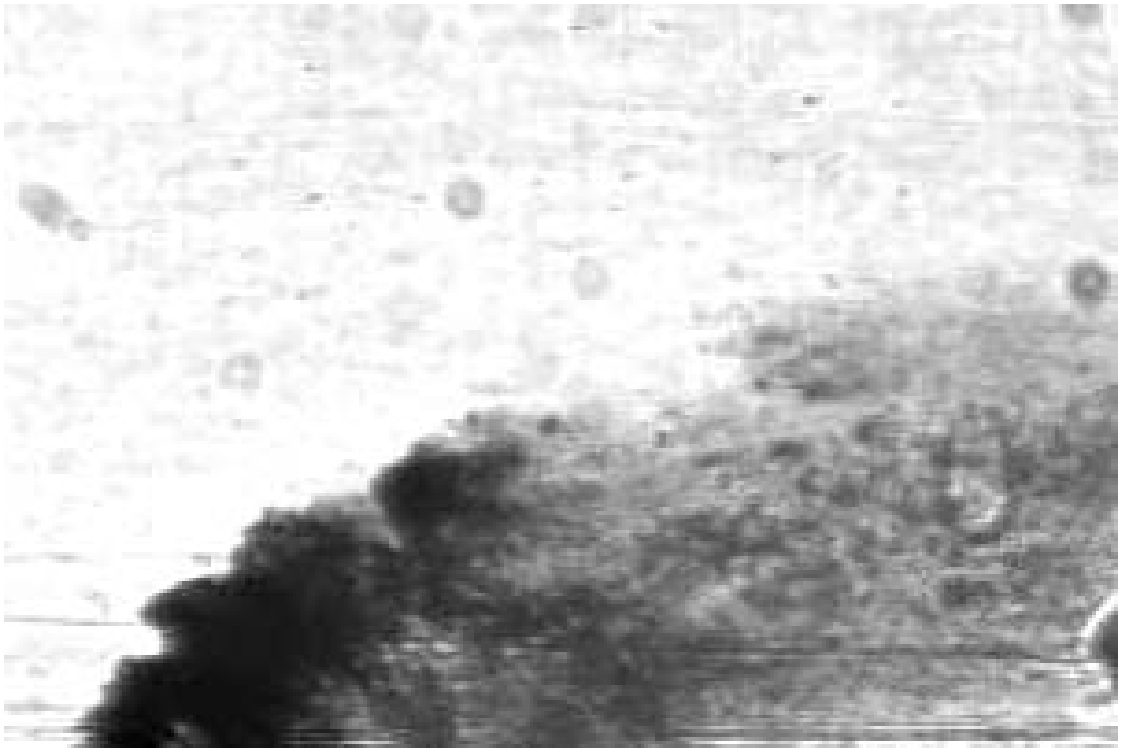

Fig. 4.3 a. Jet-A, D =0.381 mm, We = 483.4, q = 2.4

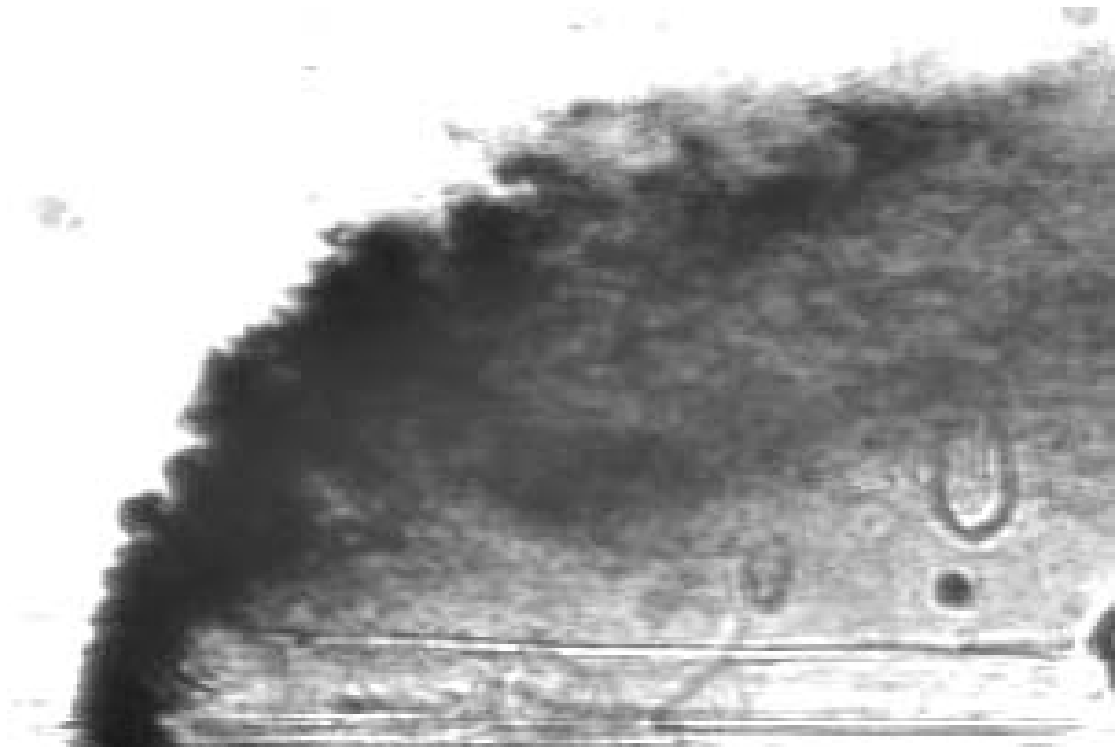

Fig. 4.3 b. Jet-A, D = 0.381 mm, We = 483.4, q = 8

Fig. 4.4 a. Jet-A, D = 0.381 mm, We = 99, q = 7.8

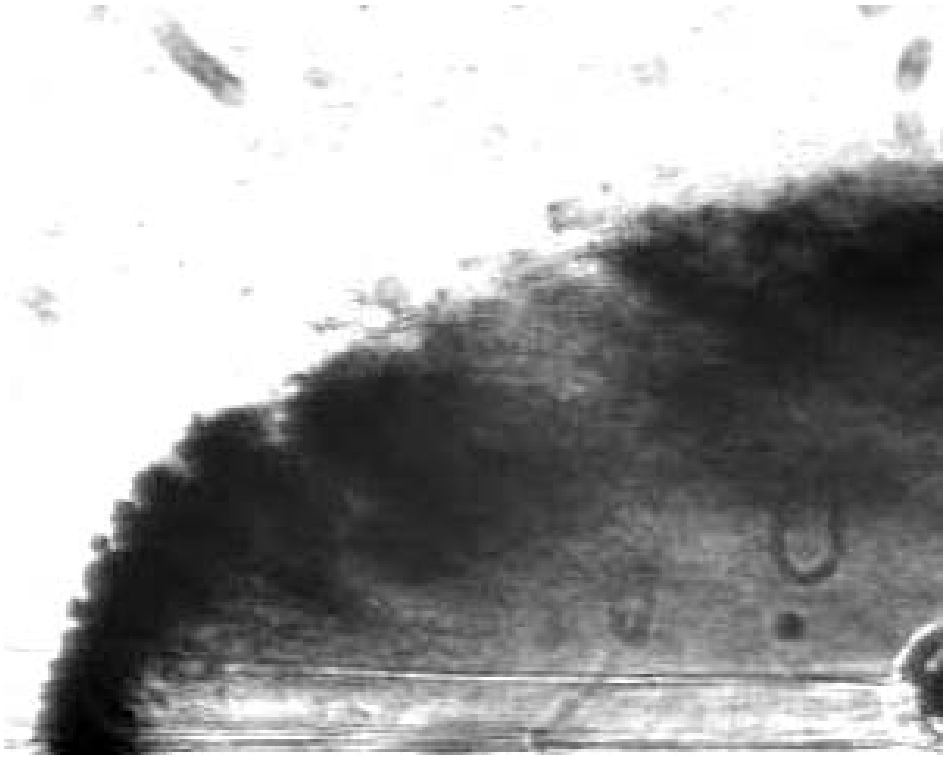

Fig. 4.4 b. Jet-A, D = 0.381 mm, We = 670.8, q = 8.1

We observe similar levels of penetration for both cases. However, the higher U_∞ exhibits a significantly higher extent of surface breakup due to a much higher extent of the droplet shearing-off mechanism. The higher shearing is caused because of higher dynamic pressure of the airstream in the case of the higher We. Thus the We = 99 jet will be labeled as occurring in the mixed mode of breakup, while the We = 671 jet will be labeled as the surface breakup mode due to the more extensive stripping-off mechanism. The breakup modes mentioned above will be described in the next chapter. Similar results have been observed by Becker and Hassa[2] and Wu et al[36]. One more difference is that the We = 671 jet appears to be thicker than the We = 99 jet, but that can be mostly attributed to the higher liquid flow rate for that case.

4.6 Effect of D on Column Behavior

Fig. 4.5 shows the effects of the nozzle diameter, D on the evolution of the jet. Jet-A jets of diameters 0.381 mm and 0.762 mm are shown in Figs. 4.5 a, b respectively. An increase in D increases We, all other parameters being kept constant. The 0.381 jet is at conditions of We = 670.8 and q = 8.1, while the 0.762 mm jet is at conditions of We = 981.5 and q = 7.9. U_∞ for the two cases are 202.7 m/s and 173.4 m/s while U_l values were 22.3 m/s and 18.9 m/s respectively. Even though the velocity for the 0.762 jet is slightly smaller, the volume flow rate is much higher owing to the larger injection diameter. Also, we note that the momentum ratio, q is almost same for both cases.

The most striking difference between the two cases is the significantly higher penetration for the larger diameter jet[14]. This will be corroborated in Chapter 5 where we will see that the jet

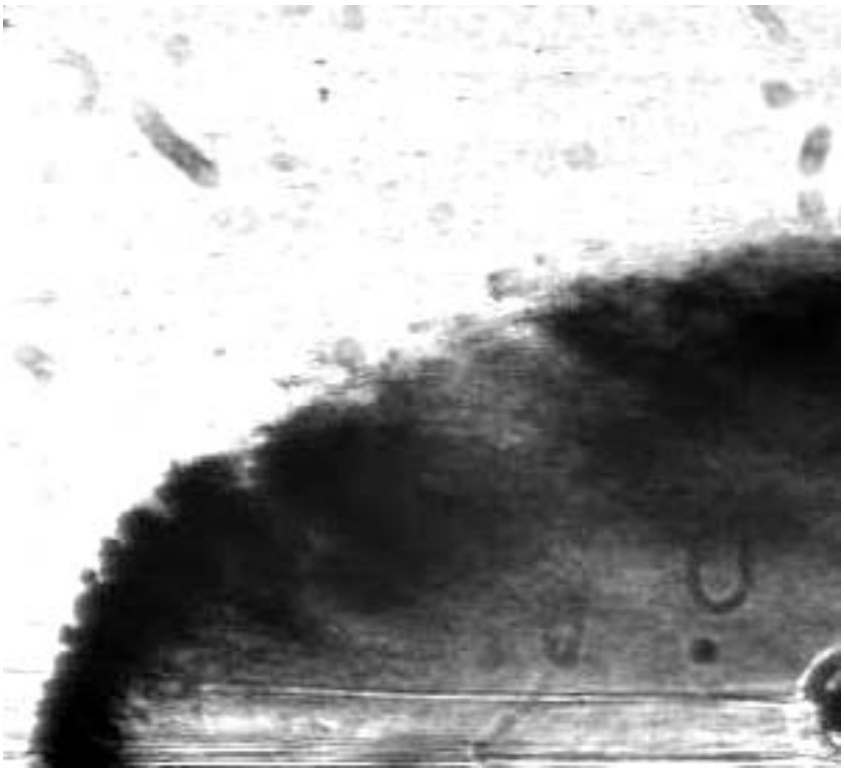

Fig. 4.5 a. Jet-A, D = 0.381 mm, We = 670.8, q = 8.1

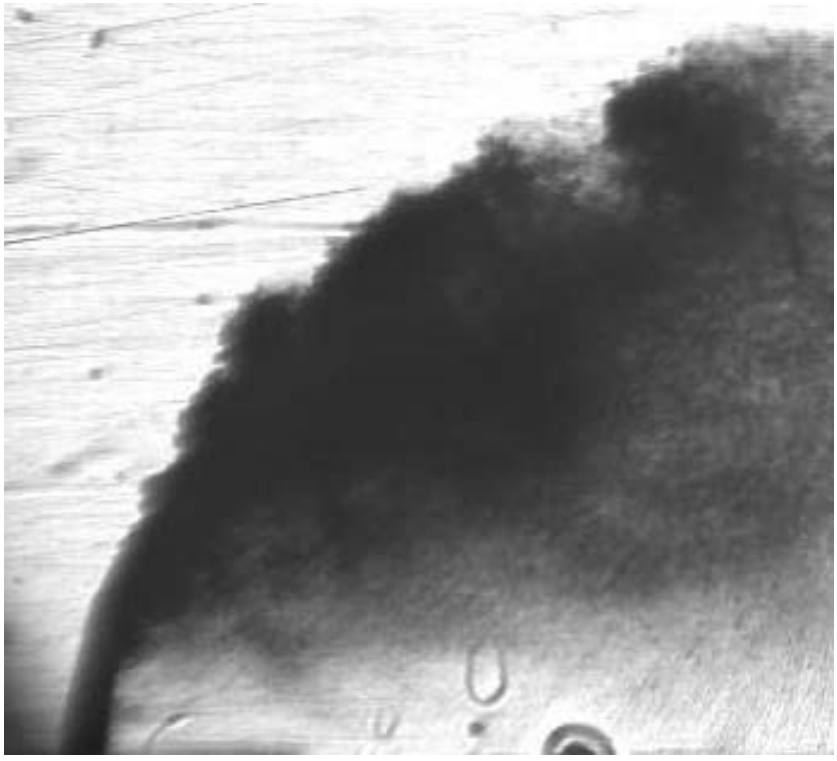

Fig. 4.5 b. Jet-A, D = 0.762 mm, We = 981.5, q = 7.9

penetration is directly proportional to the jet diameter. Also we observe that the larger diameter jet starts to bend at a further location as compared to the small diameter jet. The explanation for this phenomenon lies in the larger mass flux of the jet. At the same injection velocities, the liquid flux from the larger diameter nozzle is much higher due to which, it has greater inertia. Due to this increase in the inertia of the jet, the crossflow dynamic pressure experiences a greater opposition in causing the jet to bend, due to which the jet bending is delayed. This causes an increase in penetration of the jet even at the same injection velocity.

4.7 Effect of σ on Column Behavior

Fig. 4.6 shows the effects of σ of the injected liquid on the behavior of the jet column. Fig. 4.6 a, b and c show the evolution of 0.381 mm jets of water, Jet-A and N-Heptane respectively. The water jet is at conditions of We = 247.6, q = 7.1, the Jet-A jet is at conditions of We = 295, q = 7.1 and the conditions of the N-Heptane jet are We = 301.6, q = 6.8. We observe very similar penetrations for all three jets. Also all three jets exhibit the same breakup mode, surface breakup, which will be examined in detail in Chapter 7. However, a marked difference can be observed in the droplet sizes produced. The water jet produces large droplets, while Jet-A and N-Heptane jet produce smaller droplets. The change in the behavior, in spite of almost constant q and We values, arises due to the different σ values for these liquids. Surface tension forces try to minimize the surface area of the droplets. Hence the lower σ allows for the formation of smaller droplets. However, due to the higher surface tension of water ($\sigma = 72 \times 10^{-3}$ N/m), droplet breakup is reduced in its extent, leading to the presence of relatively larger droplets. The sizes of the droplets produced by the Jet-A ($\sigma = 28 \times 10^{-3}$ N/m) and N-Heptane ($\sigma = 21.4 \times 10^{-3}$ N/m) jets are

Fig. 4.6 a. Water, D = 0.381mm, We = 247.6, q = 7.1

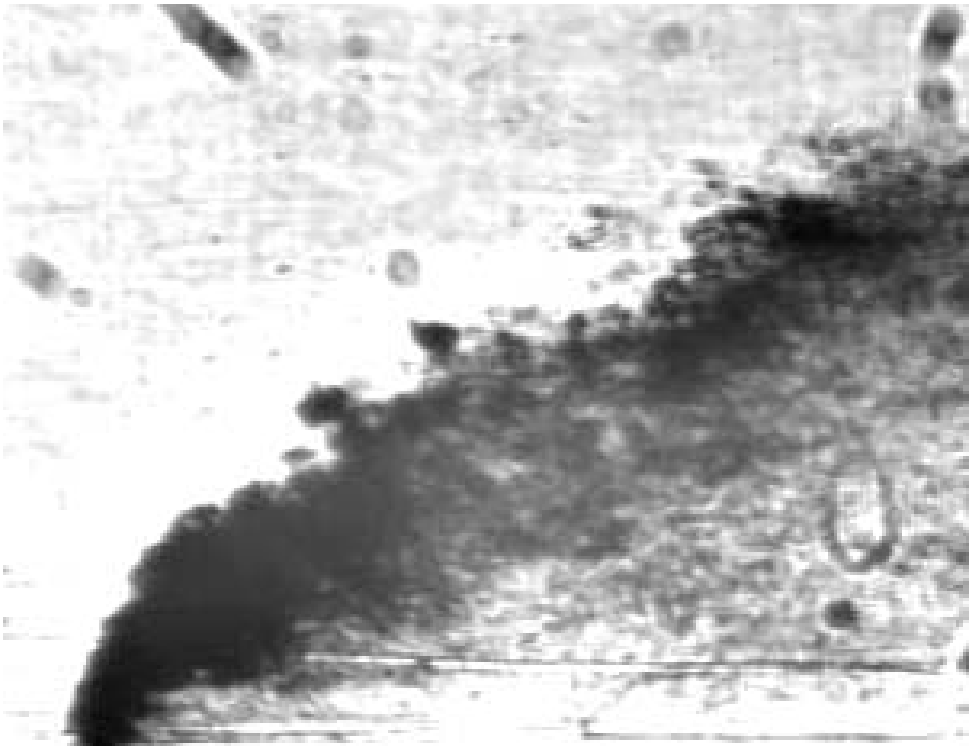

Fig. 4.6 b. Jet-A D = 0.381 mm, We = 295, q = 7.1

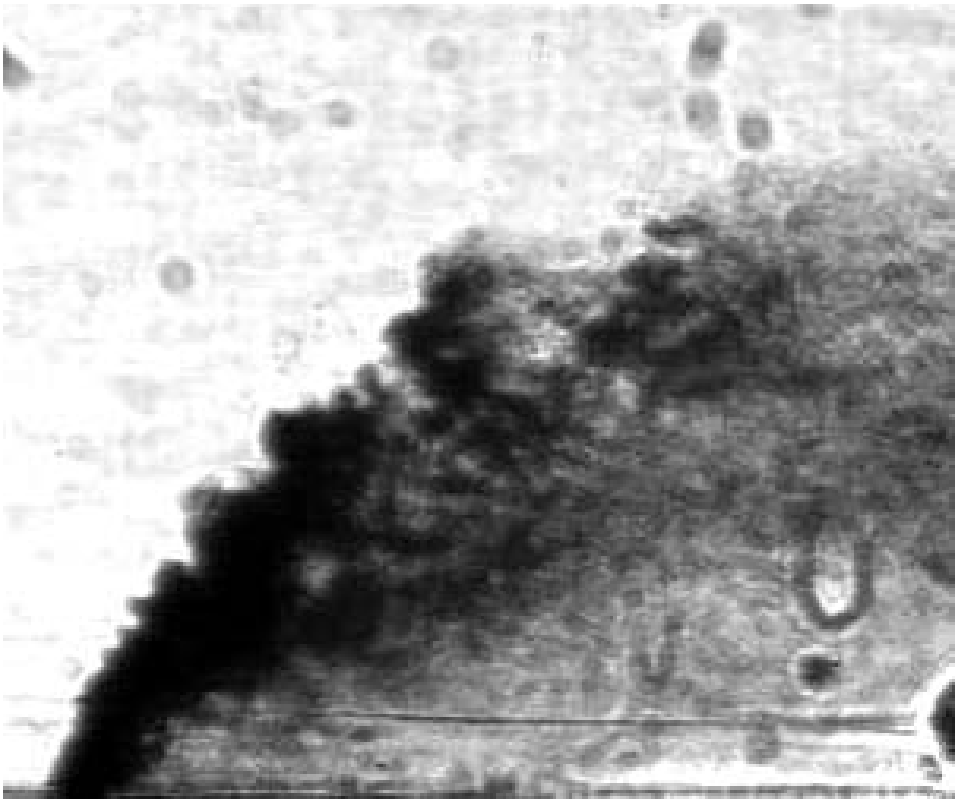

Fig. 4.6 c. N-Heptane D = 0.381 mm, We = 301.6, q = 6.8

not distinguishable due to the very small difference in their surface tensions, as compared to the difference between the σ values Jet-A (or N-Heptane) and water.

Chapter 5: Results and Discussion - PDPA Measurements and Cross-Sectional Spray Distributions

5.1 Overview of PDPA Analysis

PDPA analysis was used to study the distributions of the spray produced as a result of the breakup of the liquid jet injected into a crossflow. The PDPA instrumentation and setup has already been described in section 3.5.

PDPA measures the SMD, droplet axial velocities (U_d) and the volume flux of the liquid spray. We are interested in determining the near-field breakup characteristics. Hence PDPA analysis was carried out in the region just after the breakup of the jet column.

While applying the PDPA analysis, care should be taken to choose the analysis plane that consists only of droplets and not the intact column, since it can only detect objects having a size less than the probe volume. Here, we have conducted the analysis at three planes for each test condition. These were the center plane and two cross-sectional planes. The cross-sectional planes were chosen to be at z/D values of 30 and 65, which for the 0.381 mm jets were at 11.5 mm and 25 mm downstream, and for the 0.762 mm the planes were at 23 mm and 50 mm downstream.

Table 5.1 Summary of PDPA Test Conditions

Case No	Acronym	Liquid	D	We	q
1	J_100_5	Jet-A	0.015	94.8	5.2
2	J_100_10	Jet-A	0.015	94.8	10.1
3	J_500_5	Jet-A	0.015	471.7	5.1
4	J_500_10	Jet-A	0.015	471.7	10.3
5	J_1200_5	Jet-A	0.03	1148.6	5
6	J_1200_10	Jet-A	0.03	1148.6	10.1
7	N_1200_5	N-heptane	0.03	1150.6	4.8
8	W_100_5	Water	0.015	96.2	5.2
9	W_100_10	Water	0.015	96.2	10.4

A summary of the various test conditions is given in Table 5.1. Table 5.2 lists the details of the parameters used for each test case. For ease of notation, here forth, the cases will be represented by their acronyms, with the corresponding plane added in parentheses. For example, J_100_5 (11.5 mm) will represent the case of a 0.381 mm jet of Jet-A at We = 94.8 and q = 5.2. Case J_100_5 (11.5 mm), was taken as the baseline case, and all other cases were designed to study the influence of variation of some properties on the spray distribution. The plane of z/D = 30, which for this case is 11.5 mm was considered as the baseline cross-sectional plane.

Before we continue on to discuss the cross sectional variations, we note that the liquid flow rate, as obtained from integrating the volume fluxes, computed by the PDPA, over the entire area, was found to differ significantly from the liquid flow rate measured by the coriolis flowmeter. The reasons for this difference could be the sensitivity of the PDPA technique and the presence of some ligaments which may still have persisted at these locations. These ligaments are beyond the threshold of the PDPA measurement volume and hence will go

undetected. Due to this, all discussions regarding the distributions of volume flux will be treated on a qualitative level only. No values will be given.

Table 5.2 Details of PDPA Test Cases

Acronym	Section	U_∞	U_l	U_d max	U_d min	SMD max	SMD min
J_100_5	11.5	76.2	6.7	49.4	23.2	89.5	33
J_100_5	25	76.2	6.7	63.2	44.5	73.3	45.6
J_100_5	center	76.2	6.7	63.9	12.1	66.3	41
J_100_10	11.5	76.2	9.4	57	37.2	61.4	23.4
J_100_10	25	76.2	9.4	66.1	44.6	80.7	37.4
J_100_10	center	76.2	9.4	83.4	19.1	66.8	26.4
J_500_5	11.5	170	14.9	110.4	53.1	42.4	20.5
J_500_5	25	170	14.9	127.9	83.4	42.5	18.7
J_500_5	center	170	14.9	130.6	32.6	62.4	26.5
J_500_10	11.5	170	21.1	114.7	59.7	44.1	17.2
J_500_10	25	170	21.1	131.7	87.5	45.9	16.1
J_500_10	center	170	21.1	123.3	43.7	60.6	21
J_1200_5	23	187.5	16.3	159	49.4	56.5	16.5
J_1200_5	50	187.5	16.3	181.6	23.6	87.6	14.1
J_1200_5	center	187.5	16.3	185.2	22	64.7	14.3
J_1200_10	23	187.5	23.1	152	59.3	45	14.7
J_1200_10	50	187.5	23.1	188.3	110.5	44.7	15.6
J_1200_10	center	187.5	23.1	160.2	31.5	63.3	14.4
N_1200_5	23	123.1	9.7	140.8	54.8	43.2	18.6
N_1200_5	50	123.1	9.7	156.9	100.9	29.1	16.07
N_1200_5	center	123.1	3.7	158.2	18.5	67.1	18.1
W_100_5	11.5	123.1	13.8	65.8	34.4	51.9	39
W_100_5	25	123.1	13.8	79.9	52.5	66.8	42.1
W_100_5	center	123.1	13.8	88.7	18.5	68.4	35.4
W_100_10	11.5	164.1	15.1	75.6	40.7	48.7	27
W_100_10	25	164.1	15.1	84.2	27.8	80.8	27.1
W_100_10	center	164.1	15.1	83.3	19.1	66.8	26.4

The rest of this chapter will study the distribution of the spray in the cross-sectional planes. The spray distribution in the center plane will be the subject of discussion in Chapter 6.

5.2 Cross-Sectional Spray Distributions for the Baseline Case

Fig. 5.1 shows the cross-sectional variations for the baseline case, J_100_5 (11.5 mm). As seen from table 5.2, J_100_5 denotes a 0.381 mm jet of Jet-A conditions of We = 94.8, q = 5.2, U_∞ = 76.2 m/s and U_l = 6.7 m/s. Figs. 5.1 a, b and c show the plots for the SMD, axial velocity and the volume flux respectively.

The SMD is seen to vary from 33 μm to 89.5 μm. A region of large droplets can be observed in the central region of the spray, which can be identified as the spray core from Fig. 5.1 c. The SMD decreases gradually as we move to the spray extremities from the core region. As we move in the direction of increasing transverse distance from the bottom wall, the SMD variation first increases and then decreases.

The axial velocity of the droplets, U_d can be seen to vary from 23.2-49.4 m/s. We observe a low velocity region in the center and lower portion of the spray plume. This is a result of the wake region located downstream and below the jet. This wake induced region is surrounded on the sides and on the top by regions of higher velocities[37]. The highest velocities are observed at the top of the spray plume[16].

The volume flux seen in Fig. 5.1 c exhibits a maximum in an area at the center of the plume. This region is obviously the core of the spray, and is also the location where the larger droplets were located. The flux gradually reduced towards the spray periphery on all sides. The spray core has been observed to be an area of high droplet concentration and also

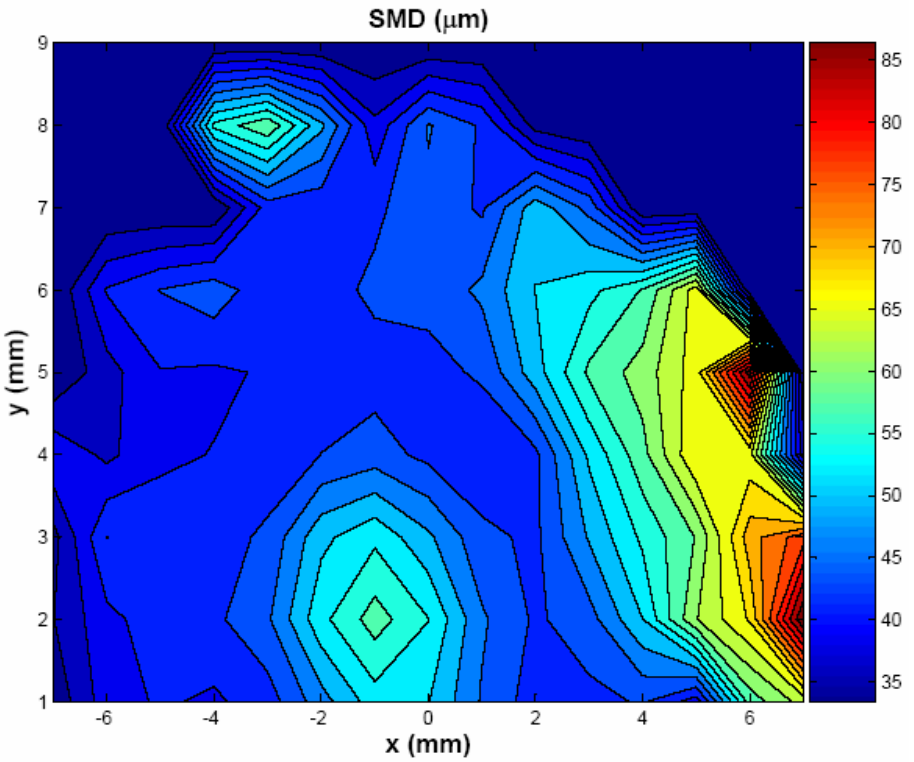

Fig. 5.1 a. SMD for Jet-A We = 94.8, q = 5.2, D =0.381 mm, z = 11.5 mm

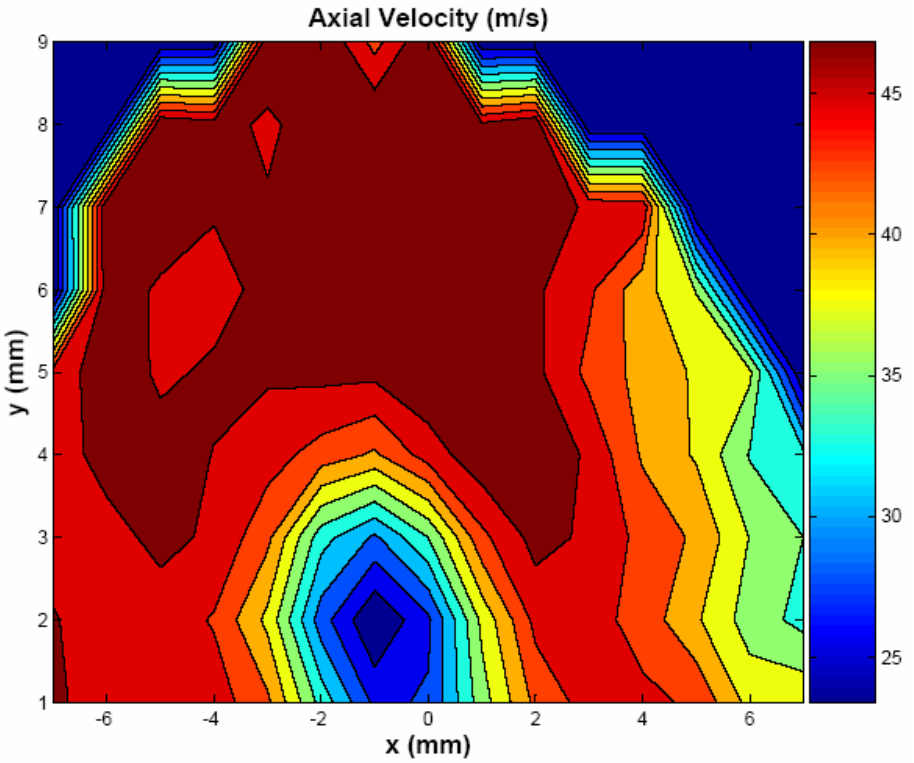

Fig. 5.1 b. Axial Velocity for Jet-A We = 94.8, q = 5.2, D = 0.381 mm, z = 11.5 mm

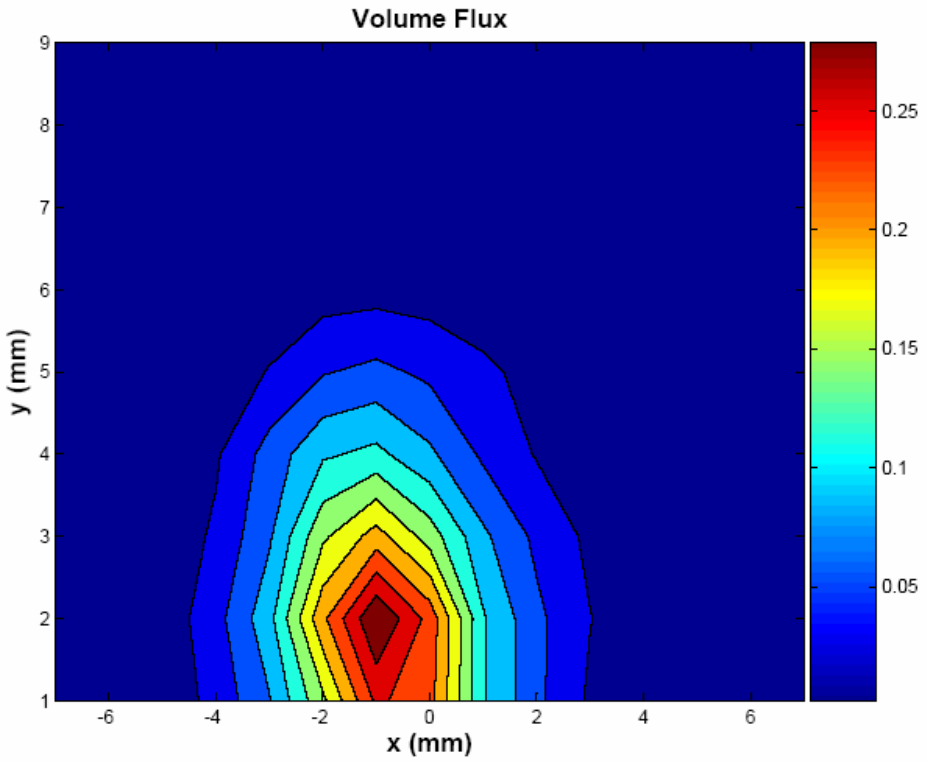

Fig. 5.1 c. Volume Flux for Jet-A We = 94.8, q = 5.2, D = 0.381 mm, z = 11.5 mm

contains a significant portion of the injected liquid. Wu et al[37] found out that 70% of the injected liquid is concentrated in 25% of the total area of the spray plume.

We observe some asymmetry in Figs. 5.1 a, b for the SMD and U_d plots. The reason for this is not clear. Some of the studies published in the literature have also reported the presence of such asymmetries in the spray flow field[33,34]. However, no reasons have been identified to explain this occurrence. Also the SMD plot indicates an area of extremely high droplet sizes in the right extreme of the spray plume. This is believed to be an error. No reasons are known for this occurrence.

The effect of various parameters on the spray distribution is then determined by comparing various cases to the baseline case spray distribution.

5.3 Effect of Streamwise Distance on Cross-Sectional Spray Distributions

Since we are studying near-field conditions, we know that the spray produced has not stabilized till it reached the end of our area of interest. Consequently, significant changes can be expected in the flow distributions as we move further downstream from the plane of the J_100_5 (11.5 mm) case. To quantify these effects we study the spray distributions for the case J_100_5 (25 mm). As denoted, the streamwise location of this plane is z/D = 65 (25 mm). The SMD, U_d and volume flux distributions at this cross-section are shown in Figs. 5.2 a, b and c respectively.

Comparing the volume flux plot of Fig. 5.2 c to the one in Fig. 5.1 c, we immediately recognize an increase in the cross-sectional area of the spray plume with an increase in the streamwise distance. Consequently, since the overall flow rate is the same, the value of the maximum flow rate has dropped, indicating a higher level of mixing with the crossflow. Also we notice a slight increase in the transverse location of the spray core, and of the spray plume in general, indicating that the spray is still rising and has not reached the maximum penetration within this streamwise distance.

U_d for this case is observed to vary from 44.5-63.2 m/s. The values of U_d are much higher than those at z/D = 30, indicating the occurrence of a significant amount of momentum exchange between these two locations. Momentum exchange is mainly a product of the entrainment of crossflow fluid, which imparts its higher momentum to the jet flow[11,39]. Also

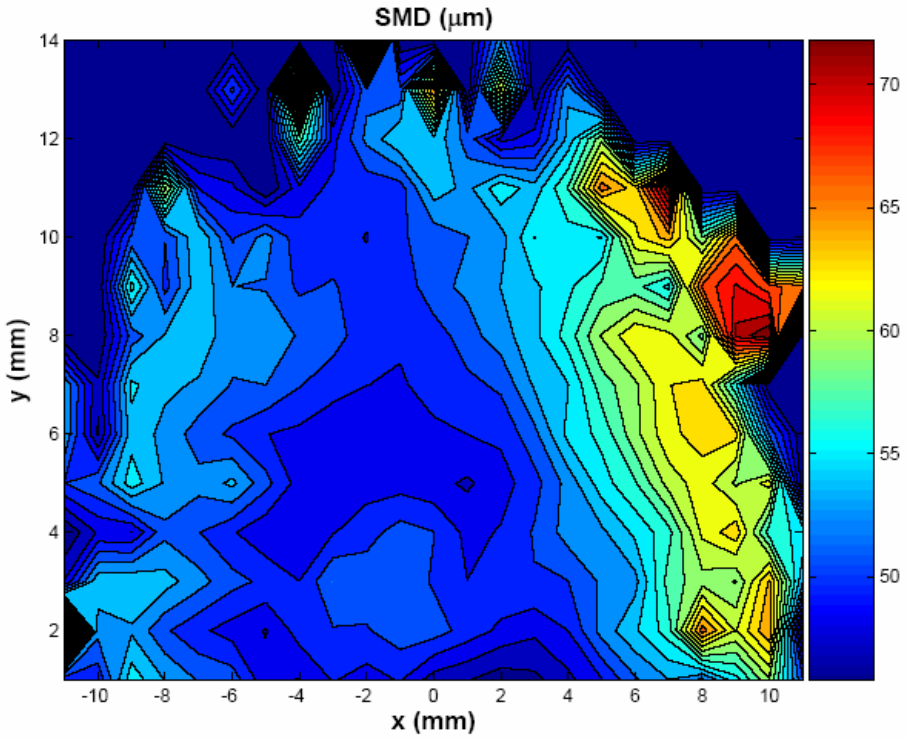

Fig. 5.2 a. SMD for Jet-A We = 94.8, q = 5.2, D = 0.381 mm, z = 25 mm

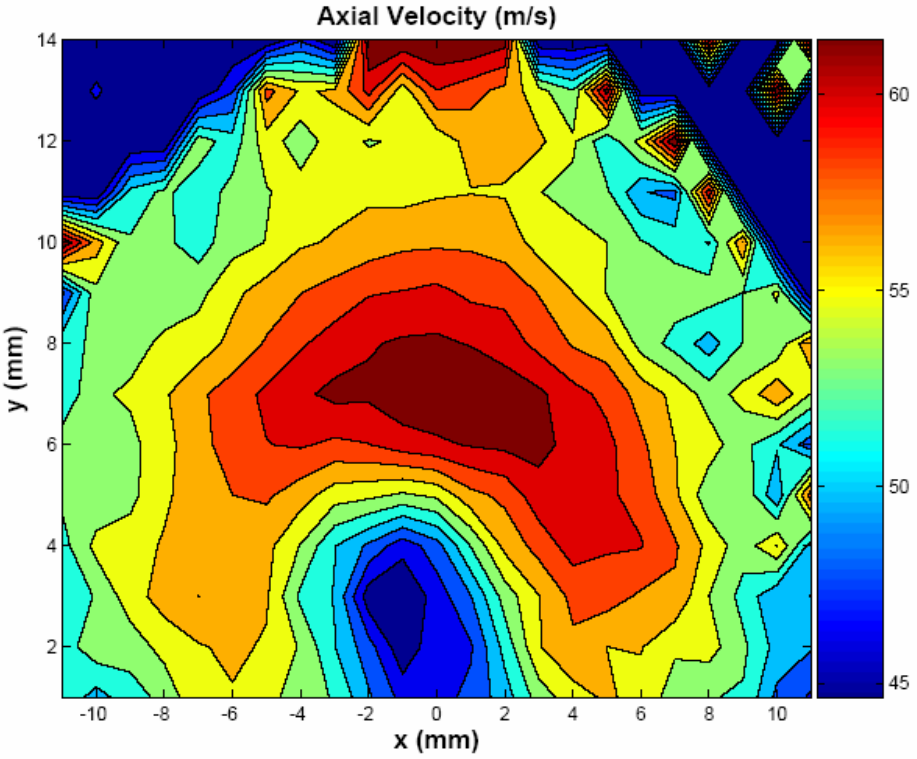

. 5.2 b. Axial Veloicty for Jet-A We = 94.8, q = 5.2, D = 0.381 mm, z = 25 mm

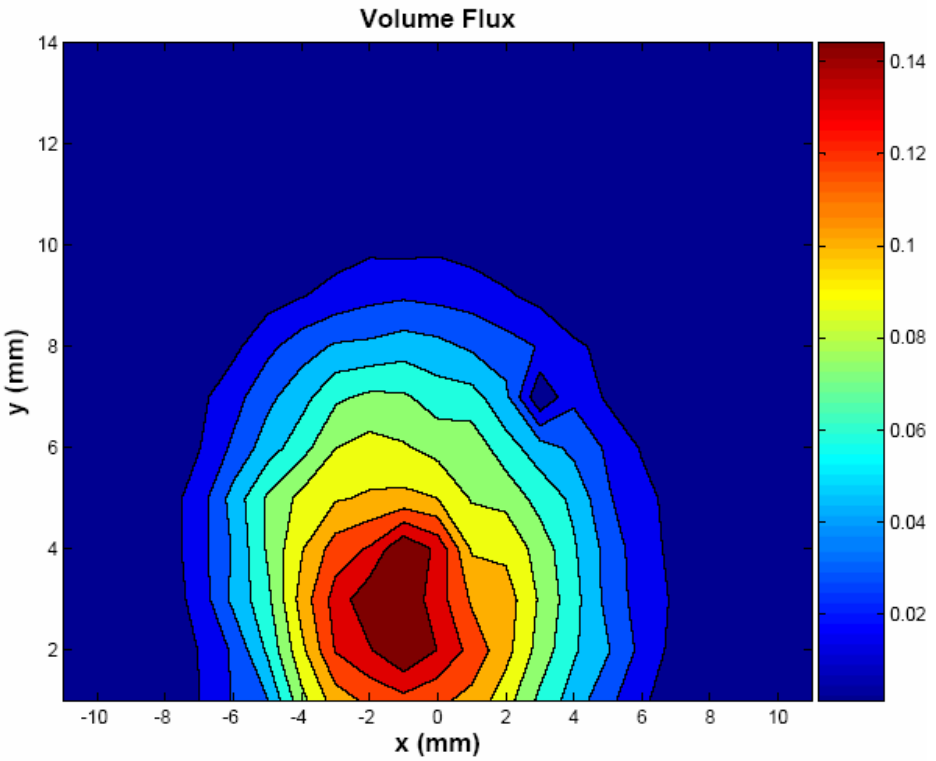

Fig. 5.2 c. Volume Flux for Jet-A We = 94.8, q = 5.2, D = 0.381 mm, z = 25 mm

the location of the maximum velocity drops down from the top of the spray plume to a location between the spray core and the top of the plume. The velocity of the droplets near the top of the plume gets reduced as a result of momentum exchange[26].

The SMD values at this location vary from 45.6 μm to 73.3 μm. We observe that the SMD range is smaller than the previous case; however, the minimum SMD is higher than the previous location. A comparison of Figs. 5.2 a. and 5.1 a show that the droplet sizes for the current case, J_100_5 (25 mm) are generally higher than the case J_100_5 (11.5 mm). The overall distribution in the plane is qualitatively similar to the earlier case.

Inamura and Nagai[16] observed that as we proceed further downstream the larger droplets start moving down due to the effect of gravity. However this effect is observed only at far

downstream locations, and no such effect was observed at the z/D = 65 cross-sectional plane.

5.4 Effect of q on Cross-Sectional Spray Distributions

From the penetration analysis we have seen that an increase in q results in an increased penetration of the jet. Here we observe its effect on the spray distributions. This effect is studied by comparing the baseline case J_100_5 (11.5 mm) to the case J_100_10 (11.5 mm), which is a 0.381 mm jet of Jet-A at conditions of We = 94.8, q = 10.1, U_∞ = 76.2 m/s and U_l = 9.4 m/s at the same z/D location of 30 (11.5 mm). The SMD, U_d and volume flux distributions for this plane are shown in Fig. 5.3 a, b and c respectively.

The volume flux plot in Fig. 5.3 c clearly shows the spray plume to be located at a higher transverse location as compared to the location in Fig 5.1 c for the baseline case. Thus an increase in q leads to an increase in the spray penetration. Except for the penetration, the volume flux distribution is similar to the distribution for the baseline case.

The SMD values for this spray vary from 23.4-61.4 μm. We observe the maximum as well as the minimum SMD values for this case (61.4 μm and 23.4 μm) are lesser than the corresponding values for the baseline case J_100_5 at 11.5 mm (89.5 μm and 33 μm). Moreover the range of SMD for the current case is smaller. One possible reason for the relatively higher droplet sizes of the baseline J_100_5 case could arise from the lesser penetration of the baseline case. It is much nearer to the wall, due to which there is a possibility of droplet impingement of the chamber wall, which raises the SMD of the spray,

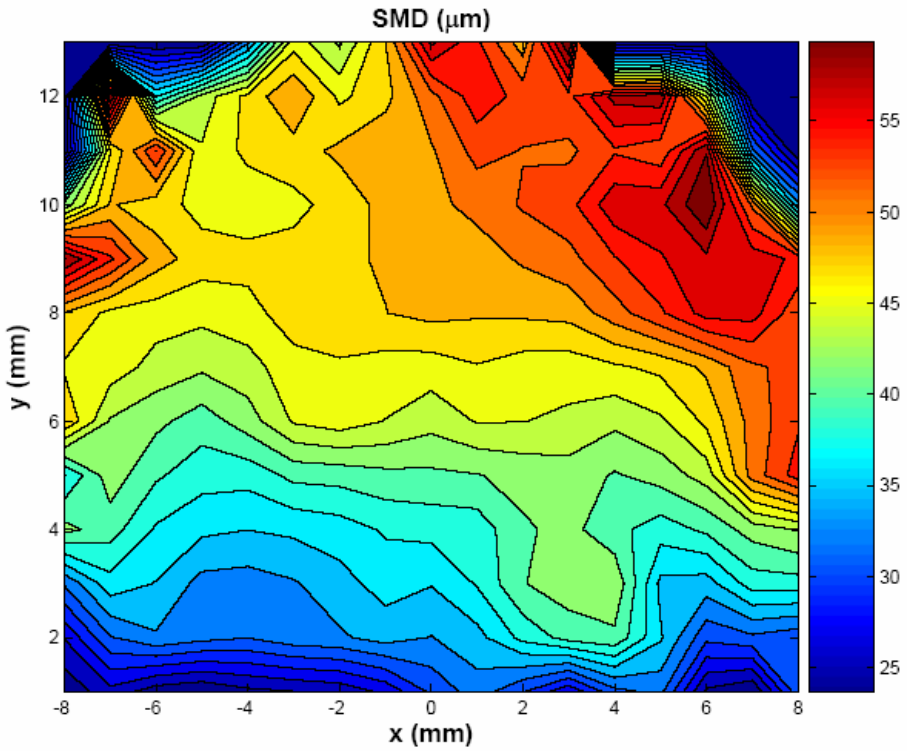

Fig. 5.3 a. SMD for Jet-A We = 94.8, q = 10.1, D = 0.381 mm, z = 11.5 mm

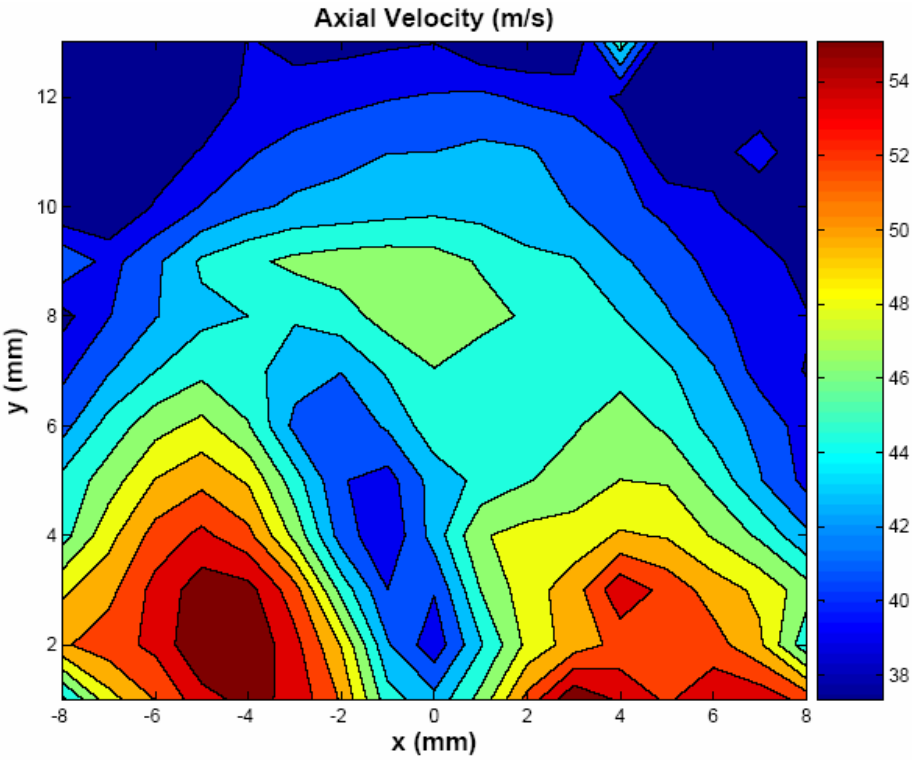

Fig. 5.3 b. Axial Velocity for Jet-A We = 94.8, q = 10.1, D = 0.381 mm, z = 11.5 mm

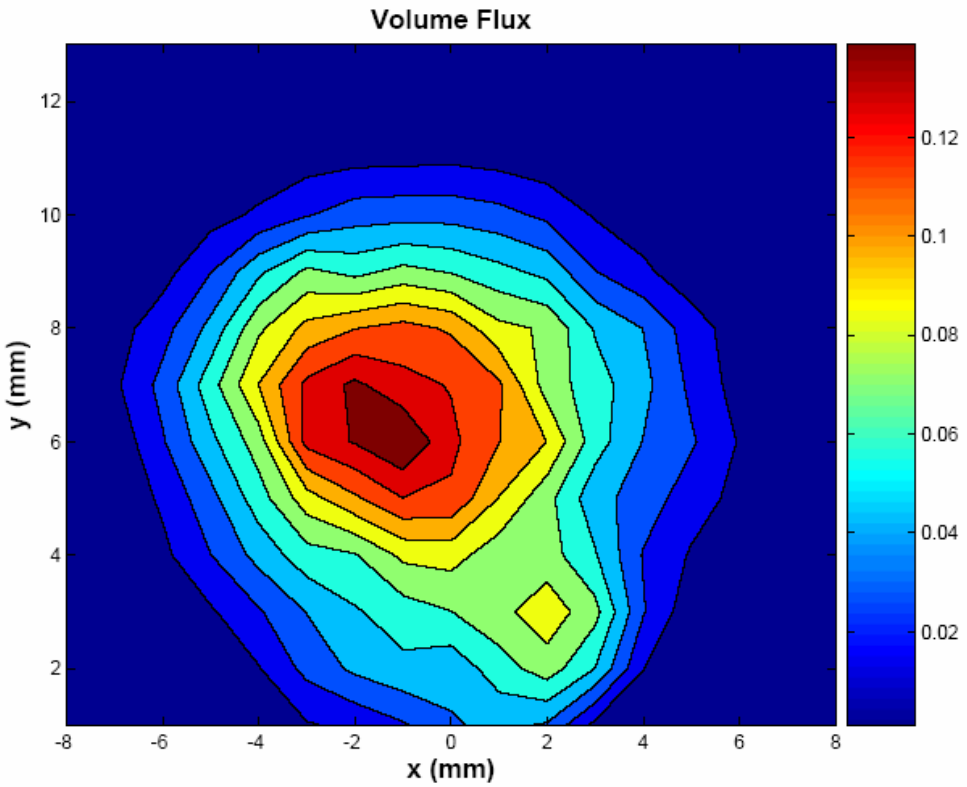

Fig. 5.3 c. Volume Flux for Jet-A We = 94.8, q = 10.1, D = 0.381 mm, z = 11.5 mm

according to Wu et al[37]. This occurrence is avoided in the current case due to the increased penetration.

Another possible reason for a reduction in the lower bound of the SMD could be the greater extent of droplet shearing in this case. From the breakup mode map, we see that both the baseline case J_100_5 and the current case J_100_10 fall under the mixed mode of breakup. However, the case J_100_10 is much closer to the surface breakup zone, signifying a much larger extent of surface breakup. The droplets produced due to surface breakup are much smaller than those produced by column breakup, which might be responsible for the smaller droplets appearing in the current case.

For this case, SMD is observed to increase monotonically with transverse distance, with a maximum at the periphery of the spray plume, as opposed to the SMD peaking in the spray core region for the baseline case. This is in accordance with the findings of Wu et al[37] and Inamura and Nagai[16] who observed that the maximum location for SMD for low q occurs in the spray core, while for higher q, it occurs at the spray periphery. This happens because for a relatively low U_∞ (high q), larger droplets penetrate into the airstream and some of them are able to reach the boundary of the spray plume. However, at high U_∞ (low q), even the larger droplets are not able to penetrate very far into the crossflow due to the large aerodynamic force. In such a case the periphery is dominated by finer droplets that are sheared off from the jet's surface[16].

U_d values are observed to vary from 37.2-57 m/s. These values are higher than the corresponding values for the baseline J_100_5 (11.5 mm) case, which is essentially due to the higher liquid momentum, since U_∞ is constant. Two high velocity areas are observed on the lateral sides of the spray core. However the velocity in the region above the spray core is less due to the momentum exchange.

5.5 Effect of U_∞ on Cross-Sectional Spray Distributions

We study the effect of increasing the We by increasing the crossflow velocity, U_∞. For this we compare the baseline J_100_5 (11.5 mm) to the J_500_5 (11.5 mm), which denotes a 0.381 mm jet of Jet-A at conditions of We = 471.6, q = 5.1, U_∞ = 170 m/s and U_l = 14.9 m/s at z/D = 30 (11.5 mm). Before we start comparing the two cases we note that the J_100_5 case exhibits the mixed breakup mode while the current J_500_5 case falls under

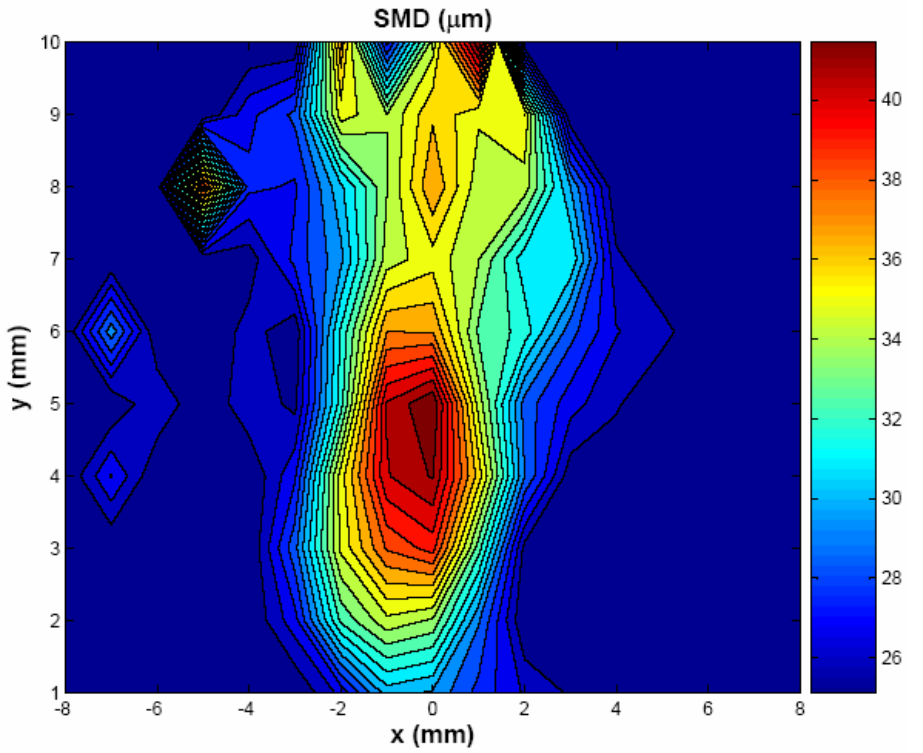

Fig. 5.4 a. SMD for Jet-A We = 471.6, q = 5.1, D = 0.381 mm, z = 11.5 mm

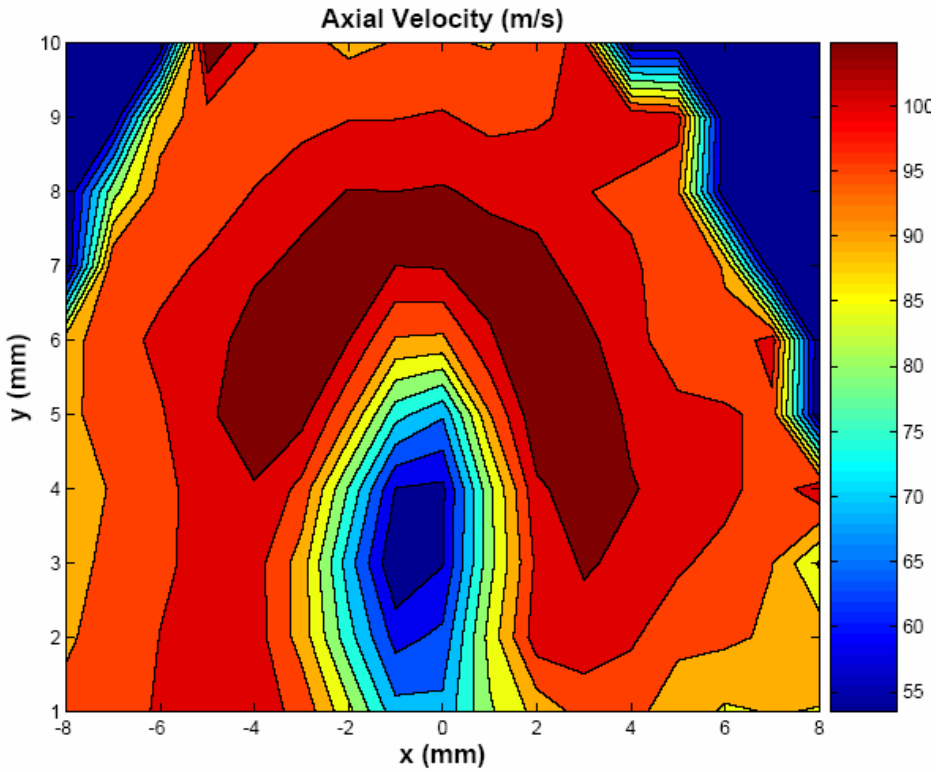

Fig. 5.4 b. Volume Flux for Jet-A We = 471.6, q = 5.1, D = 0.381 mm, z = 11.5 mm

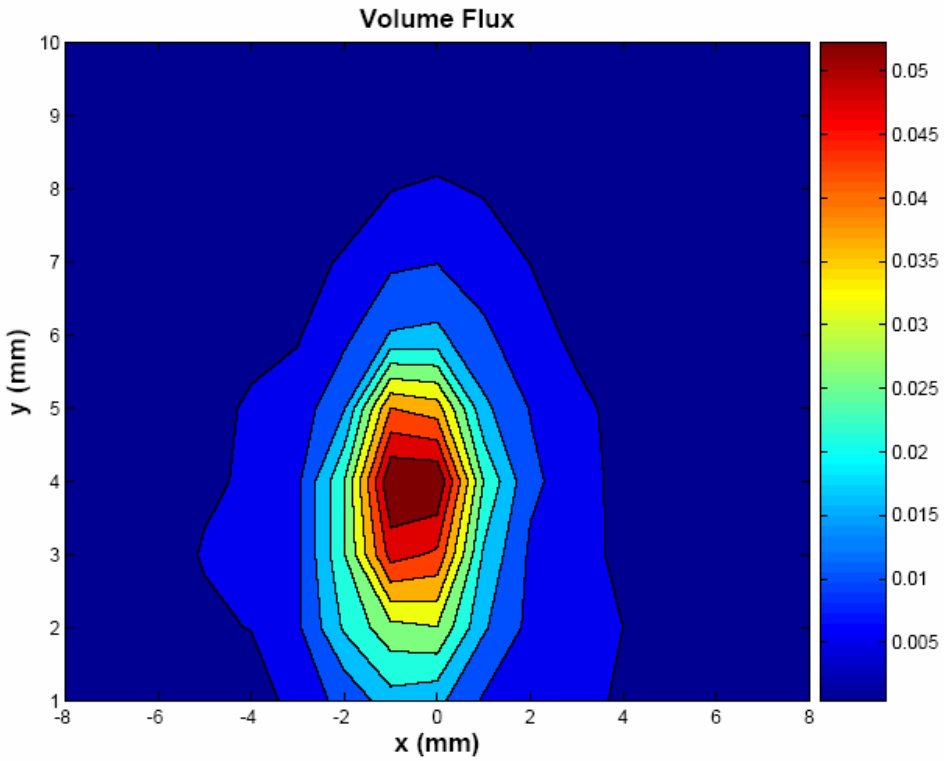

Fig. 5.4 c. Volume Flux for Jet-A We = 471.6, q = 5.1, D = 0.381 mm, z = 11.5 mm

the surface breakup mode, as will be seen in Chapter 7. U_∞ has been increased from 76.2 m/s for J_100_5 to 170 m/s for J_500_5.

The SMD, U_d and volume flux plots for the current case are shown in Fig. 5.4 a, b and c respectively. The SMD is seen to vary from 20.5-42.4 μm. We observe that both the maximum and minimum SMD values are much lesser than in any of the previous cases. This indicates that an increase in We generates more effective atomization[12,14,16,37,40]. Here, it is noted that an increase in We is brought about by an increase in the dynamic pressure of the crossflow which has the effect of increasing the extent of surface breakup. Thus atomization is improved by increasing the dynamic pressure of the crossflow. Additionally the SMD range is quite lesser than that for the previous high q case. This indicates a more uniform distribution of the droplets in the spray plume, which is a sign of better mixing with the

crossflow fluid. The SMD distribution is similar to the low q baseline case with a maximum in the core region.

The values of U_d vary from 53.1-110.4 m/s, where the high values are primarily due to the high crossflow velocity[16]. The volume fluxes are very low, and the distribution is similar to the baseline case with a maximum in the core of the spray plume.

5.6 Effect of D on Cross-Sectional Spray Distributions

We study the effect of changing the We through an increase in the jet diameter by comparing the spray for the J_1200_5 (23 mm) case at z/D = 30 to the previous J_500_5 case at z/D = 30 (11.5 mm). We note that both have similar U_∞ values (187.5 m/s for J_1200_5 and 170 m/s for J_500_5); which indicates that the increase in We is purely due to the increase in D. The J_1200_5 case denotes a 0.762 mm jet of Jet-A at conditions of We = 1148.5, q = 5, U_∞ = 187.5 m/s, U_l = 16.3 m/s. Fig. 5.5 a, b and c show the SMD, U_d and volume flux variations, respectively for the J_1200_5 case.

SMD has been observed to vary from 16.5-56.5 μm, while U_d varies from 49.4-159 m/s. The minimum SMD for this case (16.5 μm) is lower than the minimum value for the J_500_5 case (20.5 μm). However the maximum SMD value (56.5 μm) is much higher than the corresponding value for the previous case (42.4 μm). This shows that even though a few smaller droplets might have been produced, the increase in the jet diameter did not lead to any improvement in the overall atomization is spite of the slightly higher U_∞ for this case.

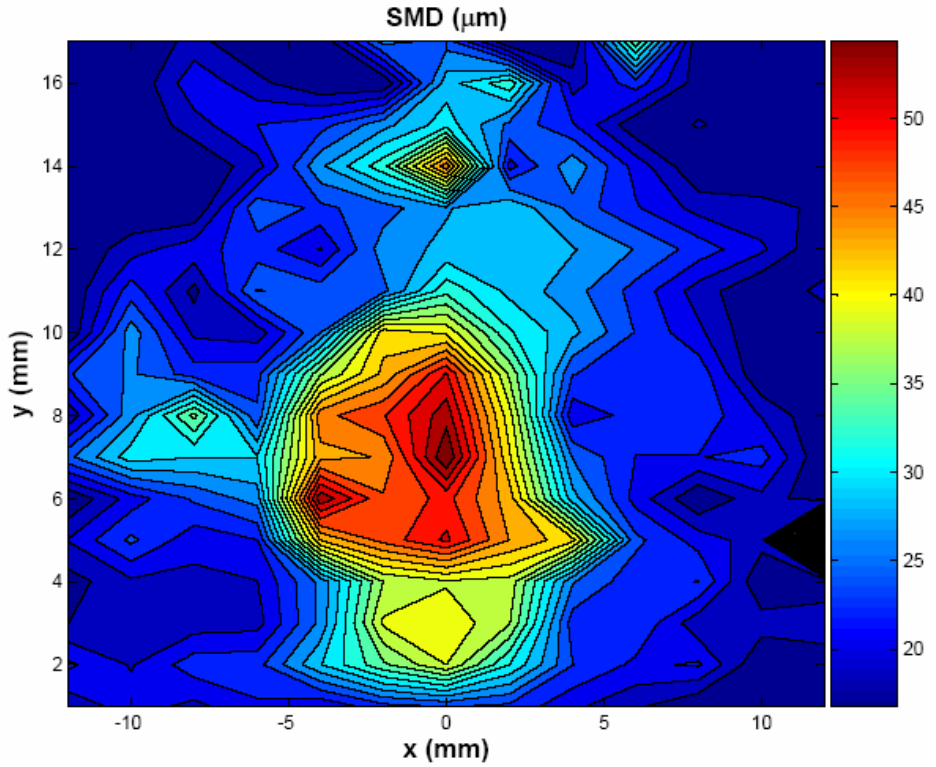

Fig. 5.5 a. SMD for Jet-A We = 1148.5, q = 5, D = 0.762 mm, z = 23 mm

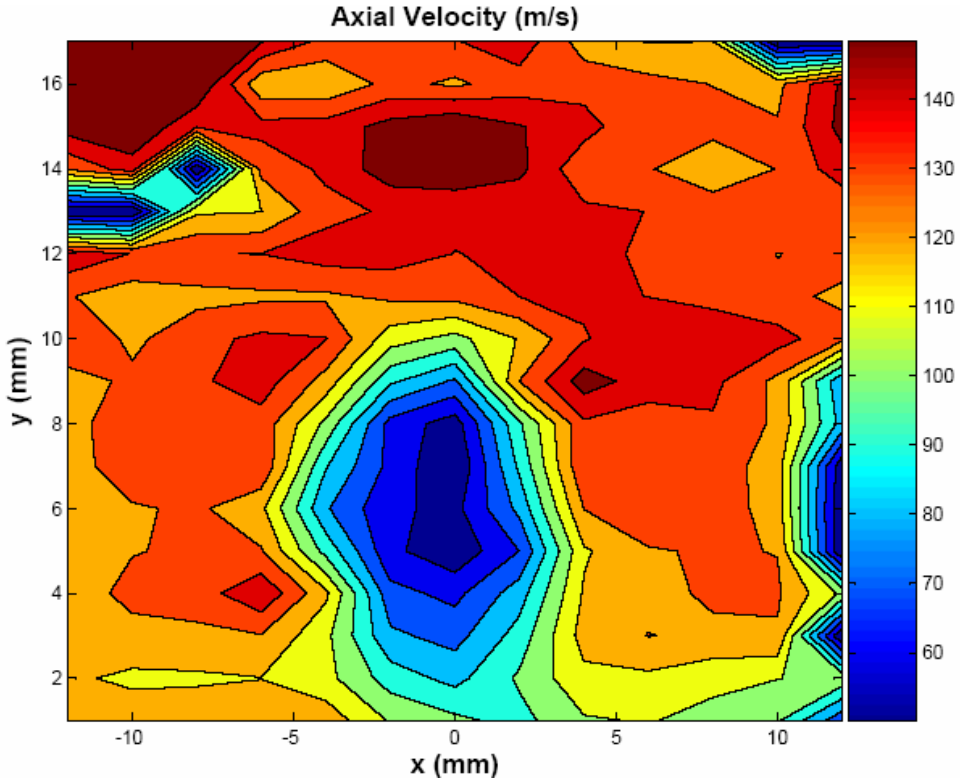

Fig. 5.5 b. Axial Velocity for Jet-A We = 1148.5, q = 5, D = 0.762 mm, z = 23 mm

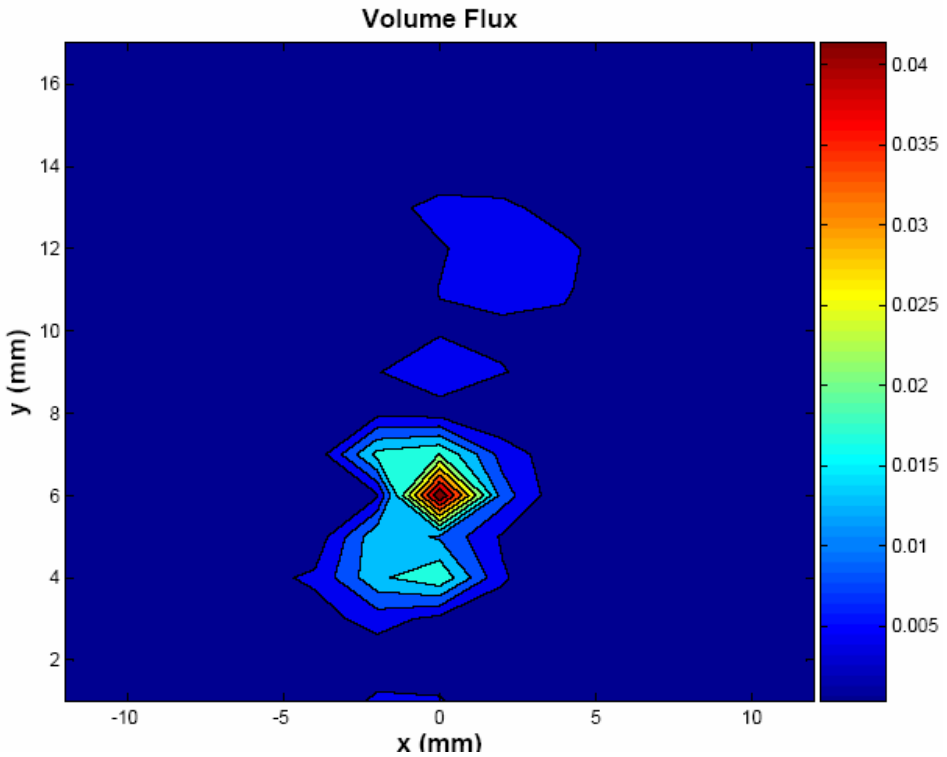

Fig. 5.5 c. Volume Flux for Jet-A We 1148.5, q 5, D =0.762 mm, z = 23 mm

The variation of both SMD and U_d are similar to the previous case, except for the location of the spray core, which occurs at a much higher transverse location. The same thing is observed in the plot of the volume flux, indicating that the penetration for the 0.762 mm jet is much higher than for the 0.381 mm jet. A similar observation was seen in section 4.6 where the higher penetration was related to an increased resistance to bending of the jet due to the higher mass flux.

Thus we conclude that increasing the jet diameter increases the penetration but has little or no effect on the atomization of the spray.

5.7 Effect of σ on Cross-Sectional Spray Distributions

We now consider the effect of surface tension of the liquid on the spray atomization. For this we compare the spray properties of N-Heptane and water jets with those of Jet-A at similar conditions.

The case N_1200_5 (23 mm), which is a 0.762 mm N-Heptane jet at conditions of We = 1150.6, q = 4.8, U_∞ = 164.1 m/s, U_l = 15.1 m/s, observed at z/D = 30 (23 mm) is compared with case J_1200_5 (23 mm) observed in the previous section. U_∞ for this case is observed to be smaller than the J_1200_5 case, which had a U_∞ value of 187.5 m/s. The SMD plot for the N-Heptane jet is shown in Fig. 5.6. The SMD for the N-Heptane jet is found to vary from 18.6-43.2 μm. We observe that though the minimum SMD value for this case is slightly bigger than the J_1200_5 case, the overall SMD values are lesser than the corresponding values for the J_1200_5 case.

Next we compare the spray produced by case W_100_5 (11.5 mm), which is a 0.381 water jet at conditions of We = 96.2, q = 5.2, U_∞ = 123.1 m/s, U_l = 9.7 m/s to the baseline case J_100_5 at the same z/D location. Fig. 5.7 shows the SMD plot for the water jet. The range of the SMD for the water jet is 39.0-51.9 μm. The SMD range for the corresponding Jet-A case is 33-89.5 μm. Even though the droplets for the baseline Jet-A case seem to be slightly higher than the water jet, we observe that the crossflow velocity for the baseline case was 76.2 m/s, which is much lesser than the corresponding value for the case of the water jet, 123.1 m/s. Also the minimum SMD for the baseline J_100_5 case is still smaller than the corresponding value for the current case. We have observed, in section 5.5 that increase in

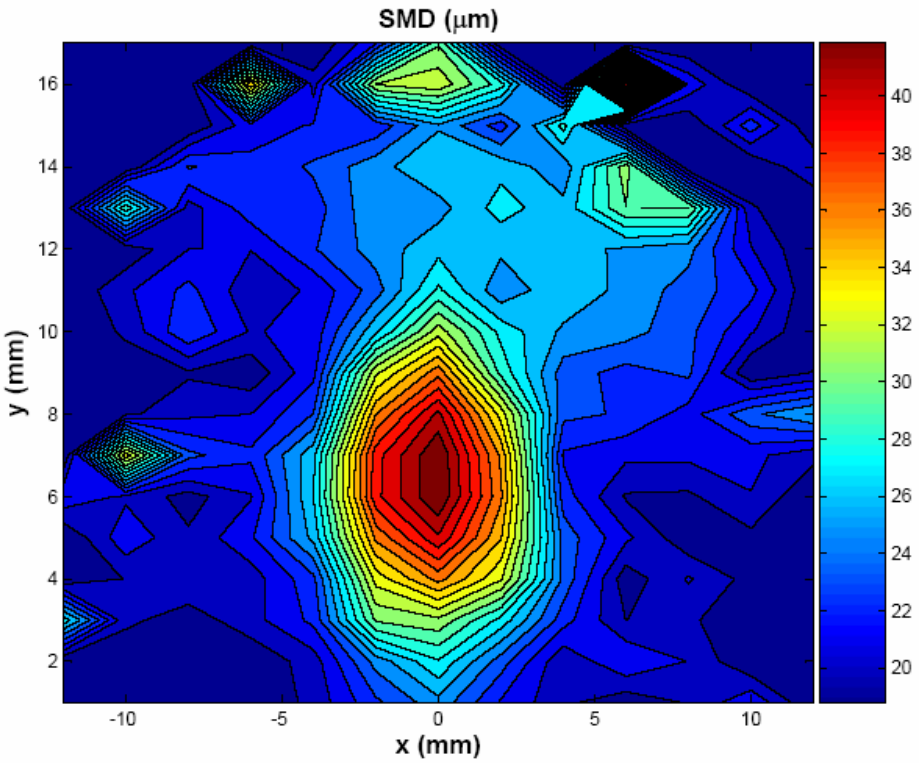

Fig. 5.6 SMD for N-Heptane We = 1150.6, q = 4.8, D = 0.762 mm, z = 23 mm

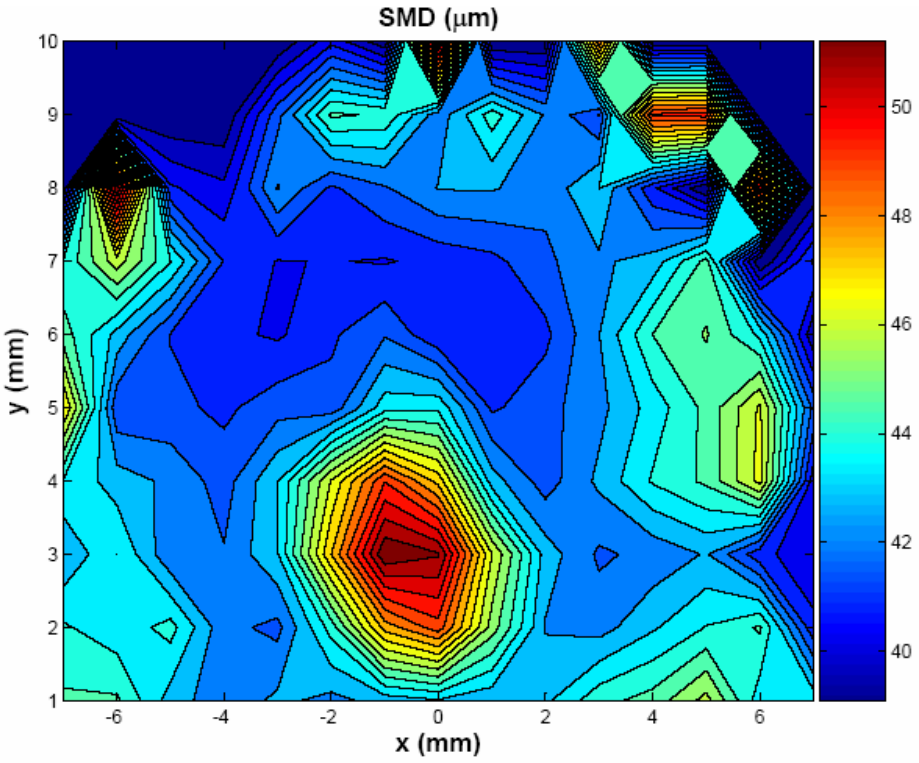

Fig. 5.7 SMD for Water We = 96.2, q = 5.2, D = 0.381 mm, z = 11.5 mm

the crossflow dynamic pressure improves the atomization, from which we conclude that in general the droplets produced by a water jet are slightly larger than those produced by a Jet-A jet under similar conditions.

Thus N-Heptane produces smaller droplets than Jet-A while water produces larger droplets. The surface tension of the three liquids also follows a similar trend with N-Heptane having the lowest σ (21.4 N/m) while water has the largest σ (72 N/m). Hence we conclude that a decrease in the surface tension improves the atomization by allowing smaller droplets to be produced. We notice that the same observation was made in section 4.7 from the shadowgraphs for the three liquids.

Chapter 6: Results and Discussion - Center-Plane Spray Distributions

In Chapter 5 we compared the spray distributions in a cross-sectional plane of the jet injected into a crossflow. We also studied the variations in this distribution due changes in different parameters. In this chapter we will study the effects of these parameters on the centerline spray distributions.

6.1 Effect of Streamwise Distance on Center-Plane Spray Distributions

The variations of the spray SMD in the center-plane for cases J_100_5 and J_100_10 at streamwise distances of 12, 20 and 28 mm are shown in Fig. 6.1 a, b, respectively. We have observed in Chapter 5 that the spray SMD exhibits a maximum in the spray core for low values of q and towards the periphery for high values of q. Thus Fig. 6.1 a. (q = 5) has a peak of the SMD in the spray core while Fig. 6.1. b (q = 10) has a SMD peak near the upper extremity of the spray. As the transverse distance increases, the SMD values for the low q case increase; reach a maximum; decrease and then increase again near the periphery. The SMD profile for the high q case increases monotonously with increase of transverse distance[16,29].

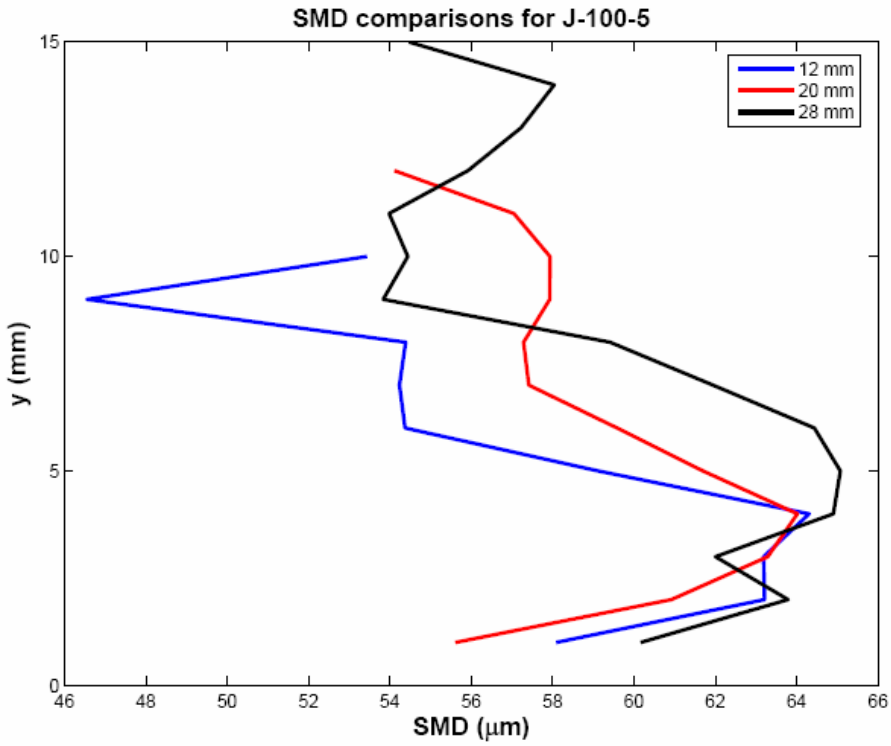

Fig. 6.1 a. Effect of Streamwise distance on SMD for Jet-A We = 94.8, q = 5.2, D = 0.381 mm

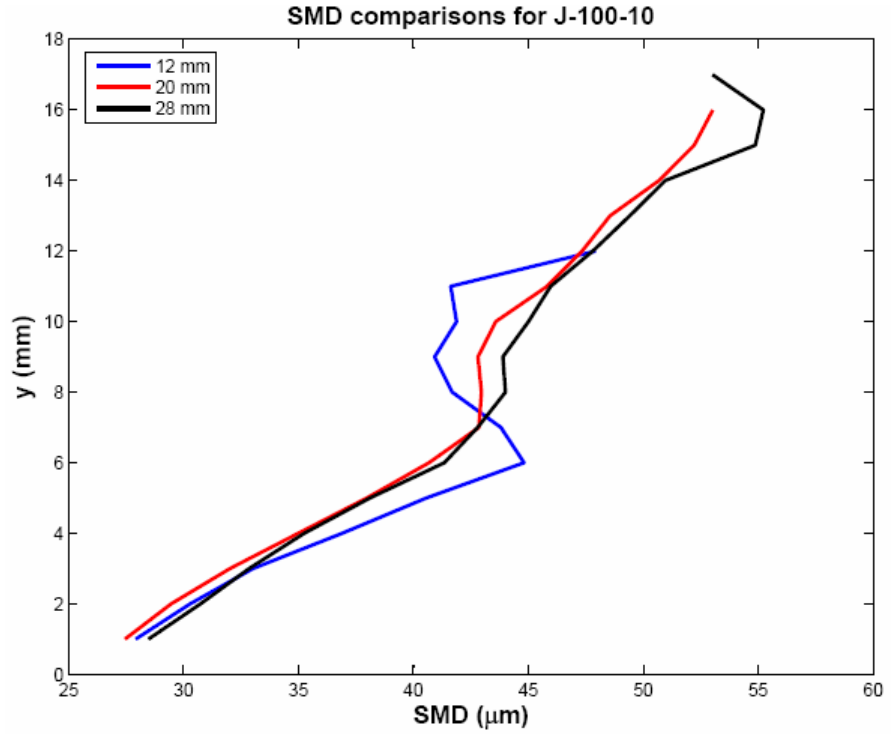

Fig. 6.1 b. Effect of Streamwise distance on SMD for Jet-A We = 94.8, q = 10.1, D = 0.381 mm

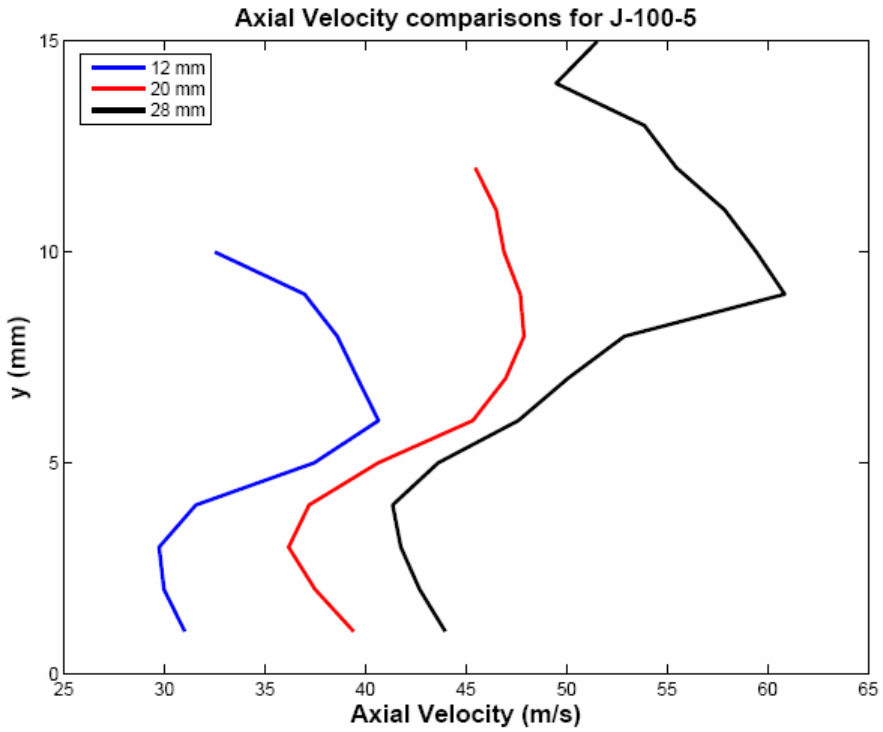

Fig. 6.2 a. Effect of Streamwise distance on Ud for Jet-A We = 94.8, q = 5.2, D = 0.381 mm

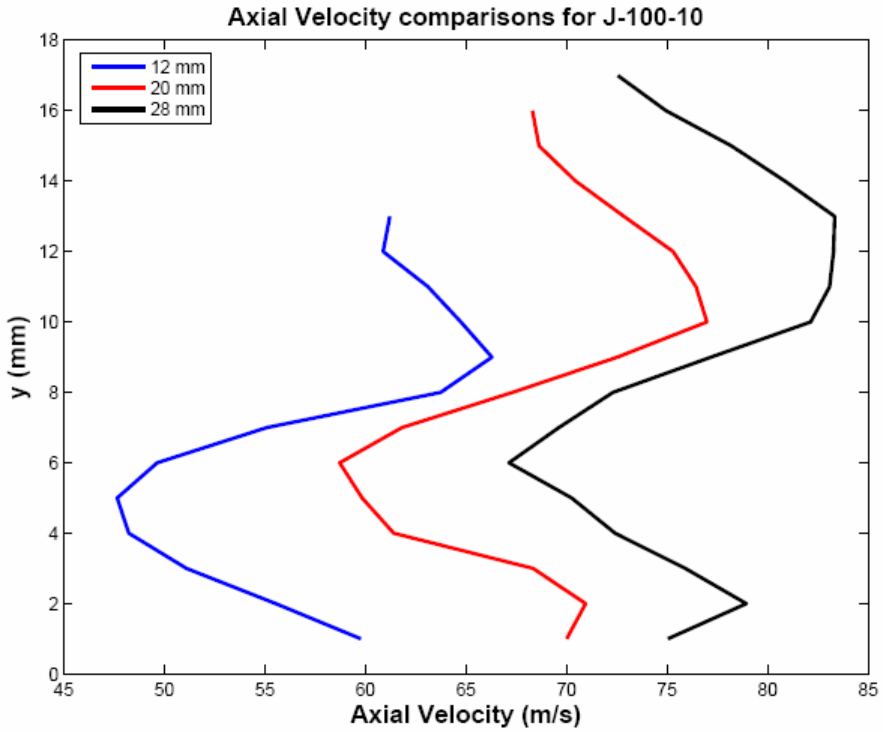

Fig. 6.2 b. Effect of Streamwise distance on U_d for Jet-A We = 94.8, q = 10.1, D = 0.381 mm

As we move further downstream we observe that the spray penetration increases for both cases. The SMD values at transverse locations close to the wall are almost equal. However, as we go further from the wall, the SMD values are seen to increase with downstream distance.

The variations of the droplet axial velocities for the same cases are seen in Figs 6.2 a, b. As we move away from the bottom wall the velocity profile exhibits the following characteristic. It reduces initially to a minimum near the spray core region, increases, exhibits a maximum just below the spray extremity and then decreases again[16,37]. All the cases exhibited a similar trend in the velocity profile. We note here that the top of the plume basically consists of large droplets moving relatively slowly[16].

With increasing downstream distance, the shape of the velocity profile does not change much, however its magnitude increases causing the profile to shift towards increasing U_d[16] and y. The increase in y is simply due to an increase in the spray penetration with streamwise distance. The increase in the magnitude of the axial velocity is due to the higher momentum exchange of the jet. The jet entrains a part of the crossflow fluid into itself, as a result of which its overall momentum increases due to the higher momentum crossflow particles. The amount of crossflow fluid increases with streamwise distance, causing an increase in the axial velocity of the spray.

6.2 Effect of q on Center-Plane Spray Distributions

The effect of q on the center-plane SMD distributions is shown in Fig. 6.3 a, b for conditions of We = 94.8 (J_100_5, J_100_10) and 1148.6 (J_1200_5, J_1200_10). The chief effect of increasing the momentum ratio is an increase in the penetration. Also we observe some decrease in the SMD values with an increase in the q. The drop in SMD seems to be significant for the low We case (low U_∞), however the high We (high U_∞) case exhibits only a minor drop in the SMD. Since we already know that the dynamic pressure of the crossflow plays an important role in the breakup process we conclude that an increase in q also improves the breakup, but only to a small extent. The significant increase found at We = 94.8 is primarily because the crossflow velocity is very low, hence its contribution towards atomization is also comparably less.

Fig. 6.4 a, b show the effect of q on the axial velocity distribution in the center-plane. As q increases the axial velocity of the spray droplets is also seen to increase, while the shape of the profile remains the same. The transverse location of the minimum in the axial velocity moves upwards[16] with an increase in q. The higher penetration of the spray allows for more entrainment of the crossflow fluid. Also the injection velocity of the droplets is high due to the high q. As a result of these, the droplets have higher axial velocity in case of conditions of high q. For the low We case, a larger increase in the droplet axial velocity is observed due to the smaller value of the U_l. This increase seems to be marginal for the We 1200 case; however we note that for this case the droplets are already moving at very high speeds, hence the relative increase in velocity is only marginal.

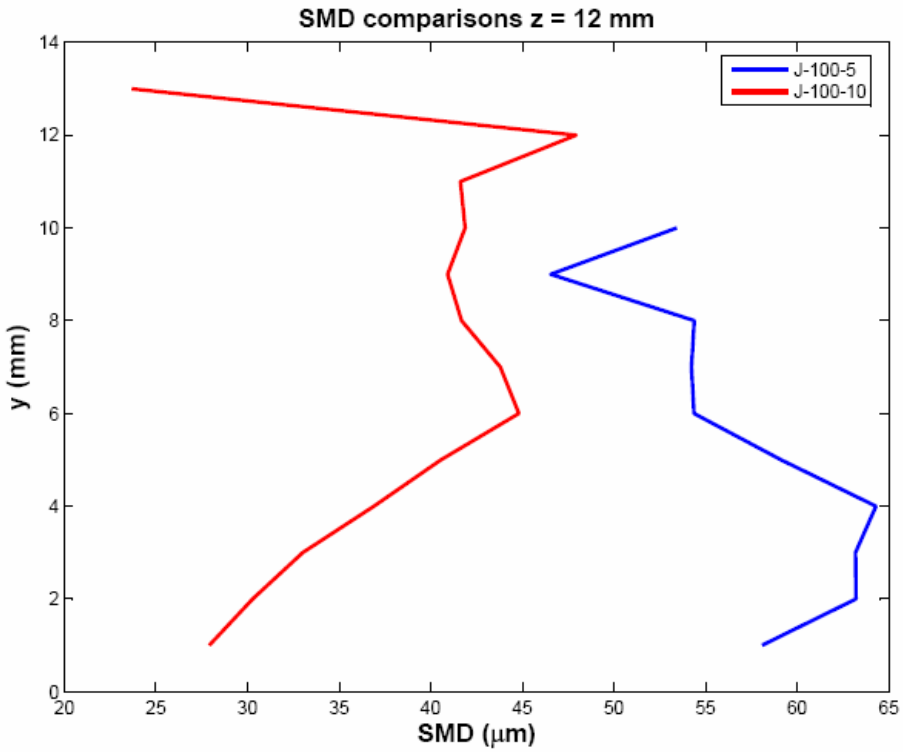

Fig. 6.3 a. Effect of q on SMD for Jet-A We = 94.8, D = 0.381 mm

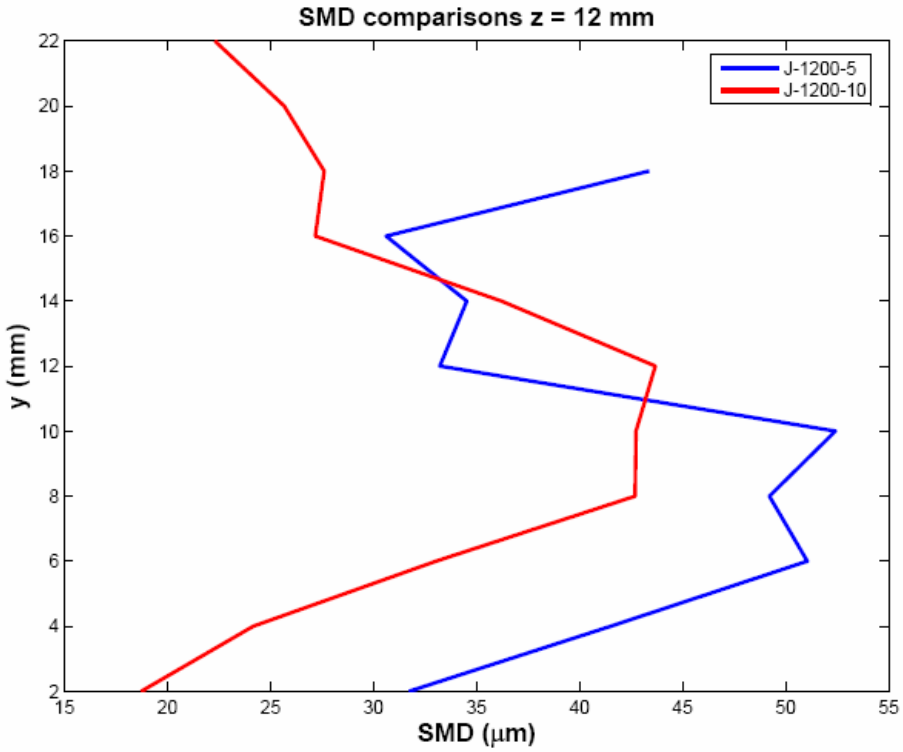

Fig. 6.3 b. Effect of q on SMD for Jet-A We = 1148.6, D = 0.762 mm

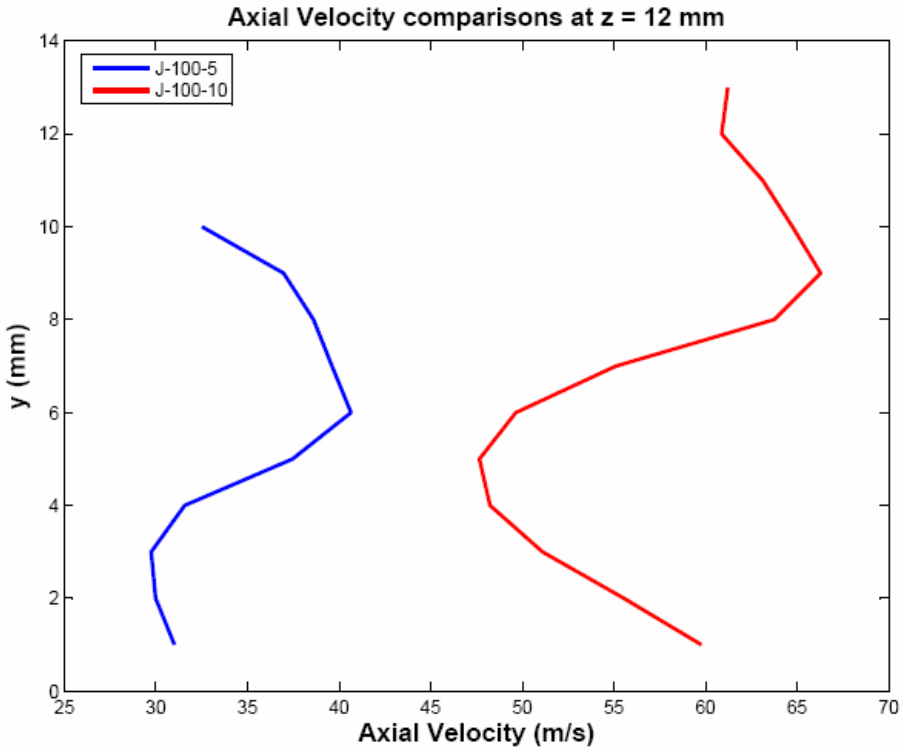

Fig. 6.4 a. Effect of q on Axial Velocity for Jet-A We = 94.8, D = 0.381 mm

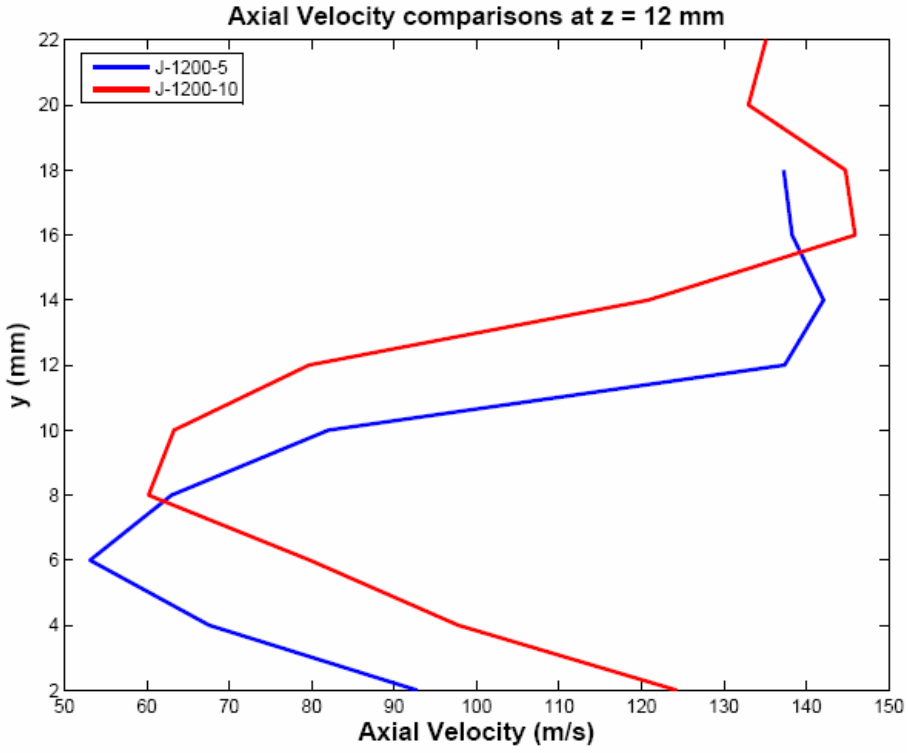

Fig. 6.4 b. Effect of q on Axial velocity for Jet-A We = 1148.6, D = 0.762 mm

6.3 Effect of U_∞ on Center-Plane Spray Distributions

The effect of an increase in We by and increase in U_∞ on the SMD and velocity distributions in the center-plane of the spray is shown in Figs. 6.5 a, b respectively, where the profiles for J_100_5 (Jet-A, D = 0.381 mm, We = 94.8, q = 5.2) and J_500_5 (Jet-A, D = 0.381 mm, We = 471.6, q = 5.1) are compared. A sharp decrease in the spray SMD is observed with an increase in We[14,16,19,40]. We observe that the reduction in SMD due to an increase in the We is much greater than the reduction due to an increase in q. We had already seen in Chapter 6 that the dynamic pressure of the crossflow is chiefly responsible for the extent of atomization of the spray. Since the increase in crossflow is the chief method of increasing the We from 94.8 to 471.7, the decrease in SMD is essentially due to the same. We also observe some reduction in the range of SMDs observed, which shows that an increase in We produces a more uniform mixture of the spray with the crossflow.

An increase in We causes the center-plane axial velocity profile to sharply increase in magnitude primarily because of the higher crossflow velocities. Momentum exchange improves significantly which is reflected in the much higher velocity difference between the droplet velocities in the spray core and in the spray periphery.

6.4 Effect of D on Center-Plane Spray Distributions

Fig. 6.6 a, b show the effect of a change in the injection diameter, D on the SMD and axial velocity distributions. The distributions are compared for J_500_5 (Jet-A, D = 0.381 mm, We = 471.7, q = 5.1) and J_1200_5 (Jet-A D = 0.381 mm, We = 1148.6, q = 5)

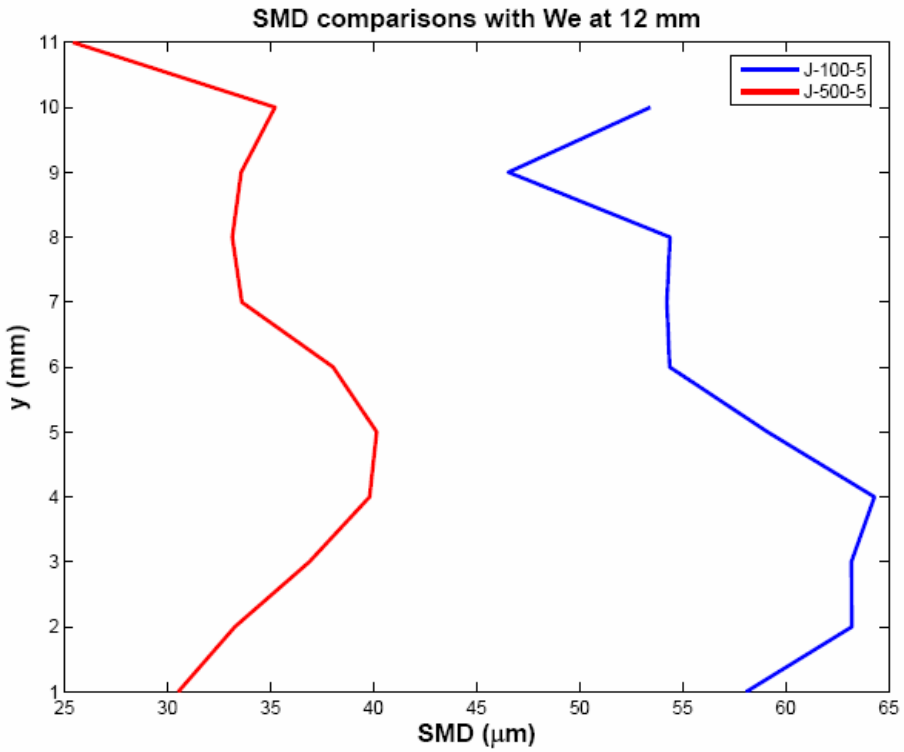

Fig. 6.5 a. Effect of U_∞ on SMD for Jet-A We = 94.8, 471.6, q = 5

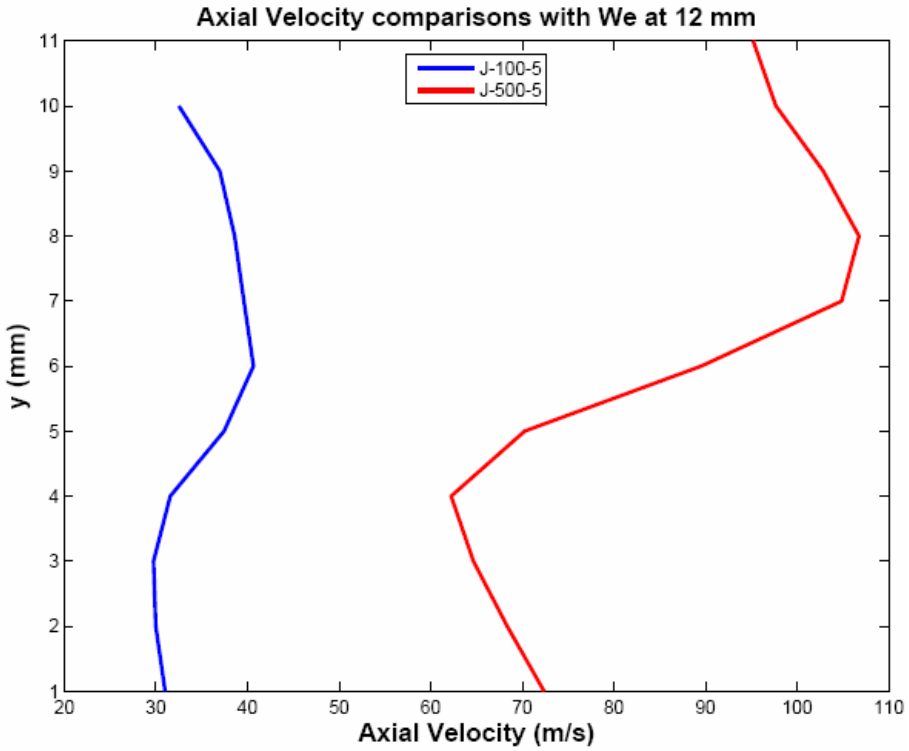

Fig. 6.5 b. Effect of U_∞ on Axial Velocity for Jet-A We = 94.8, 471.6, q = 5

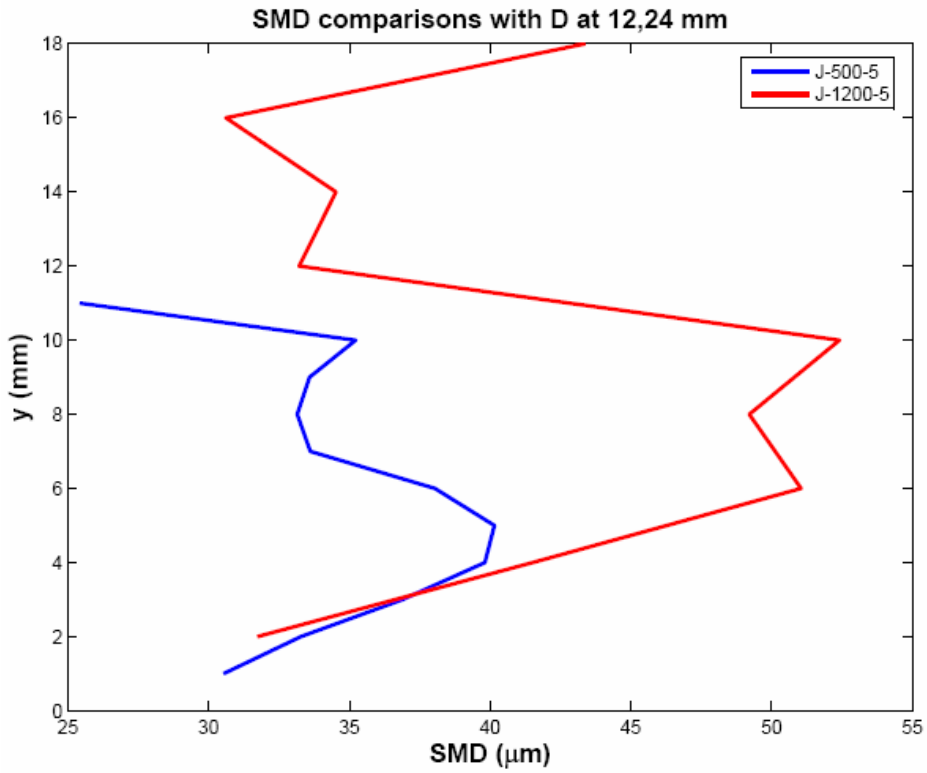

Fig. 6.6 a. Effect of D on SMD for We = 471.6, 1148.6, q = 5, D = 0.381 mm (We = 471.6), 0.762 mm (We = 1148.6)

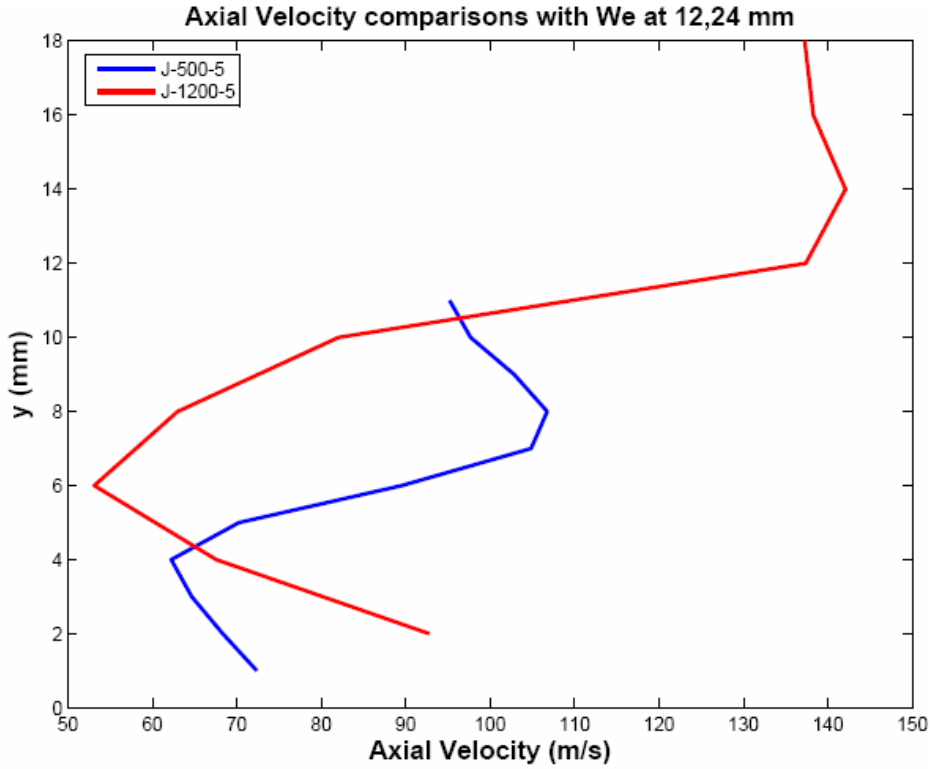

Fig. 6.6 b. Effect of D on Axial Velocity for We = 471.6, 1148.6, q = 5, D = 0.381 mm

We observe that an increase in D increases the penetration significantly[14]. Also the larger diameter jet seems to have larger SMDs as compared to the 0.381 mm jet. This shows that an increase in the jet diameter does not produce any improvement in the SMD even though the crossflow velocities are approximately equal.

The axial velocity distributions are similar with the 0.762 mm jet having much larger axial velocities. This is chiefly due to the higher momentum exchange due to the higher penetration.

6.5 Summary of Spray Distributions

We have found that for low values of q, SMD exhibits a maximum in the spray core region. This maximum moves towards the spray periphery with an increase in the jet penetration. Droplet velocities are usually low in the spray core and increase towards the periphery. Volume flux peaks in the spray core and decreases gradually on all sides.

We have also observed a very interesting phenomenon. An increase in the crossflow dynamic pressure (or U_∞) improves the atomization but does not affect penetration. On the other hand both q and D affect the jet penetration, but have little or no effect of the atomization. A similar conclusion was made by Becker and Hassa[2]. The significance of this observation is that both the atomization and the penetration can be optimized independent of each other.

Chapter 7: Results and Discussion - Breakup and Penetration Behavior

We have so far observed the behavior of the jet column and the post-breakup spray and the variation in their behavior with changes in We and q. In this chapter we focus our attention on the phenomena associated with the jet breakup. The latter part of the chapter will deal with the penetration of the jet column.

7.1 Breakup Modes

Two distinct breakup modes have been observed in the course of this study. These modes are called column breakup and surface breakup. Wu et al[36] and Becker and Hassa[2] also observed the same breakup modes for their experiments. Of these, Wu et al[36] conducted experiments at atmospheric pressure, but the air velocities were lower than the current study, and Becker and Hassa[2] conducted their experiments at elevated pressures.

While studying the behavior of the jet column, we observed two different mechanisms for the formation of droplets from the jet. The first mechanism is the breakup of the jet into ligaments. Surface waves occur on the jet, which might be produced by the jet vorticity, and cause the jet column to rupture at some of the wave trough locations. This produces short segments of the jet liquid, called ligaments. These ligaments are acted upon by the dynamic

pressure of the air and break up to form droplets with diameters of the order of the jet diameters. These droplets undergo further breakup to produce smaller droplets[36].

The second mechanism is the droplet shearing from the jet column surface. The pressure distribution on the jet column causes the jet to flatten from a circular shape to an oblate shape. Moreover surface waves exist on the side and leeward surfaces having extremely small wavelengths. Due to this, the shear forces on the sides of the jet column, in combination with the leeward surface waves, lead to the stripping-off of small droplets from the walls of the jet. The diameters of these droplets are much smaller than the jet diameter. The droplet shearing mechanism causes a gradual erosion of the jet column, which might cause a change in its behavior due to the corresponding momentum loss of the jet column[2]. Both of these mechanisms can be observed in the schematic jet shown in Fig 4.1 and also in the baseline case shown in Fig. 4.2.

Both of the breakup mechanisms described above are usually active for a jet; however for most of the cases only one of them is dominant[2]. This leads us to label the breakup modes, based upon the dominant breakup mechanism. The column breakup mode is said to occur when the mechanism of formation of ligaments is the prominent form of breakup, and little or no droplet shearing-off is present[2,36]. This mode was exhibited by cases having low We and low q values. Moreover this mode was observed only for cases involving the smaller injection diameter, 0.381 mm. A sample shadowgraph of a jet undergoing column breakup is shown in Fig. 7.1 a.

Surface breakup mode is said to occur when the shearing-off mechanism is the dominant process of breakup[2]. A sample shadowgraph of a jet undergoing surface breakup is shown in Fig. 7.1 c. The process of ligament formation still exists, but its contribution to droplet formation is much lesser than the shearing-off process. Jets with high q values, where a well-defined column exists, due to the higher penetration, are seen to exhibit surface breakup. For the same value of q, surface breakup occurs when the crossflow dynamic pressure increases beyond a certain value, i. e. for higher crossflow velocities[2]. The larger diameter jets (D = 0.762 mm) had significantly larger penetrations, which implies a longer jet column, hence the shearing mechanism was active for all cases, placing them in the surface breakup mode. The droplets sheared off from the jet form a dense cloud in the downstream portion of the spray plume[4]. In many of the high We cases, including all of the larger diameter jets, the cloud of droplets stripped off was so dense that no trace of ligament formation could be observed from the shadowgraphs.

However, since both mechanisms have been observed to occur at the same time, as we increase either q or We, we come across a region where there is no marked dominance of either of the breakup mechanisms. Such a case is shown in Fig. 7.1 b. In other words, these modes are not exclusive and some overlapping occurs between the modes. This region has been called as the mixed breakup mode.

We have observed that the breakup mode shifts from column breakup to surface breakup as we increase in either We or q. An increase in We implies an increase in the dynamic pressure exerted by the crossflow on the jet. Since we have observed that the crossflow dynamic pressure is responsible for the shearing mechanism, it is natural for the same mechanism to

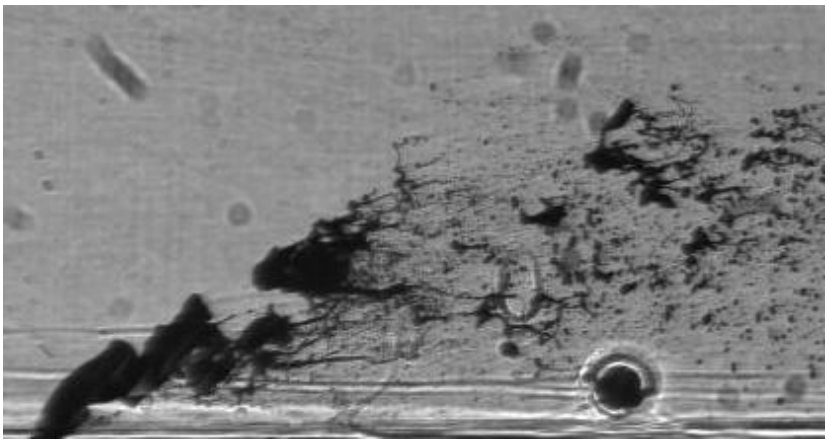

Fig. 7.1 a. Column breakup mode

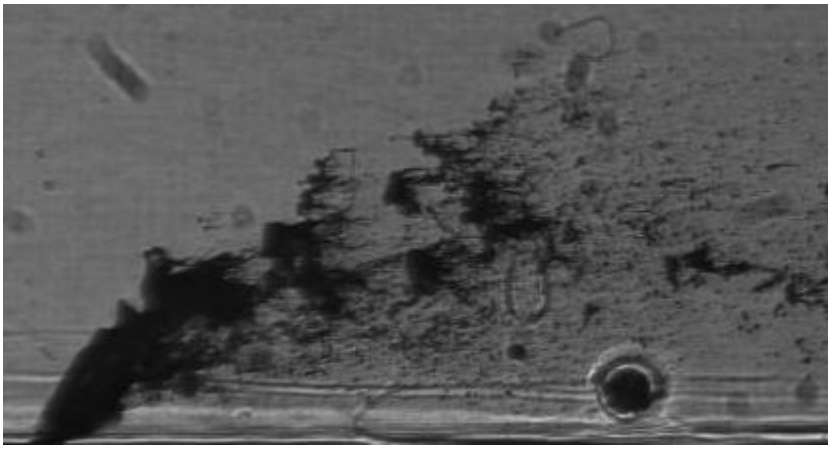

Fig. 7.1 b. Mixed breakup mode

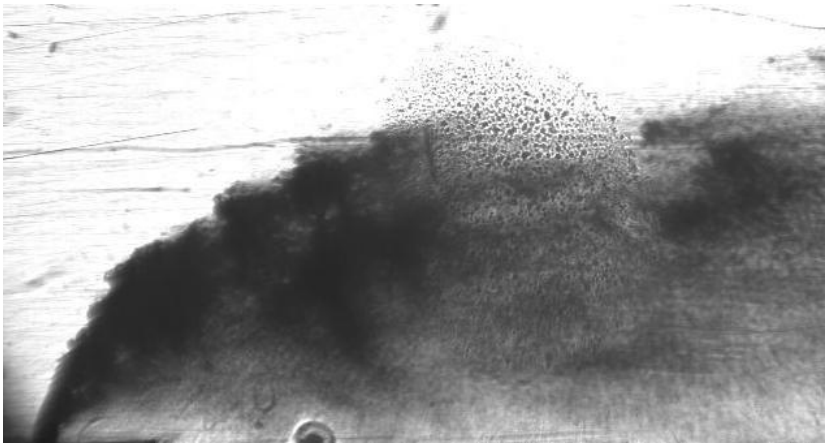

Fig. 7.1 c. Surface breakup mode

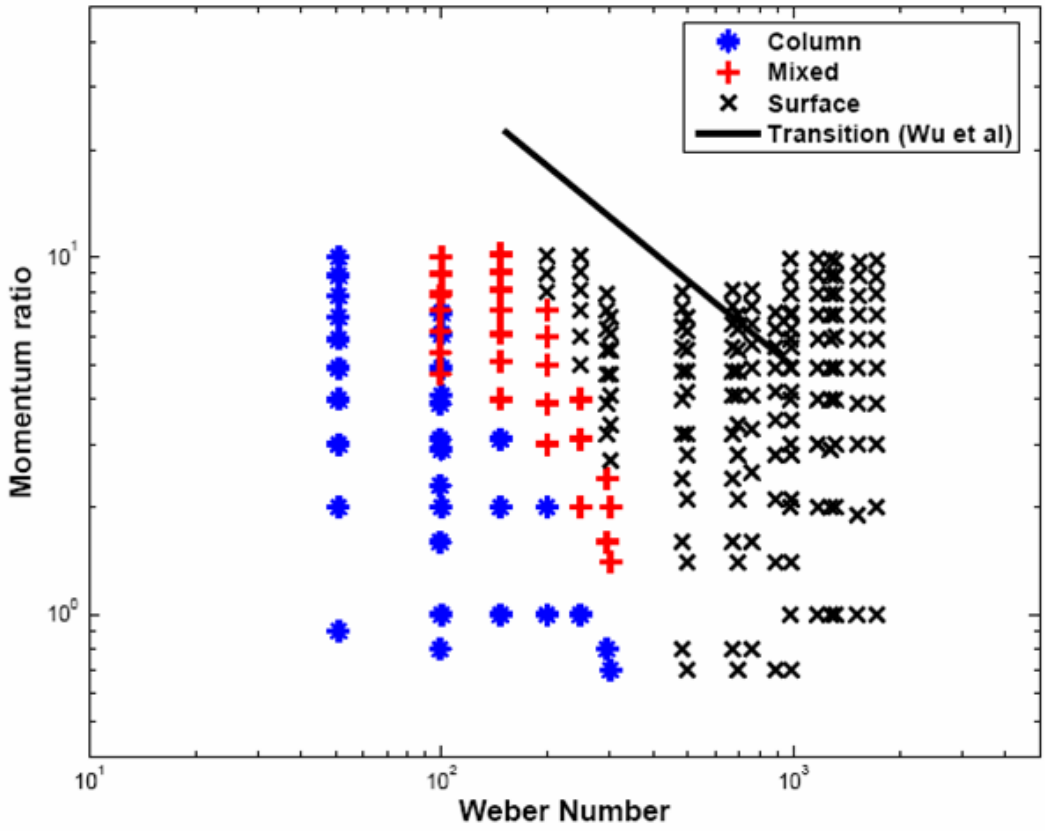

Fig. 7.2 Breakup Modes in We-q plane with the transition line from Wu et al[36]

strengthen, thus causing the transition from column to surface breakup mode. The effects of an increase in q arise due to the increased penetration of the jet at higher q. Due to the increased penetration, a longer column length is available for the shearing-off process, thus increasing the proportion of the droplets generated by this process.

The transition of the breakup mode by a change in We and q can be easily observed from a plot of the breakup mode in a We-q plane shown in Fig. 7.2. A similar plot had been created by Wu et al[36]. The scale of Fig. 7.2 has been chosen so as to correspond with Wu et al's[36] plot, in order to facilitate easy comparison of the results. Wu et al[36] had plotted a line of transition between the breakup modes, which has been replicated in Fig. 7.2.

The transition between the breakup modes for the current results follows a similar trend as the line plotted by Wu et al[36]. However, it is seen to occur at lower values of q and We. Also it exhibits a higher slope, indicating that transition occurs at increasingly lower values of We as compared to that of Wu et al[36] with a decrease in the transition q value. A reason for this is the higher freestream velocities employed in the current experiments, leading to high dynamic pressures. These higher dynamic pressures strengthen the shearing-off mechanism causing the transition to surface breakup to occur earlier. Thus, the effect of increasing q is similar to that of Wu et al[36] but the effects of increase in We are more severe, causing the increase in slope of the transition line.

7.2 Breakup Locations

The location of the jet breakup is significant as it signifies the initiation of the spray zone, which consists mostly of droplets. For the current results the breakup location has been defined as the mean jet location at the point of ligament formation as shown in Fig. 7.3.

However, for the current experiments, a large portion of the test cases, 83%, have been observed to exhibit the surface breakup mode. In most of these cases, the presence of a dense droplet cloud below and on the sides of the jet completely blocks the view of the

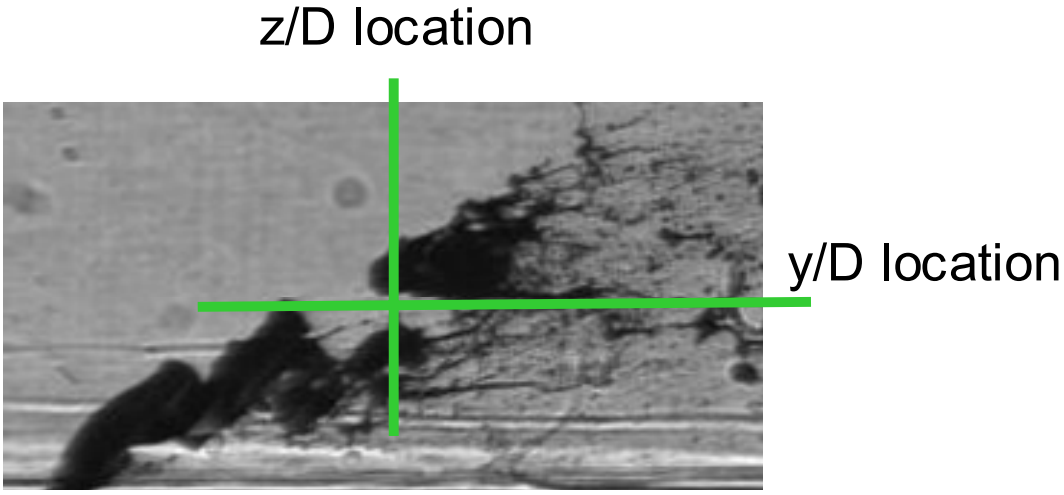

Fig. 7.3 Streamwise and transverse breakup locations

jet column. Due to these, breakup locations could only be determined for the cases with column and mixed modes of breakup.

The streamwise (z/D) and the transverse (y/D) coordinates of the breakup locations have been plotted in Figs. 7.4 and 7.5 respectively with q as the abscissa. The plot of the z/D locations with q is a scattered plot with a mean value of 13.7 and a standard deviation of 2.56 with the z/D varying from 5.4 – 17.4. Many studies in the literature have found streamwise (z/D) location of the breakup of length to be constant regardless of variation of all parameters. However, there exists some difference for the value reported for the streamwise breakup location.

The high standard deviation in the plot for the current experiments suggests an erratic nature for the breakup locations and hence does not seem to be in harmony with the above conclusion. However a closer look at the plot shows that the z/D locations for $q \leq 2$ are much smaller than the rest of the points and are responsible for the high standard deviation.

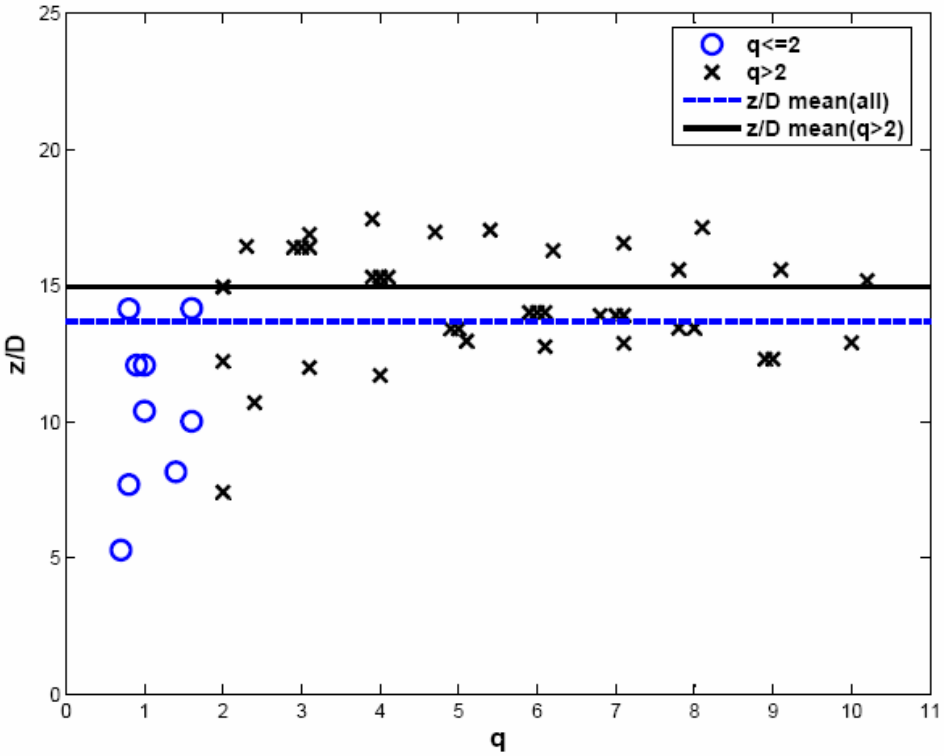

Fig. 7.4 Breakup z/D Locations

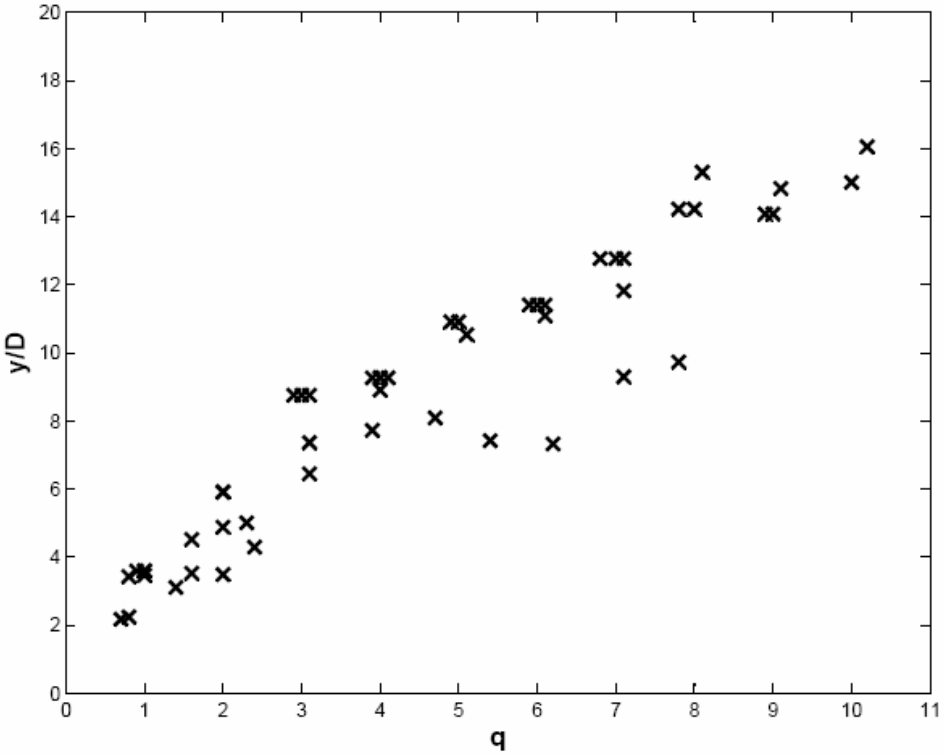

Fig. 7.5 Breakup y/D Locations

Eliminating these results, we observe a mean z/D location of 14.97 with a standard deviation of 1.37. Also the range for the z/D locations decreases to 10.7-17.4 for the cases with $q > 2$. Then for $q > 2$, we can claim the streamwise location to be constant within experimental error, noting that for a 0.381 mm diameter, the difference between the maximum and minimum values of the range of z/D is just 2.5 mm. The low values of the streamwise breakup locations could be due to the presence of the boundary layer near the walls of the jet. In Fig. 5.2 the z/D locations for $q \leq 2$ have been represented by blue circles and the mean locations for the complete dataset is represented by a blue dashed line. We see that the mean for the z/D locations for $q > 2$ (black line in Fig. 5.2) provides a better description of the data.

The transverse (y/D) breakup locations are observed to increase with q. Similar observations have been reported in the literature and the transverse location has been correlated with q. However, no efforts were taken to obtain a correlation for the current results due to the extremely limited number of cases for which breakup locations could be determined.

7.3 Jet Penetrations

For any application of liquid jets in crossflows including LPP premix ducts, two of the most significant characteristics of the flow are the location of the spray and the extent of atomization and mixing with the crossflow air. The first of these can be quantified by measuring the jet penetrations and correlating it with the streamwise distance. However, the definition of jet penetration is not exclusive. Some of the representations for jet penetration in earlier studies have been the outermost (or uppermost) extremities of the jet[5,14], mean

streamline location[39], locations of maximum velocities[39], and the location of maximum liquid concentrations[11,33]. The application of interest for the current study is the premix duct of LPP combustors; consequently we need to design the flow so as to prevent any excessive impingement on the farther wall of the duct. Hence the transverse extremity of the jet at any streamwise location is taken to be the penetration of the jet at that location. The penetration then serves as a reference of the position of the jet within the flowfield.

The origin of the coordinate system was shifted 0.5D upstream, which is the upstream end of the injection nozzle, for the sake of the penetration calculations, to ensure that the correlation passes through the origin.

The shadowgraphs for each test condition were averaged using the Image Processing toolbox in MATLAB. The averaged shadowgraphs were used to determine the jet penetration values. A digitizing software, DigitizeIt! was used to manually pick out points lying on the jet extremity. The streamwise range for studying the penetrations of the jet was restricted to streamwise values of $z/D = 0\text{-}30$.

The penetration behavior of the intact jet can in general be expected to be different from that of the droplets. This conclusion was also reached by Chen et al[6] who proposed a three-term correlation for the jet penetration to account for the three zones of the jet, namely column, ligament and droplet regions. The penetrations of the unbroken column can be taken to be a reasonable estimate of the penetration characteristics in the near field region. However, the unavailability of breakup locations for large portions of the data precludes this choice of the range for the study of the penetrations. Due to this, the above mentioned

streamwise range was chosen, which was primarily based on the range of the shadowgraphs. The points picked from DigitizeIt! were restricted to this range. Approximately 30 points were chosen for every test condition.

Nonlinear regression analysis was carried out on the data points to obtain a correlation using the software NLREG. The software NLREG uses the data to optimize the shape of a user-input curve function to best fit the dataset. The user needs to feed a form of the final correlation in the form of a functional model, and NLREG computes the parameters for the model variables and the errors associated with the final result.

A brief survey of the correlations established in the literature was necessary to use an optimal model to describe the jet penetrations. All correlations in the literature correlate the penetration (transverse location) to the streamwise location, z, injection diameter, D, and q[2,6,17,36,38]. The penetration has been reported to be independent of all other parameters[2,36]. Three different functional forms have been observed in the published literature. These are a power-law description[36], a logarithmic relation[2,17,38] and an exponential form[6]. Hence for the sake of completeness, a model was selected for each of these three forms and the results were compared to select a model that best described the dataset.

The three models used with NLREG were as follows:

$$\frac{y}{D} = cq^{p}\left(\frac{z}{D}\right)^{r} \tag{7.1}$$

$$\frac{y}{D} = cq^{p}\ln\left(1 + d\frac{z}{D}\right) \tag{7.2}$$

$$\frac{y}{D} = cq^{p}\left[1 - d\exp\left(\frac{-z/D}{e}\right)\right] \tag{7.3}$$

NLREG then computes the values of c, d, e, p and r. The correlations obtained from the use of these three models have been shown in Fig. 7.6. The exponential model seen in equation 7.3 provided the least errors with a standard deviation of 1.822. However, the correlation obtained from this equation is flawed because it does not pass through the origin. Chen et al[6] who proposed an exponential correlation had a relation involving three exponential terms. The correlation was limited numerically by scaling the transverse coordinates by the maximum penetration, so that y/D values had limits imposed on them. For the current experiments, the restriction to near field studies meant that maximum penetration was not reached. Hence a scaling could not be used, without which adding more exponential terms to the correlation caused it to diverge. Hence the correlation using the exponential model was discarded.

The next best result was obtained by the Logarithmic model of Equation 7.2. The standard deviation for this correlation was 1.826. The resulting correlation is given in equation 7.4.

$$\frac{y}{D} = 1.55q^{0.53}\ln\left(1 + 1.66\frac{z}{D}\right) \tag{7.4}$$

The correlation has been plotted along with the data points in Fig. 7.7. In order to enable us to plot all the data in a single graph the data have been made independent of q by scaling the

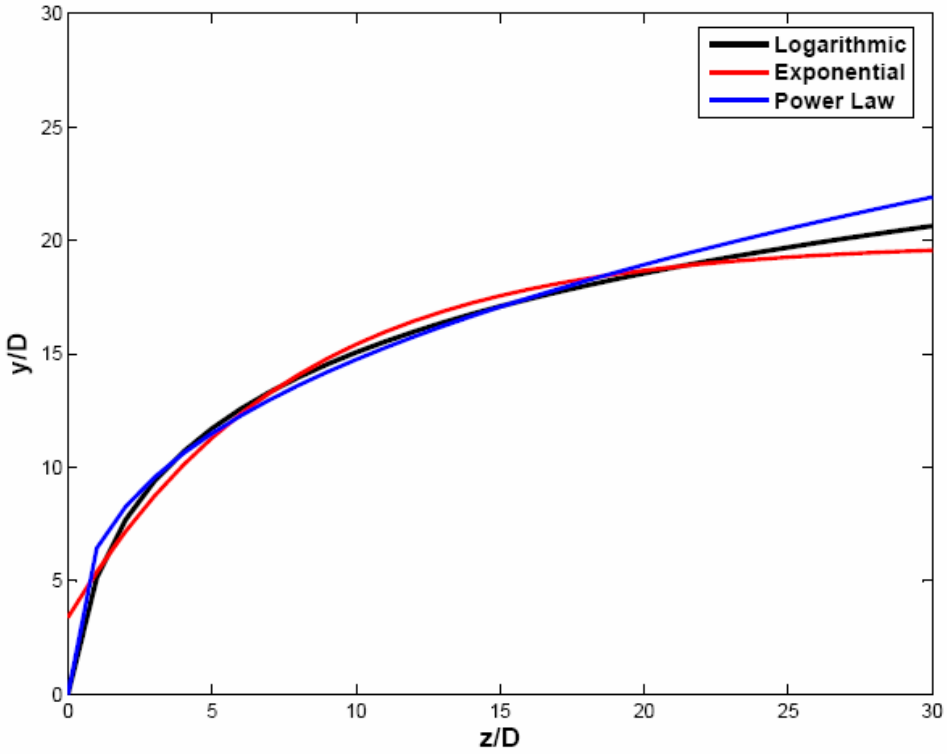

Fig. 7.6 Comparison of Computed Correlations

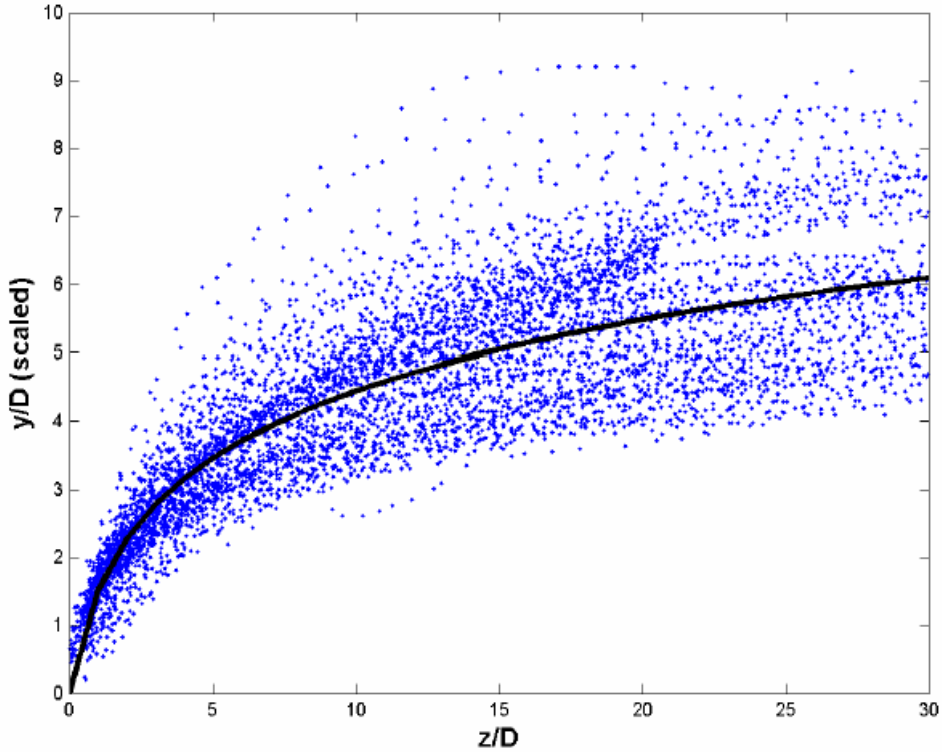

Fig. 7.7 Final Correlation with Scaled Data

y/D coordinates by $q^{0.53}$. Thus the plot of Fig. 7.7 is actually z/D vs. scaled y/D, where scaled y/D is simply $(y/D)/q^{0.53}$.

We observe that the correlation does seem to capture a mean of the dataset. However, there still seems to be a lot of spread on either side of the correlations. The author reasoned that this large variation might be the effect of some other parameter of the penetration which might have had a non-negligible effect on the penetration over the range covered. Since the experiments do cover a large range of test conditions, it is entirely possible that the effect of some parameter, though it is negligible over a smaller range, might reach significant proportions when considered over the entire range. Other parameters which might have had and effect of the jet penetrations are We, Re_∞, Re_j and Oh.

NLREG computations were then carried out for variations of equation 7.3 with the added influence of different combinations of the additional parameters. Since the aim was to investigate an improvement in the errors by putting an additional influence, the q dependence was frozen before adding any influencing parameters. This was to prevent NLREG from locking on to a mathematical optimum point, which might not have any physical relevance. However no combination of the additional parameters was found to provide any significant improvement in the fit of the correlation to the data. It was thus concluded that the jet penetration is independent of these additional parameters. Thus we have indirectly supported the conclusions of other studies which have found the jet penetrations to depend only on q and the downstream distance. Thus for a given downstream location, the penetration depends only on q. This conclusion holds a special significance as we will observe later on.

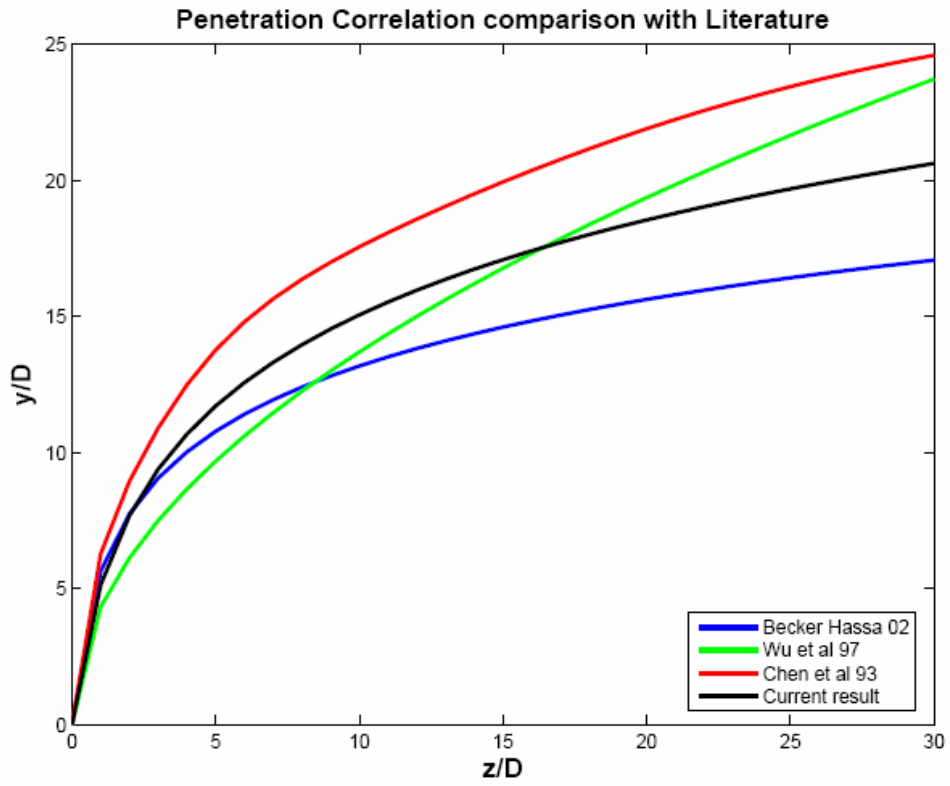

Fig. 7.8 Comparison of Computed Correlation with Correlations from Literature

It is pertinent to point out here that in Chapters 4-6, and even in the penetration computations, the penetration is seen to increase with the injection diameter, D. However, an increase in D also increases the Weber number, We, all other parameters being constant. Then, one can expect We to have some influence on the penetration, however no such influence is evident from the penetration data. The reason for this could not be explained.

Finally the correlation predicted from this study was compared to some of the penetration correlations present in the literature. A plot of the correlations has been shown in Fig. 7.8 for a q value of 10. We observe that the exponential and the power law correlations, of Wu et al[36] and Chen et al[6] respectively, have significantly higher penetrations as compared to the logarithmic correlations, the computed correlation and the one of Becker and Hassa[2].

Both the studies of Wu et al[36] and Chen et al[6] were conducted at atmospheric pressures for relatively low subsonic crossflows. The current study has relative high speed subsonic crossflows, and Becker and Hassa[2] carried out studies at elevated pressures (high density). Hence both of these studies had significantly higher crossflow dynamic pressure, with that of Becker and Hassa[2] being much greater than for the current study. Correspondingly these two studies have lower penetrations, with the penetrations for Becker and Hassa[2] being even lower than that of the current study, as should have been expected.

Chapter 8: Conclusions and Future Work

8.1 Conclusions

A systematic experimental study of liquid jets injected into subsonic crossflows has been carried out. The experiments were carried out at atmospheric pressure. The test range was expanded by using three injection liquids and two nozzle sizes. The Weber number range was sought to be maximized while limiting the momentum ratio to regions of applicability to premix ducts of LPP combustors. Pulsed shadowgraphy and PDPA techniques were used to study the jet column behavior, its penetration and breakup characteristics, and the behavior of the spray produced after breakup. The findings are summarized as follows:

1. The jet bends soon after injection and aligns itself with the crossflow direction. The bending occurs due to the drag exerted on the jet by the crossflow.

2. Surface waves are observed on the jet column shortly after injection. The appearance of surface waves is very close to the location where significant bending starts. These waves seem to be responsible for the jet breakup. These waves are formed due to the vorticity present in the jet.

3. Two mechanisms have been found for the formation of droplets from the jet. The jet column breaks up into ligaments which undergo further breakup to form droplets. The other

mechanism arises from the shearing-off of liquid droplets from the surface jet column due to the dynamic pressure exerted by the crossflow

4. These two mechanisms govern the existence of the two breakup modes, column and surface breakup. Column breakup occurs at low q and low We. Increase in either q or We leads to a change of breakup mode to surface breakup. A finite region is observed between these two modes where both mechanisms are active and is called as the mixed breakup mode.

5. The breakup of the jet is observed occur at a constant streamwise location within limits of experimental error. Inclusion of low q values, which might have been affected by the wall boundary layer, adds to the error. The transverse breakup locations increase with q.

6. Jet penetration depends upon the momentum ratio, q, the streamwise distance, z and the injection diameter D. A correlation has been found to relate the penetration with these parameters.

7. For low q, SMD peaks in the spray core and decreases on either side. However, further away from the wall, SMD starts increasing again towards the periphery. Higher q values exhibit a monotonous increase in q towards the periphery. Decrease in surface tension is found to produce smaller droplets.

8. Liquid velocities exhibit minima in the spray core, which has been attributed to the wake behind the jet. Regions of high velocity are found on the lateral sides of the jet.

9. Volume fluxes peak in the spray core. A large portion of the liquid is found to be concentrated within a small portion of the spray cross section

10. Spray penetration depends on q and D while atomization depends on u_∞. This is very significant as it allows either of them to be optimized independent of the other.

8.2 **Scope for Future Work**

The current study for liquid jets has been limited to atmospheric pressures and temperatures. The next step towards a complete understanding of the jet injection in LPP compressors is to extend these studies to elevated temperatures and pressures. These results along with the current results will then complete the behavior description of liquid jets which can then be used in the design of next-generation low emission combustors.

Another extension of the current study is to study the injection of liquid jets into a swirling crossflow. A significant amount of swirl is imparted to the flow inside the combustion chamber in order to stabilize the flame. If the behavior of a jet is a swirling flow is known, it will allow us to gain a better understanding of the phenomena inside the combustion chamber, though it is much more complicated. Further, it might also allow us to inject fuel directly into the swirling air passed into the combustion chamber, thus avoiding the need for premix ducts.

References

1. Aalburg, C., Sallam, K. A. and Faeth, G. M., "Properties of Nonturbulent Round Liquid Jets in Uniform Crossflows", AIAA Paper, 2004-0969, Jan 2004

2. Becker, J. and Hassa, C., "Breakup and Atomization of a Kerosene Jet in Crossflow at Elevated Pressure", *Atomization and Sprays*, Vol. 11, 2002, pp. 49-67

3. Birouk, M., Azzopardi, B. J., Stäbler, T., "Primary Break-up of a Viscous Liquid Jet in a Cross Ariflow", *Particle and Particle Systems Characterization*, Vol. 20, 2003, pp. 283-289

4. Cavaliere, A., Ragucci, R. and Noviello, C., "Bending and Break-up of a Liquid Jet in a High Pressure Airflow", *Experimental Thermal and Fluid Science*, Vol. 27, 2003, pp. 449-454.

5. Chelko, L. J., "Penetration of Liquid Jets into a High-Velocity Air Stream", NACA RM E50F21, 1950

6. Chen, T. H., Smith, C. R. and Schommer, D. G., "Multi-Zone Behavior of Transverse Liquid Jet in High-Speed Flow", AIAA Paper 93-0453, 1993

7. Clark, B. J., "Breakup of a Liquid Jet in a Transverse Flow of Gas", NASA TN D-2424, 1964

8. Cortelezzi, L. and Karagozian, A. R., "On the Formation of the Counter-Rotating Vortex Pair in Transverse Jets", *Journal of Fluid Mechanics*, Vol. 446, 2001, pp. 347-373.

9. Flohre, N., "Experimental Investigation of Spray Atomization Properties of an Aircraft Engine Swirl Cup", MS Thesis, University of Cincinnati, 2003.

10. Fuller, R. P., Wu, P.-K., Kirkendall, K. A. and Nejad, A. S., "Effects of Injection Angle on Atomization of Liquid Jets in Transverse Airflow", *AIAA Journal*, Vol. 38, No. 1, January 2000, pp. 64-72.

11. Han, D., Orozco, V. and Mungal, M. G., "Gross-Entrainment Behavior of Turbulent Jets Injected Obliquely into a Uniform Crossflow", *AIAA Journal*, Vol. 38, No. 9, September 2000, pp. 1643-1649.

12. Hautman, D. J. and Rosfjord, T. J., "Transverse Liquid Injection Studies", AIAA Paper 90-1965, 1990.

13. Haven, B. A. and Kurusaka, M., "Kidney and Anti-Kidney Vortices in Crossflow Jets", *Journal of Fluid Mechanics*, Vol. 352, 1997, pp. 27-64.

14. Hussein, G. A., Jasuja, A. K. and Fletcher, R. S., "Penetration and Break-Up Studies of Discrete Liquid Jets in Cross Flowing Airstreams", ASME Paper 82-GT-25, 1982.

15. Inamura, T., "Trajectory of a Liquid Jet Traversing Subsonic Airstreams", *Journal of Propulsion*, Vol. 16, No. 1, 2000, pp. 155-157.

16. Inamura, T. and Nagai, N., "Spray Characteristics of Liquid Jets Traversing Subsonic Airstreams", *Journal of Propulsion and Power*, Vol. 13, No. 2, March-April 1997, pp. 250-256.

17. Inamura, T., Nagai, N., Hirai, T. and Asano, H, "Disintegration Phenomena of Metalized Slurry Fuel Jets in High Speed Air Stream", *Proceedings of the 5th International Conference on Liquid Atomization and Spray System*, Gaithersburg, MD, USA, July 1991, pp. 839-846.

18. Ingebo, R. D., "Aerodynamic Effect of Combustor Inlet-Air Pressure on Fuel Jet Atomization, AIAA paper, 84-1320, 1984.

19. Ingebo, R. D. and Foster, H. H., "Drop-Size Distribution for Crosscurrent Breakup of Liquid Jets in Airstreams", NACA TN 4087, 1957.

20. Kelso, R. M., Lim, T. T. and Perry, A. E., "An Experimental Study of Round Liquid Jets in Cross-Flow", *Journal of Fluid Mechanics*, Vol. 306, 1996, pp. 111-144.

21. Kihm, K. D., Lyn, G. M. and Son, S. Y., "Atomization of Cross-Injecting Sprays into Convective Air Stream", *Atomization and Sprays*, Vol. 5, 1995, pp. 417-433.

22. Lefebvre, A. H., *Gas Turbine Combustion*, 2nd ed., Taylor & Francis, 1998, pp. 324-363.

23. Less, D. M. and Schetz, J. A., "Transient Behavior of Liquid Jets Injected Normal to a High-Velocity Gas Stream", *AIAA Journal*, Vol. 24, No. 12, December 1986, pp. 1979-1986.

24. Lin, K.-C., Kennedy, P. J. and Jackson, T. A., "A Review of Penetration Heights of Transverse Liquid Jets in High-Speed Flows", *Proceedings of the 15th International Conference on Liquid Atomization and Spray System*, Madison, Wisconsin USA, 2002, pp. 345-349.

25. Liu, F., Smallwood, G. J. and Gülder, Ö. L., "Numerical Study of Breakup Processes of Water Jet Injected into a Cross Air Flow" *Proceedings of the 8th International Conference on Liquid Atomization and Spray System*, Pasadena, CA, USA 2000, pp 67-73.

26. Madabhushi, R. K., "A Model for Numerical Simulation of Breakup of a Liquid Jet in Crossflow", *Atomization and Sprays*, Vol. 13, 2003, pp. 413-424.

27. Mazallon, J., Dai, Z. and Faeth, G. M., "Primary Breakup of Nonturbulent Round Liquid Jets in Gas Crossflows", *Atomization and Sprays*, Vol. 9, 1999, pp. 291-311.

28. Nejad, A. S. and Schetz, J. A., "Effects of Properties and Location in the Plume on Droplet Diameter for Injection in a Supersonic Stream", *AIAA Journal*, Vol. 21, No. 7, July 1983, pp. 956-961.

29. Oda, T., Hiroyasu, H., Arai, M. and Nishida, K., "Characterization of Liquid Jet Atomization across a High-Speed Airstream", *JSME International Journal*, Series B, Vol. 37, No. 4, 1994, pp. 937-944.

30. Peterson, S. D. and Plesniak, M. W., "Evolution of Jets Emanating from Short Holes into Crossflow", *Journal of Fluid Mechanics*, Vol. 503, 2004, pp. 57-91.

31. Schetz, J. A., Kush Jr., E. A. and Joshi, P. B., "Wave Phenomena in Liquid Jet Breakup in a Supersonic Crossflow", *AIAA Journal*, Vol. 18, No. 7, July 1980, pp. 774-778.

32. Schetz, J. A. and Padhye, A., "Penetration and Breakup of Liquids in Subsonic Airstreams", *AIAA Journal*, Vol. 15, No. 10, October 1977, pp. 1385-1390.

33. Smith, S. H. and Mungal, M. G., "Mixing, Structure and Scaling of the Jet in Crossflow", *Journal of Fluid Mechanics*, Vol. 357, 1998, pp. 83-122.

34. Thomas, R. H. and Schetz, J. A., "Distributions Across the Plume of Transverse Liquid and Slurry Jets in Supersonic Airflow", *AIAA Journal*, Vol. 23, No. 12, December 1985, pp. 1892-1901.

35. Vich, G. and Ledoux, M., "Investigation of a Liquid Jet in a Subsonic Cross-Flow", *Proceedings of the 7th International Conference on Liquid Atomization and Spray System*, Seoul, S. Korea, August 1997, pp. 23-30.

36. Wu. P.-K., Kirkendall, K. A., Fuller, R. P. and Nejad, A. S., "Breakup Processes of Liquid Jets in Subsonic Crossflows", *Journal of Propulsion and Power*, Vol. 13, No. 1, January-February 1997, pp. 64-72.

37. Wu. P.-K., Kirkendall, K. A., Fuller, R. P. and Nejad, A. S., "Spray Structures of Liquid Jets Atomized in Subsonic Crossflows", *Journal of Propulsion and Power*, Vol. 14, No. 2, March-April 1998, pp. 173-181.

38. Yates, C. L., "Liquid Injection into Supersonic Airstreams", AIAA Paper, 71-724, 1971.

39. Yuan, L. L. and Street, R. L., “Trajectory and Entrainment of a Round Jet in Crossflow”, *Physics of Fluids*, Vol. 10, No. 9, September 1998, pp. 2323-2335.

40. Zhu, J. Y., Hou, M. Y. and Chin, J. S., “Experimental Study on the Atomization of Plain Orifice Injector under Uniform Cross Air Flow” ASME Paper, 86-GT-43, 1986.

Appendix A: Pulsed Shadowgraphy Test Conditions

This section contains a detailed list of all the test cases used for pulsed shadowgraphy. The test conditions are sorted by injection liquids and injection diameters. The tables include the various parameters related to the test conditions as well as information on the breakup modes for that particular condition.

Table A1. Test cases for Water, D = 0.381 mm

We	q	U_∞ (m/s)	U_l (m/s)	Re_∞	Re_l	Oh	Breakup Mode
50.5	0.9	89.2	3.0	2.36E+03	1.32E+03	5.23E-03	Column
50.5	2.0	89.2	4.3	2.36E+03	1.90E+03	5.23E-03	Column
50.5	3.0	89.2	5.4	2.36E+03	2.36E+03	5.23E-03	Column
50.5	4.0	89.2	6.2	2.36E+03	2.70E+03	5.23E-03	Column
50.5	4.9	89.2	6.9	2.36E+03	3.02E+03	5.23E-03	Column
50.5	5.9	89.2	7.5	2.36E+03	3.30E+03	5.23E-03	Column
50.5	6.8	89.2	8.1	2.36E+03	3.54E+03	5.23E-03	Column
50.5	7.8	89.2	8.7	2.36E+03	3.81E+03	5.23E-03	Column
50.5	8.9	89.2	9.2	2.36E+03	4.06E+03	5.23E-03	Column
50.5	10.0	89.2	9.8	2.36E+03	4.29E+03	5.23E-03	Column
100.0	1.0	125.5	4.3	3.32E+03	1.89E+03	5.23E-03	Column
100.0	2.0	125.5	6.2	3.32E+03	2.72E+03	5.23E-03	Column
100.0	2.9	125.5	7.5	3.32E+03	3.28E+03	5.23E-03	Column
100.0	4.1	125.5	8.8	3.32E+03	3.86E+03	5.23E-03	Column
100.0	4.9	125.5	9.7	3.32E+03	4.25E+03	5.23E-03	Column
100.0	6.1	125.5	10.7	3.32E+03	4.70E+03	5.23E-03	Column
100.0	7.0	125.5	11.5	3.32E+03	5.05E+03	5.23E-03	Column
100.0	8.0	125.5	12.3	3.32E+03	5.41E+03	5.23E-03	Mixed
100.0	9.0	125.5	13.1	3.32E+03	5.73E+03	5.23E-03	Mixed
100.0	10.0	125.5	13.8	3.32E+03	6.03E+03	5.23E-03	Mixed
147.3	1.0	152.3	5.3	4.03E+03	2.32E+03	5.23E-03	Column
147.3	2.0	152.3	7.5	4.03E+03	3.29E+03	5.23E-03	Column
147.3	3.1	152.3	9.3	4.03E+03	4.08E+03	5.23E-03	Column
147.3	4.0	152.3	10.6	4.03E+03	4.66E+03	5.23E-03	Mixed
147.3	5.1	152.3	11.9	4.03E+03	5.23E+03	5.23E-03	Mixed
147.3	6.1	152.3	13.0	4.03E+03	5.71E+03	5.23E-03	Mixed
147.3	7.1	152.3	14.1	4.03E+03	6.19E+03	5.23E-03	Mixed
147.3	8.1	152.3	15.1	4.03E+03	6.61E+03	5.23E-03	Mixed
147.3	9.1	152.3	16.0	4.03E+03	7.00E+03	5.23E-03	Mixed
147.3	10.2	152.3	16.9	4.03E+03	7.40E+03	5.23E-03	Mixed
198.9	1.0	177.0	6.1	4.68E+03	2.69E+03	5.23E-03	Column
198.9	2.0	177.0	8.7	4.68E+03	3.82E+03	5.23E-03	Column
198.9	3.0	177.0	10.7	4.68E+03	4.69E+03	5.23E-03	Mixed
198.9	3.9	177.0	12.2	4.68E+03	5.34E+03	5.23E-03	Mixed
198.9	5.0	177.0	13.7	4.68E+03	6.01E+03	5.23E-03	Mixed
198.9	6.0	177.0	15.0	4.68E+03	6.60E+03	5.23E-03	Mixed
198.9	7.1	177.0	16.4	4.68E+03	7.18E+03	5.23E-03	Mixed
198.9	8.0	177.0	17.4	4.68E+03	7.64E+03	5.23E-03	Surface
198.9	9.0	177.0	18.5	4.68E+03	8.10E+03	5.23E-03	Surface
198.9	10.1	177.0	19.5	4.68E+03	8.54E+03	5.23E-03	Surface
247.6	1.0	197.4	6.8	5.22E+03	2.99E+03	5.23E-03	Column
247.6	2.0	197.4	9.7	5.22E+03	4.25E+03	5.23E-03	Mixed
247.6	3.1	197.4	12.0	5.22E+03	5.26E+03	5.23E-03	Mixed
247.6	4.0	197.4	13.7	5.22E+03	6.02E+03	5.23E-03	Mixed
247.6	5.0	197.4	15.3	5.22E+03	6.73E+03	5.23E-03	Surface
247.6	6.0	197.4	16.8	5.22E+03	7.39E+03	5.23E-03	Surface
247.6	7.1	197.4	18.3	5.22E+03	8.02E+03	5.23E-03	Surface
247.6	8.1	197.4	19.5	5.22E+03	8.54E+03	5.23E-03	Surface
247.6	9.1	197.4	20.7	5.22E+03	9.07E+03	5.23E-03	Surface
247.6	10.1	197.4	21.7	5.22E+03	9.54E+03	5.23E-03	Surface

Table A2. Test cases for Jet-A D = 0.381 mm

We	q	U_∞ (m/s)	U_l (m/s)	Re_∞	Re_l	Oh	Breakup Mode
99.0	0.8	77.9	2.7	2.06E+03	6.30E+02	1.41E-02	Column
99.0	1.6	77.9	3.8	2.06E+03	8.83E+02	1.41E-02	Column
99.0	2.3	77.9	4.6	2.06E+03	1.07E+03	1.41E-02	Column
99.0	3.1	77.9	5.3	2.06E+03	1.24E+03	1.41E-02	Column
99.0	3.9	77.9	6.0	2.06E+03	1.40E+03	1.41E-02	Column
99.0	4.7	77.9	6.5	2.06E+03	1.53E+03	1.41E-02	Mixed
99.0	5.4	77.9	7.0	2.06E+03	1.65E+03	1.41E-02	Mixed
99.0	6.2	77.9	7.5	2.06E+03	1.76E+03	1.41E-02	Mixed
99.0	7.1	77.9	8.0	2.06E+03	1.88E+03	1.41E-02	Mixed
99.0	7.8	77.9	8.4	2.06E+03	1.98E+03	1.41E-02	Mixed
295.0	0.8	134.4	4.6	3.55E+03	1.08E+03	1.41E-02	Column
295.0	1.6	134.4	6.5	3.55E+03	1.53E+03	1.41E-02	Mixed
295.0	2.4	134.4	8.0	3.55E+03	1.88E+03	1.41E-02	Mixed
295.0	3.2	134.4	9.2	3.55E+03	2.17E+03	1.41E-02	Surface
295.0	3.9	134.4	10.3	3.55E+03	2.42E+03	1.41E-02	Surface
295.0	4.7	134.4	11.3	3.55E+03	2.64E+03	1.41E-02	Surface
295.0	5.5	134.4	12.2	3.55E+03	2.87E+03	1.41E-02	Surface
295.0	6.3	134.4	13.1	3.55E+03	3.06E+03	1.41E-02	Surface
295.0	7.1	134.4	13.8	3.55E+03	3.24E+03	1.41E-02	Surface
295.0	7.9	134.4	14.6	3.55E+03	3.43E+03	1.41E-02	Surface
483.4	0.8	172.1	5.9	4.55E+03	1.39E+03	1.41E-02	Surface
483.4	1.6	172.1	8.4	4.55E+03	1.97E+03	1.41E-02	Surface
483.4	2.4	172.1	10.3	4.55E+03	2.42E+03	1.41E-02	Surface
483.4	3.2	172.1	11.9	4.55E+03	2.80E+03	1.41E-02	Surface
483.4	4.0	172.1	13.4	4.55E+03	3.14E+03	1.41E-02	Surface
483.4	4.8	172.1	14.6	4.55E+03	3.42E+03	1.41E-02	Surface
483.4	5.6	172.1	15.7	4.55E+03	3.69E+03	1.41E-02	Surface
483.4	6.4	172.1	16.9	4.55E+03	3.95E+03	1.41E-02	Surface
483.4	7.2	172.1	17.9	4.55E+03	4.20E+03	1.41E-02	Surface
483.4	8.0	172.1	18.9	4.55E+03	4.42E+03	1.41E-02	Surface
670.8	0.8	202.7	7.1	5.36E+03	1.65E+03	1.41E-02	Surface
670.8	1.6	202.7	10.0	5.36E+03	2.34E+03	1.41E-02	Surface
670.8	2.4	202.7	12.2	5.36E+03	2.87E+03	1.41E-02	Surface
670.8	3.2	202.7	14.1	5.36E+03	3.31E+03	1.41E-02	Surface
670.8	4.1	202.7	15.9	5.36E+03	3.72E+03	1.41E-02	Surface
670.8	4.8	202.7	17.3	5.36E+03	4.05E+03	1.41E-02	Surface
670.8	5.6	202.7	18.7	5.36E+03	4.37E+03	1.41E-02	Surface
670.8	6.5	202.7	20.0	5.36E+03	4.68E+03	1.41E-02	Surface
670.8	7.3	202.7	21.2	5.36E+03	4.97E+03	1.41E-02	Surface
670.8	8.1	202.7	22.3	5.36E+03	5.23E+03	1.41E-02	Surface
760.8	0.8	215.9	7.5	5.70E+03	1.77E+03	1.41E-02	Surface
760.8	1.6	215.9	10.7	5.70E+03	2.50E+03	1.41E-02	Surface
760.8	2.5	215.9	13.1	5.70E+03	3.08E+03	1.41E-02	Surface
760.8	3.3	215.9	15.1	5.70E+03	3.54E+03	1.41E-02	Surface
760.8	4.1	215.9	16.9	5.70E+03	3.97E+03	1.41E-02	Surface
760.8	4.9	215.9	18.5	5.70E+03	4.33E+03	1.41E-02	Surface
760.8	5.7	215.9	20.0	5.70E+03	4.70E+03	1.41E-02	Surface
760.8	6.5	215.9	21.4	5.70E+03	5.01E+03	1.41E-02	Surface
760.8	7.3	215.9	22.6	5.70E+03	5.31E+03	1.41E-02	Surface
760.8	8.1	215.9	23.9	5.70E+03	5.60E+03	1.41E-02	Surface

Table A3. Test cases for Jet-A, D = 0.762 mm

We	q	U_∞ (m/s)	U_l (m/s)	Re_∞	Re_l	Oh	Breakup Mode
979.0	1.0	173.1	6.6	9.15E+03	1.69E+07	9.95E-03	Surface
979.1	2.0	173.2	9.4	9.15E+03	1.69E+07	9.95E-03	Surface
980.3	3.0	173.3	11.5	9.16E+03	1.69E+07	9.95E-03	Surface
979.7	4.0	173.2	13.4	9.15E+03	1.69E+07	9.95E-03	Surface
979.4	4.9	173.2	14.9	9.15E+03	1.69E+07	9.95E-03	Surface
981.2	5.9	173.3	16.3	9.16E+03	1.69E+07	9.95E-03	Surface
980.9	6.9	173.3	17.6	9.16E+03	1.69E+07	9.95E-03	Surface
981.5	7.9	173.4	18.9	9.16E+03	1.69E+07	9.95E-03	Surface
978.8	8.8	173.1	19.9	9.15E+03	1.69E+07	9.95E-03	Surface
979.4	9.9	173.2	21.1	9.15E+03	1.69E+07	9.95E-03	Surface
1168.2	1.0	189.1	7.3	1.00E+04	2.01E+07	9.95E-03	Surface
1173.0	2.0	189.5	10.3	1.00E+04	2.02E+07	9.95E-03	Surface
1169.6	3.0	189.2	12.7	1.00E+04	2.02E+07	9.95E-03	Surface
1171.6	4.0	189.4	14.6	1.00E+04	2.02E+07	9.95E-03	Surface
1169.9	4.9	189.3	16.3	1.00E+04	2.02E+07	9.95E-03	Surface
1173.0	5.9	189.5	17.9	1.00E+04	2.02E+07	9.95E-03	Surface
1171.3	6.9	189.4	19.3	1.00E+04	2.02E+07	9.95E-03	Surface
1171.3	7.9	189.4	20.6	1.00E+04	2.02E+07	9.95E-03	Surface
1171.0	8.9	189.4	21.9	1.00E+04	2.02E+07	9.95E-03	Surface
1170.2	9.9	189.3	23.0	1.00E+04	2.02E+07	9.95E-03	Surface
1272.4	1.0	197.4	7.6	1.04E+04	2.19E+07	9.95E-03	Surface
1270.8	2.0	197.3	10.7	1.04E+04	2.19E+07	9.95E-03	Surface
1272.4	2.9	197.4	13.1	1.04E+04	2.19E+07	9.95E-03	Surface
1270.8	4.0	197.3	15.2	1.04E+04	2.19E+07	9.95E-03	Surface
1271.0	4.9	197.3	17.0	1.04E+04	2.19E+07	9.95E-03	Surface
1274.0	5.9	197.5	18.5	1.04E+04	2.20E+07	9.95E-03	Surface
1268.9	6.9	197.1	20.1	1.04E+04	2.19E+07	9.95E-03	Surface
1268.9	7.9	197.1	21.5	1.04E+04	2.19E+07	9.95E-03	Surface
1269.1	8.9	197.1	22.8	1.04E+04	2.19E+07	9.95E-03	Surface
1271.0	9.9	197.3	24.0	1.04E+04	2.19E+07	9.95E-03	Surface

Table A4. Test cases for N-Heptane, D = 0.381 mm

We	q	U_∞ (m/s)	U_l (m/s)	Re_∞	Re_l	Oh	Breakup Mode
301.6	0.7	118.8	4.1	3.14E+03	1.79E+03	8.04E-03	Column
301.6	1.4	118.8	5.8	3.14E+03	2.52E+03	8.04E-03	Mixed
301.6	2.0	118.8	7.1	3.14E+03	3.09E+03	8.04E-03	Mixed
301.6	2.7	118.8	8.1	3.14E+03	3.53E+03	8.04E-03	Surface
301.6	3.4	118.8	9.2	3.14E+03	3.99E+03	8.04E-03	Surface
301.6	4.1	118.8	10.1	3.14E+03	4.38E+03	8.04E-03	Surface
301.6	4.7	118.8	10.8	3.14E+03	4.71E+03	8.04E-03	Surface
301.6	5.5	118.8	11.7	3.14E+03	5.07E+03	8.04E-03	Surface
301.6	6.1	118.8	12.3	3.14E+03	5.33E+03	8.04E-03	Surface
301.6	6.8	118.8	13.0	3.14E+03	5.65E+03	8.04E-03	Surface
498.8	0.7	152.8	5.3	4.04E+03	2.29E+03	8.04E-03	Surface
498.8	1.4	152.8	7.5	4.04E+03	3.27E+03	8.04E-03	Surface
498.8	2.1	152.8	9.2	4.04E+03	3.99E+03	8.04E-03	Surface
498.8	2.8	152.8	10.6	4.04E+03	4.61E+03	8.04E-03	Surface
498.8	3.2	152.8	11.4	4.04E+03	4.97E+03	8.04E-03	Surface
498.8	4.2	152.8	13.0	4.04E+03	5.66E+03	8.04E-03	Surface
498.8	4.8	152.8	14.0	4.04E+03	6.10E+03	8.04E-03	Surface
498.8	5.5	152.8	15.1	4.04E+03	6.54E+03	8.04E-03	Surface
498.8	6.2	152.8	15.9	4.04E+03	6.90E+03	8.04E-03	Surface
498.8	6.8	152.8	16.7	4.04E+03	7.27E+03	8.04E-03	Surface
694.8	0.7	180.3	6.3	4.77E+03	2.73E+03	8.04E-03	Surface
694.8	1.4	180.3	8.9	4.77E+03	3.85E+03	8.04E-03	Surface
694.8	2.1	180.3	10.9	4.77E+03	4.75E+03	8.04E-03	Surface
694.8	2.8	180.3	12.6	4.77E+03	5.45E+03	8.04E-03	Surface
694.8	3.4	180.3	14.0	4.77E+03	6.08E+03	8.04E-03	Surface
694.8	4.1	180.3	15.3	4.77E+03	6.66E+03	8.04E-03	Surface
694.8	4.8	180.3	16.6	4.77E+03	7.22E+03	8.04E-03	Surface
694.8	5.5	180.3	17.7	4.77E+03	7.70E+03	8.04E-03	Surface
694.8	6.3	180.3	18.9	4.77E+03	8.21E+03	8.04E-03	Surface
694.8	6.9	180.3	19.9	4.77E+03	8.64E+03	8.04E-03	Surface
888.5	0.7	203.9	7.2	5.39E+03	3.11E+03	8.04E-03	Surface
888.5	1.4	203.9	10.1	5.39E+03	4.37E+03	8.04E-03	Surface
888.5	2.1	203.9	12.3	5.39E+03	5.36E+03	8.04E-03	Surface
888.5	2.8	203.9	14.2	5.39E+03	6.18E+03	8.04E-03	Surface
888.5	3.5	203.9	15.9	5.39E+03	6.91E+03	8.04E-03	Surface
888.5	4.2	203.9	17.5	5.39E+03	7.58E+03	8.04E-03	Surface
888.5	4.9	203.9	18.9	5.39E+03	8.22E+03	8.04E-03	Surface
888.5	5.6	203.9	20.1	5.39E+03	8.74E+03	8.04E-03	Surface
888.5	6.3	203.9	21.4	5.39E+03	9.30E+03	8.04E-03	Surface
888.5	7.0	203.9	22.6	5.39E+03	9.79E+03	8.04E-03	Surface
985.3	0.7	214.8	7.5	5.68E+03	3.25E+03	8.04E-03	Surface
985.3	1.4	214.8	10.6	5.68E+03	4.62E+03	8.04E-03	Surface
985.3	2.1	214.8	13.0	5.68E+03	5.64E+03	8.04E-03	Surface
985.3	2.8	214.8	15.0	5.68E+03	6.52E+03	8.04E-03	Surface
985.3	3.5	214.8	16.8	5.68E+03	7.30E+03	8.04E-03	Surface
985.3	4.2	214.8	18.4	5.68E+03	7.98E+03	8.04E-03	Surface
985.3	4.9	214.8	19.8	5.68E+03	8.61E+03	8.04E-03	Surface
985.3	5.6	214.8	21.3	5.68E+03	9.26E+03	8.04E-03	Surface
985.3	6.3	214.8	22.6	5.68E+03	9.81E+03	8.04E-03	Surface
985.3	7.0	214.8	23.8	5.68E+03	1.03E+04	8.04E-03	Surface

Table A5. Test cases for N-Heptane, D = 0.762 mm

We	q	U_∞ (m/s)	U_l (m/s)	Re_∞	Re_l	Oh	Breakup Mode
1316.1	1.0	175.5	7.3	9.28E+03	3.21E+07	5.68E-03	Surface
1314.9	2.0	175.4	10.4	9.27E+03	3.21E+07	5.68E-03	Surface
1315.3	3.0	175.4	12.7	9.27E+03	3.21E+07	5.68E-03	Surface
1313.3	4.0	175.3	14.6	9.27E+03	3.20E+07	5.68E-03	Surface
1314.5	4.9	175.4	16.3	9.27E+03	3.21E+07	5.68E-03	Surface
1314.9	6.0	175.4	17.9	9.27E+03	3.21E+07	5.68E-03	Surface
1314.1	6.9	175.4	19.3	9.27E+03	3.20E+07	5.68E-03	Surface
1316.5	7.9	175.5	20.7	9.28E+03	3.21E+07	5.68E-03	Surface
1316.5	8.9	175.5	21.9	9.28E+03	3.21E+07	5.68E-03	Surface
1316.1	9.8	175.5	23.1	9.28E+03	3.21E+07	5.68E-03	Surface
1514.0	1.0	188.2	7.8	9.95E+03	3.69E+07	5.68E-03	Surface
1519.0	1.9	188.5	10.9	9.97E+03	3.70E+07	5.68E-03	Surface
1521.0	3.0	188.7	13.6	9.97E+03	3.71E+07	5.68E-03	Surface
1521.4	3.9	188.7	15.7	9.97E+03	3.71E+07	5.68E-03	Surface
1520.0	4.9	188.6	17.5	9.97E+03	3.71E+07	5.68E-03	Surface
1523.1	5.9	188.8	19.2	9.98E+03	3.71E+07	5.68E-03	Surface
1527.5	6.9	189.1	20.8	9.99E+03	3.72E+07	5.68E-03	Surface
1527.4	7.8	189.1	22.2	9.99E+03	3.72E+07	5.68E-03	Surface
1531.7	8.9	189.3	23.6	1.00E+04	3.74E+07	5.68E-03	Surface
1540.7	9.7	189.9	24.8	1.00E+04	3.76E+07	5.68E-03	Surface
1724.8	1.0	200.9	8.4	1.06E+04	4.21E+07	5.68E-03	Surface
1719.9	2.0	200.6	11.9	1.06E+04	4.19E+07	5.68E-03	Surface
1721.2	3.0	200.7	14.5	1.06E+04	4.20E+07	5.68E-03	Surface
1720.3	3.9	200.6	16.7	1.06E+04	4.19E+07	5.68E-03	Surface
1723.7	4.9	200.9	18.6	1.06E+04	4.20E+07	5.68E-03	Surface
1722.2	5.9	200.8	20.4	1.06E+04	4.20E+07	5.68E-03	Surface
1724.1	6.9	200.9	22.1	1.06E+04	4.20E+07	5.68E-03	Surface
1720.6	7.9	200.7	23.6	1.06E+04	4.20E+07	5.68E-03	Surface
1722.3	8.8	200.8	25.0	1.06E+04	4.20E+07	5.68E-03	Surface
1725.1	9.8	200.9	26.4	1.06E+04	4.21E+07	5.68E-03	Surface